Several Surface Plasmon Related Phenomena in Metallic Periodic Nano-Structures

Von der Fakultät für Elektrotechnik, Informationstechnik, Physik
der Technischen Universität Carolo-Wilhelmina zu Braunschweig

zur Erlangung des Grades eines Doktors

der Naturwissenschaften (Dr. rer. nat.)

genehmigte Dissertation

von Bo Liu

aus Liaoning, China

eingereicht am: 07.11.2018

Disputation am: 16.01.2019

1. Referent: Prof. Dr. Peter Lemmens
2. Referent: Prof. Dr. Meinhard Schilling

Druckjahr: 2019

Dissertation an der Technischen Universität Braunschweig,
Fakultät für Elektrotechnik, Informationstechnik, Physik

VORVERÖFFENTLICHUNGEN DER DISSERTATION

Teilergebnisse aus dieser Arbeit wurden mit Genehmigung der Fakultät für Elektrotechnik, Informationstechnik, Physik, vertreten durch den Betreuer der Arbeit, in folgenden Beiträgen vorab veröffentlicht:

Publikationen

- B. Hampel, B. Liu, F. Nording, J. Ostermann, P. Struszewski, J. Langfahl-Klabes, M. Bieler, H. Bosse, P. Lemmens, M. Schilling, and R. Tutsch *Approach to determine measurement uncertainty in complex nanosystems with multiparametric dependencies and multivariate output quantities*, Meas. Sci. Technol. **29**, 035003 (2018)

- J. Patwari, S. Sardar, B. Liu, P. Lemmens and S. Pal *Three-in-one approach towards efficient organic dye-sensitized solar cells: aggregation suppression, panchromatic absorption and resonance energy transfer*, Beilstein J. Nanotechnol. **8**, 17051713 (2017)

- B. Liu, H. Yan, R. Stosch, B. Wolfram, M. Brring, A. Bakin, M. Schilling and P. Lemmens, *Modelling plexcitons of periodic gold nanorod arrays with molecular components* , Nanotechnology **28**, 195201 (2017)

- M. Khatun, S. Choudhury, B. Liu, P. Lemmens, S. K. Pal, and S. Mazumder, *Resveratrol-ZnO Nanohybrid Enhanced Anti-cancerous Effect in Ovarian Cancer Cells through ROS*, RSC Adv. **6**, 105607 (2016)

- P. Kar, S. Sardar, B. Liu, M. Sreemany, P. Lemmens, S. Ghosh, and S. K. Pal, *Facile Synthesis of Reduced Graphene Oxide-gold Nanohybrid for Potential Use in Industrial Waste-water Treatment* Sci. and Techn. Adv. Mat. **17**, 375 (2016)

- S. Sardar, H. Remita, P. Kar, B. Liu, P. Lemmens, S. K. Pal, and S. Ghosh, *Enhanced Photovoltage in DSSC: Synergistic Combination of Silver Modified TiO_2 Photoanode and low cost Counter Electrode*, RSC Adv. **6**, 33433 (2016)

- S. Sardar, P. Kar, H. Remita, B. Liu, P. Lemmens, S. K. Pal, and S. Ghosh, *Enhanced Charge Separation and Resonance Energy Transfer at Heterojunctions between Semiconductor Nanoparticles and Conducting Polymer Nanofibers for Efficient Solar Light Harvesting*, Sci. Rep. **5**, 17313 (2015)

- P. Kar, S. Sardar, S. Ghosh, M. R. Parida, B. Liu, O. F. Mohammed, P. Lemmens, and S. K. Pal, *Nano Surface Engineering of Mn_2O_3 for Potential Light-Harvesting Applications* J. Mater. Chem. C **3**, 8200 (2015)

Tagungsbeiträge

- *Approach to quantify chemical enhancement contribution in surface enhanced Raman scattering* (Presentation), DPG Spring Meeting, Berlin, (2018)

- *Quantitative concentration measurements of organic molecules based on on-chip isotope-dilution surface enhanced Raman spectrometry* (Poster), International conference on SERS, Xiamen, China, (2017)

- *Magnetic Nano wires in 2D array* (Presentation), Iron Symposium in Hannover, (2016)

- *ZnO coated TiO_2 photoanodes with improved electron transfer for dye sensitized solar cells* (Presentation), DPG Spring Meeting, Berlin, (2015)

CONTENTS

ABBREVIATIONS

AAO	anodic aluminium oxide
AR	aspect ratio
CLT	central limit theorem
CM	chemical mechanism
DFT	density functional theory
EELS	electron energy loss spectroscopy
EF	enhancement factor
EM	electromagnetic mechanism
FEM	finite element method
FE-SEM	field emission scanning electron microscope
HA	hard anodization
HOMO	highest occupied molecular orbital
IEIS	isotope edited internal standard
IDSERS	isotope dilution surface-enhanced Raman scattering
IR	infrared
ITO	indium tin oxide
L-mode	longitudinal mode
LSP	localized surface plasmon
LSPR	localized surface plasmon resonance
LUMO	lowest unoccupied molecular orbital
MA	mild anodization
NIR	near-infrared
NMR	nuclear magnetic resonance
PDF	probability distributions function
PMDA	pyromellitic dianhydride
PS	polystyrene sphere
PSSE	plasmonic spectral shaping effect
R6G	rhodamine 6G
RS	Raman scattering
SEM	scanning electron microscope

SERS	surface enhanced Raman scattering
SERRS	surface enhanced resonant Raman scattering
SPP	surface plasmon polariton
TDDFT	time dependent density functional theory
T-mode	transverse mode
UV	ultraviolet
Vis	visible (light)

ÜBERBLICK

In dieser Arbeit werden kostengünstige Self-Assembly Verfahren zur Herstellung periodischer Nanostrukturen beschrieben und verschiedene Licht-Nanopartikel-Molekül-Wechselwirkungsphänomene, die mit solchen Strukturen in Zusammenhang stehen, diskutiert. Diese sind Wechselwirkungen zwischen Oberflächenplasmonen und molekularen Exzitonen in Array-Systemen sowie quantitative Messungen der oberflächenverstärkten Raman-Streuung. Eine starke Wechselwirkung zwischen Oberflächenplasmonen und molekularen Exzitonen wird experimentell demonstriert in einem Array- System und ihre hybriden Zustände werden unter Verwendung eines Quantenmodells durch Quantisieren des kollektiven plasmonischen Verhaltens in einem Array als ein einzelnes Quasiteilchen theoretisch beschrieben. Diese Näherung bietet die Möglichkeit, die komplizierte Berechnung von Fernwechselwirkungen zwischen den einzelnen Nanopartikeln des plexcitonischen periodischen Systems zu vermeiden. Im Zusammenhang mit der oberflächen-verstärkten Raman-Streuung führt der Autor eine Methode ein, die auf lichtinduzierten molekularen Degradationen beruht, um den Verstärkungs-beitrag von chemischen Mechanismen zu identifizieren, und erstellt ein Verarmungsmodell, um den Beitrag der chemischen Mechanismen zu quantifizieren. Darüber hinaus prognostiziert der Autor für eine Konzentrationsmessmethode, genannt On-Chip Interner Standard Oberflächenverstärkter Raman Spektroskopie, einen möglichweise herausfordernden Konzentrationsbereich ($10^{-11} \sim 10^{-7}$ M) von Analyten.

Diese Arbeit könnte das Verständnis von Oberflächenplasmon-Molekül-Wechselwirkungsphänomenen in metallischen Nanostrukturen verbessern und das Design von auf Oberflächenplasmon-Molekülinteraktion beruhenden Sensoren, Vorrichtungen und Techniken unterstützen.

ABSTRACT

In this thesis cost-efficient self-assembly approaches are described to achieve periodic nanostructures and several light-nanoparticle-molecule interaction phenomena related to such structures are discussed. In detail, these are interactions between surface plasmons and molecular excitons in array systems and quantitative surface enhanced Raman scattering measurements. The author experimentally demonstrates a strong coupling between surface plasmons and molecular excitons in an arrayed system, and he theoretically describes their hybrid states using a quantum model by quantizing the collective plasmonic behavior of an array as a single quasi-particle. This approximation offers an opportunity to avoid the complicated calculation of long-distance interactions between the individual nanoparticles of the plexcitonic periodic system. With respect to surface enhanced Raman scattering, the author introduces an approach based on light induced molecular degradations to identify the enhancement contribution from chemical mechanisms, and builds a depletion model to achieve a quantification of the chemical mechanisms contribution. Moreover, for a concentration measurement technique combined by internal standard method and surface enhanced Raman spectroscopy, the author predicts a possible challenging concentration range ($10^{-11} \sim 10^{-7}$ M) of analytes in an on-chip internal standard surface enhanced Raman spectroscopy.

This work could improve the understanding of surface plasmon-molecule interaction phenomena in metallic nano structures and improve the design of surface plasmon-molecule interaction based sensors, devices and techniques.

1. INTRODUCTION

Nanomaterials refer to materials, which consist of basic structural elements having a size of 1 to 100 nm at least in one dimension. [1] They perform usually exotic properties compared to conventional materials. [2, 3]

Generally speaking, their differences come from the mesoscopic physics on this scale. In macroscopic matter the length scale is much larger than the coherent scale of the microscopic particles inside. Therefore, system properties obey usually the laws of classical mechanics, and can be derived from averaged properties of a large number of constituent particles. By contrast, in a system on the nano scale, the coherent scale of the constituent particles are usually comparable with the system site. Therefore the coherence strongly effects system properties. Usually they can not be well described as averaged properties of the constituent particles, and any slight difference could lead to remarkable system property fluctuations, so called *mesoscopic fluctuations*.

In order to easily understand the unusual behaviors of nanomaterials, the effects at this scale are usually categorized and attributed to the following four categories: surface effects, small size effect, quantum confinement effects and macroscopic quantum tunneling. [4]

Due to their exotic properties, nanomaterials are of broad interest in applications: Since the last four decades substantial research has been performed in this field. In 2016 about 140.000 nanotechnology articles have been indexed in Web of Science (WoS) Database, which is 9.5% of all articles indexed in this database in the same year. At the same time, the outcomes of those research projects have already started to contribute to both industry and our daily life, such as titanium dioxide and zinc oxide nanoparticles in sunscreen and some food products; silver nanoparticles in food packaging, clothing, disinfectants and household appliances; and cerium oxide in the glass industry and as a catalyst in a fuel cell. [5, 6]

1.1 Periodic Nanostructures

The idea of using spatially-structured nano systems to control the propagation of light and light-matter interaction was proposed in 1987. [7, 8] It

opened up a new possibility for designing the electromagnetic response of materials.

The investigation of such periodic nanosystems begun with *photonic crystals*, which provide application in the area of active photonic crystals fibres, functional optical components as well as sensors. Some of them have even entered into industrial applications. During this period, some groups expanded the initial focus from dielectric to non-dielectric, dispersive materials such as metals and discussed the properties of periodic metallic structures, so called *plasmonic crystals*. After the pioneering work of John Pendry at the beginning of this century, resonances were also investigated in dispersive structures with periodic permeability and permittivity, named *metamaterials*. This was important to understand the difference in the negative refraction in metamaterials and dielectric photonic crystals. [9]

Since that, comprehensive research has been attracted to this field, due to its substantial potential for applications. [10, 11] Moreover, from the fundamental point of view, a spatial periodic stricture is of also substantial interest in condensed matter physics: how would a mesoscopic symmetry or breaking of symmetry affect the properties of a system? [12, 13]

1.1.1 Photonic Crystals

A photonic crystal is a periodic optical nanostructure that affects the motion of photons in the similar way that crystal lattice affects electrons in solids. [14]

It can be explained by the theory of quantum mechanics in a periodic potential that the lattice can prohibit the propagation of certain waves. In electronic materials, band gaps of electrons in the energy/momentum space are well known. The optical analogue is the photonic crystal, in which periodically modulated dielectric structures exhibit their multibranch dispersion separated by photonic band gaps (PBGs). This gives rise to a large number of exotic physical properties and significant interest in potential applications in all-optical information processing and transformation. One famous application would be the photonic crystal fiber, in which bend loss is ultimately limited comparing to the conventional optical fiber. [15, 16]

Here we present a visual comparison between disordered polystyrene spheres and periodic arrangement of polystyrene nanospheres in the Fig. 1.1. More details about this will be covered in section 4.2.2.1.

1.1.2 Surface Plasmonic Crystals

The term surface plasmon is used both for propagating waves of electronic polarization along a plane interface with an exponential decay away from the

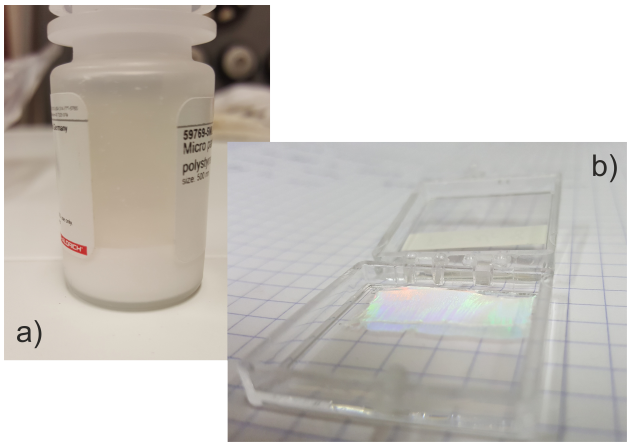

Fig. 1.1: a) Randomly arranged polystyrene nanospheres with a diameter of 500 nm. b) Periodically arranged polystyrene nanospheres. The structure makes difference.

interface as well as for localized electron oscillations in metallic nanostructures. [17]

The existence of surface plasmon was first predicted in 1957 by Rufus Ritchie, while the observation and application were much earlier in fact. [17, 18] In the last decades, surface plasmons were extensively studied in many fields due to their potential for applications, for instance, designing waveguides and sub-wavelength devices in optics, medical application in photothermal therapy, and plasmonic spectroscopies, etc. [19, 20, 21, 22]

In this thesis, several surface plasmon related phenomena will be discussed as main topics.

1.1.3 Metamaterials

Metamaterials are artificially produced materials with optical, electrical or magnetic properties which are not found in nature. They are assemblies of multiple units from different materials commonly with a periodicity. In fact, there are overlaps among the definitions of photonic crystals, surface plasmon and metamaterials, and interdiscipline studies such as plasmonic metamaterials are also widely carried out. [23, 24]

An exciting example of application of metamaterials are so-called *metamaterial cloaking* or *invisibility cloaking*. It makes objects transparent, in visible light, infrared or microwave range, usually. [25, 26] For this purpose, researchers design the periodicity of refractive index in the camouflage material in such a way that it is more favorable for the light to circulate the camouflaged object instead of being deflected or reflexed.

In order to influence the radiation, the structures of the metamaterial have to be smaller than the wavelength of the electromagnetic wave. And the wavelengths of visible light are in the range of a few hundred nanometers, which makes the production of suitable structures relative difficult.

1.2 Fabrication of periodic Nanostructures

Large-area periodic nanoscale structures, which consist of building units with feature sizes on the nanoscale level, can generally be fabricated by the top-down and bottom-up approaches. The top-down approach consists of different techniques, for instance *electron beam lithography*, *ion beam lithography*, *direct laser writing lithography* and *nanoimprint*, to cut or shape materials into the expected shape and order. [23, 27, 28] While the bottom-up approach usually seeks to arrange small components into complex assemblies. [29, 30] Some fabrication processes, such as *copolymer lithography* and *nanosphere lithography*, also combine both top-down and bottom-up techniques. [31, 32, 33, 34]

One example of cost-efficient fabrication of large-area periodic nanostructures by top-down methods is nanoimprint lithography. [27, 35] A photoresist layer is first coated onto a substrate. Then the working stamp, which can be fabricated by variant techniques, is pressed into the photoresist layer and a negative copy of the structures of stamp remains on the resist layer. After etching through the residual resist layer, a large-area periodic nanostructure is achieved. [35]

Another example of fabrication of periodic nanostructures with low cost is the self-assembly template route. A self-assembly template, which has a nanostructure is prepared first, and the target material is deposited into the template to obtain a negative copy (or a part of negative copy) of the template structure. [36, 29] Expensive lithography equipments are not necessary in this method, therefore, the expense can be further reduced.

In this thesis, we fabricate all periodic nanostructures based on the self-assembly template route. More details will be shown in following chapters.

2. BASIC THEORY

This chapter lists some of the basic concepts and theories, which are used in the experiment section and later discussions.

The basic properties of the surface plasmon excited by the external light field are discussed here.

In addition, a fundamental introduction to systems of molecular energy levels and light absorption is given. Also special emission processes, Raman scattering, fluorescence and coupling between the molecular exciton and plasmon are discussed. For a more detailed discussion we refer to Chapter 4, 5 and 6.

A simulation can offer a realistic description of complex physic models. Two simulation approaches used in this work are highlighted in this chapter.

2.1 Surface Plasmon

The term *surface plasmon* is used for collective delocalized electron oscillations, which are typically confined in a metallic interface or a volume on the nano scale. Generally it can be categorized with two types: *surface plasmon polaritons*, which are propagating waves of electronic polarization along a plane interface with an exponential decay away from the interface; as well as *localized surface plasmons*, when electron oscillations are confined in metallic nanostructures. [37] In this thesis it will mainly cover the latter case.

2.1.1 Surface Plasmon Polariton

Surface plasmon polaritons (SPPs) are electromagnetic excitations propagating along a continuous interface between a dielectric and a conductor. By this definition, these excitations are strictly confined in the perpendicular direction with respect to the interface. Therefore, the three-dimensional problem of SPPs can be reduced to a quasi-two-dimensional problem. These polaritons are generated by the coupling between the exciting electromagnetic fields and oscillations of electron plasma in the conductor. Based on SPP, the field-confinements below the diffraction limit of half wavelength in the dielectric can be achieved. [38, 39]

For the sake of simplicity the most simple model for SPPs, a one-dimensional flat interface between an ideal dielectric and a metal [37] will be introduced. We assume a harmonic time dependent electric field of the following form: $\mathbf{E}(\mathbf{r},t) = \mathbf{E}(\mathbf{r})e^{-i\omega t}$. Starting from Maxwell equations and using vector calculus identities, a Helmholtz equation is derived. This equation describes the electromagnetic wave which propagates:

$$\nabla^2\mathbf{E} + k_0^2\varepsilon\mathbf{E} = 0, \tag{2.1}$$

where $k_0 = \frac{\omega}{c}$ is the wave vector in vacuum.

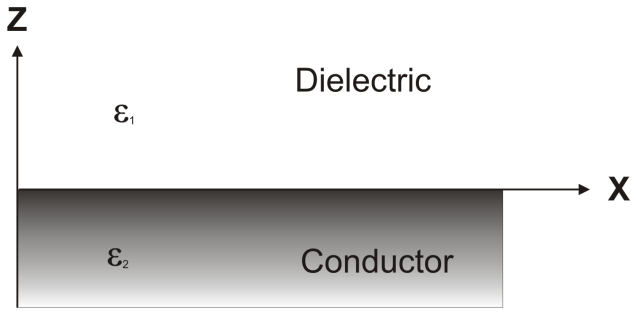

Fig. 2.1: Sketch of one-dimensional model for surface plasmon polariton (SPP).

A one-dimensional model is illustrated in Fig.2.1. It is a one-dimensional problem for dielectric functions because the dielectric function ε only depends on z: $\varepsilon = \varepsilon(z)$.

Now we use

$$\mathbf{E}(\mathbf{r}) = \mathbf{E}(z)e^{i\beta x} \tag{2.2}$$

to describe the propagating waves at the interface. The complex parameter β is named propagation constant and it corresponds to the component of the wave vector in the direction of propagation $\beta = k_x$.

Eq. (2.2) we insert into Eq. (2.1), this yields

$$\frac{\partial^2\mathbf{E}(z)}{\partial z^2} + (k_0^2\varepsilon - \beta^2)\mathbf{E} = 0 \tag{2.3}$$

with

$$\beta = k_0\sqrt{\frac{\varepsilon_1\varepsilon_2}{\varepsilon_1 + \varepsilon_2}}. \tag{2.4}$$

The last term β is the propagation constant of the TM mode. It is an important parameter for applications of SPPs. From the propagation constant β many values can be calculated: The wavelength of the plasmon λ_{spp}, the propagation length L, the energy confinement in the dielectric δ_d and in metal δ_m. These values are fundamental for the sub-wavelength device design. The mathematical details and the introduction can be found in the literature [37].

2.1.2 Localized Surface Plasmon

Localized surface plasmons (LSPs) are oscillations of the surface charge density in metallic nanoparticles. It results from the collective oscillation of the conduction electrons under the constraints imposed by the physical boundaries of the nanoparticle geometry. [17] Both SPPs and LSPs are excitations of the conduction electrons in metallic nanostructure coupled to the exciting electromagnetic field. The most apparent difference between SPPs and LSPs is that the latter one is a non-propagating excitation.

The excitation of LSPs by an electric field with a given incident wavelength occurs typically between the visible (Vis) and the infrared (IR) spectral range for Au and Ag particles. It leads to a resonant absorption maximum and very strong scattering. [40]

We start with the most convenient symmetry which is given by a homogeneous sphere placed at the origin, shown in Fig. 2.2. Note that, a surrounding medium has a real dielectric function ε_m and in the metallic sphere the function ε is complex. For the electric field we consider the approximation $\mathbf{E} = E_0\mathbf{e}_z$. This approximation is only valid if the sphere radius is very small compared to the wavelength.

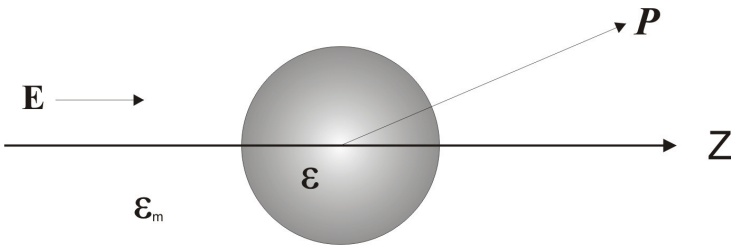

Fig. 2.2: Simple case of a localized surface plasmon.

In the following a basic theoretical introduction to LSPs is given. [41] For the potential Φ the Laplace equation holds: $\nabla^2\Phi = 0$. For this equation the general solution is given by:

$$\Phi(r,\theta) = \sum_{l=0}^{\infty}[A_l r^l + B_l r^{-(l+1)}]P_l(\cos\theta), \tag{2.5}$$

where $P_l(\cos\theta)$ are the Legendre polynomials of order l, and θ is the angle between the position vector $\mathbf{r}$ at a space point P and the unit vector $\mathbf{e}_z$. Using additional boundary conditions, the inner and outer potentials evaluate to [37]

$$\Phi_{in} = -\frac{3\varepsilon_m}{\varepsilon + 2\varepsilon_m}E_0 r\cos\theta \tag{2.6a}$$

$$\Phi_{out} = -E_0 r\cos\theta + \frac{\varepsilon-\varepsilon_m}{\varepsilon+2\varepsilon_m}E_0 a^3\frac{\cos\theta}{r^2}, \tag{2.6b}$$

where a is the radius of the metal sphere.

By comparing to the dipole moment $\mathbf{p}$

$$\mathbf{p} = 4\pi\varepsilon_0\varepsilon_m a^3\frac{\varepsilon-\varepsilon_m}{\varepsilon+2\varepsilon_m}\mathbf{E}_0, \tag{2.7}$$

we get a central result in this section: the polarizability α is given by

$$\alpha = 4\pi a^3\frac{\varepsilon-\varepsilon_m}{\varepsilon+2\varepsilon_m}. \tag{2.8}$$

In the last equation we see that resonant enhancement will occur when $|\varepsilon + 2\varepsilon_m|$ is minimum.

From the last result we can calculate the scattering cross section C_{sca} and the absorption cross section C_{abs}: [37]

$$C_{sca} = \frac{k^4}{6\pi}|\alpha|^2 = \frac{8\pi}{3}k^4a^6\left|\frac{\varepsilon-\varepsilon_m}{\varepsilon+2\varepsilon_m}\right|^2, \tag{2.9a}$$

$$C_{abs} = k\mathrm{Im}[\alpha] = 4\pi k a^3\mathrm{Im}\left[\frac{\varepsilon-\varepsilon_m}{\varepsilon+2\varepsilon_m}\right]. \tag{2.9b}$$

Skipping some mathematical treatments, which are presented in literature [42], a similar consequence for particles with a ellipsoidal form is presented here. The result is useful for our further discussions and for the experimental section. The polarizabilities α_1, α_2 and α_3 along the three principal axes are given by

$$\alpha_i = 4\pi a_1a_2a_3\frac{\varepsilon-\varepsilon_m}{3\varepsilon_m + 3L_i(\varepsilon-\varepsilon_m)}. \tag{2.10}$$

Where the geometrical factor L_i is given by

$$L_i = \frac{a_1a_2a_3}{2}\int_0^\infty \frac{dq}{(a_i^2+q)\sqrt{(q+a_1^2)(q+a_2^2)(q+a_3^2)}}. \tag{2.11}$$

Moreover, practically, the dielectric function ε of a material is a function of the wavelength. So if we choose the material very carefully, special optical properties of metallic nanostructures can be designed for different wavelength ranges. Besides, for the design of the nanostructure, size and shape should also be considered.

The approximation as mentioned above is the so-called quasi-static approximation. In such an approximation, we treat the nanoparticle as an electric dipole, that in principle leads to its validity only for vanishingly small particles. Although we could indicate the resonance frequency via this model, in practice *Mie theory* is also commonly applied to calculate the absorption and scattering response of a nanoparticle, especially when the nanoparticle is relative large. The Mie theory is named after Gustav Mie. It was first developed in 1908 with the initial propose of understanding the colors of colloidal gold particles in solution. In Mie theory internal and scattered fields are expressed as an infinite series of vector spherical harmonics. The detail of Mie theory and the calculation procedure can be found in different books [42, 43] and will not be presented here.

2.2 Absorption and Raman Spectroscopy

In light-matter interaction processes a lot of information about the material structure can be contained, but intermixed with each other. From that we can easily get most of the information just by one single experiment. However, at the same time it is very difficult to separate the informations from each other. In this section some basic concepts of the energy state structure and several typical light-matter interaction processes will be introduced.

2.2.1 Molecular Energy Levels

The energy level scheme in a molecule can be more complex than in a single atom, and usually we separate the molecular energy ϵ into different contributions:

$$\epsilon = \epsilon_{elec} + \epsilon_{vib} + \epsilon_{rot} + \epsilon_{nucl} + \epsilon_{trans}. \tag{2.12}$$

In this equation, ϵ_{elec} is the electronic energy, i.e. the energy of the electrons in orbitals; ϵ_{vib} is the vibrational energy; ϵ_{rot} is the rotational energy associated with rotations of the whole molecule as a unit; and ϵ_{nucl} is from the nuclear motion (e.g., rotation, vibration); ϵ_{trans} is the translational kinetic energy for the whole molecule.

There can be other terms (e.g. terms associated with intermolecular forces, or even with non-bonding intramolecular forces in larger molecules), and some terms do not show up in every situation (e.g. the lack of free rotation in solution). Usually for quantized molecular energy, the last two terms in Eq. (2.12) are ignored. They can be ignored because ϵ_{nucl} is very small and ϵ_{trans} has a continuous contribution.

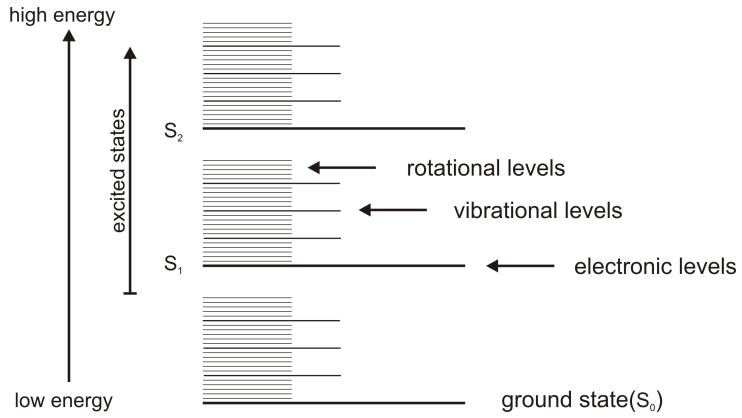

Fig. 2.3: Typical molecular energy levels are shown in the Jablonski diagram [44]. For the energies the following sequence holds: $\epsilon_{elec} > \epsilon_{vib} > \epsilon_{rot}$.

.

The remaining three contributions to the quantized energy are classically not completely independent. For example, a rotation of a molecule introduces an effective centrifugal force, which stretches the bonds and therefore affects the vibrational energy. However, treating these energy terms as separate is a good starting point.

In Fig. 2.3 a diagram of molecular energy levels of singlet states first shown by Alexander Jablonski in the 1930s is given. For further details we refer to literature [44]. It is shown that there are three contributions in order of decreasing energy, ϵ_{elec}, ϵ_{vib}, and ϵ_{rot}, which correspond to different absorption frequencies shown in Tab. 2.1.

Type of energy	Spectral range
Electronic	ultraviolet/visible
Vibrational	infrared
Rotational	microwave

Tab. 2.1: Energy contributions and corresponding absorption ranges.

2.2.2 Absorption

An UV/Vis absorption process can indicate electronic transition from the ground state to an excited state by the absorption of photons in the ultraviolet and visible spectral range. The excited electron will fall back to a lower level to satisfy the Boltzmann distribution. During this process a variety of emissions occur, [45] e.g. shown in Fig. 2.4. These emissions will be introduced in the following sections.

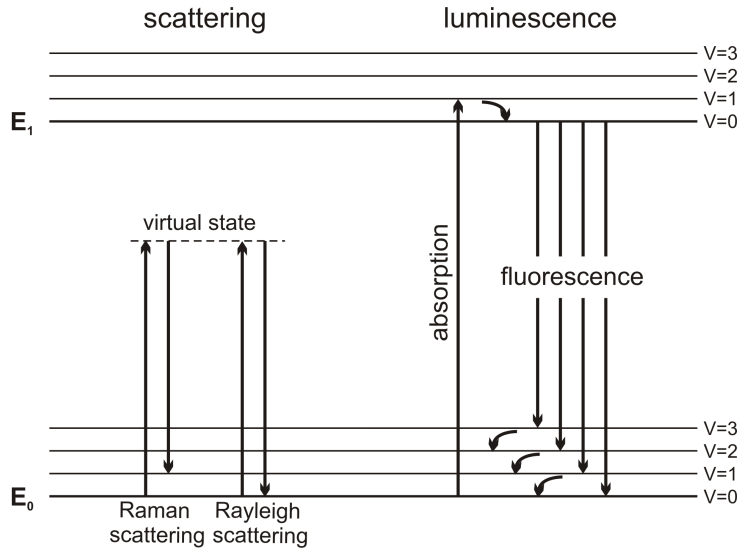

Fig. 2.4: Emission types due to scattering and luminescence processes.

2.2.3 Raman Scattering and Surface Enhanced Raman Scattering

The Raman scattering process consists of a molecular or solid excitation into a virtual intermediate state by an incoming photon and a simultaneous deexcitation of the molecules with a related emission of a photon. This process is very weak and typically only few photons (approximately 1 in 10^9-10^{11}) are emitted, and the wavelengths difference between the exciting and emitted photons is called Stokes shift. On the other side it leads to very sharp Raman spectra with a rich information about the investigated molecules, especially vibration levels. Raman scattering should not be interchanged with the more simple and efficient optical processes. However, if the lifetime of the intermediate state increases and resonance phenomena appear the Raman process is better described by hot fluorescence, see Fig. 2.4.

The strong dependence of Raman scattering on the intensity of the incident electromagnetic field and the nature of the intermediate state allows more complex effects like surface enhanced Raman scattering (SERS) and surface enhanced resonant Raman scattering (SERRS). The SERS process occurs on either metallic surface with a nanoscale roughness or on metallic nanoparticles, and it is practically powerful to enhance the Raman signal of any molecule adsorbed or at the vicinity of a metallic surface. Katrin Kneipp et al. reported the first observation of single molecule Raman scattering by SERS using near-infrared (NIR) excitation of dyes adsorbed on colloidal silver. [46] The scattering crosssection needed to detect single molecules is provided here by the enhanced electromagnetic near fields, which come from

the LSP resonance of the silver nanoparticles. For SERS an enhancement factor of 10^3-10^6 is obtained routinely. [47]

In many publications SERS and SERRS are not discriminated, but in practical applications the two can have very different properties. SERRS arises when the detected molecules have an electronic transition gap close to the energy of the exciting photons used to excite the plasmon in order to create SERS. Thus, both enhancements from the plasmon resonance (SERS) and molecular resonance (R) contribute to very intense scattering. For the first observation of single molecule Raman spectra, a SERRS process was exploited. [46]

When molecules are adsorbed on the metal substrate, the Fermi energy level of metal nanoparticles and the HOMO (highest occupied molecular orbital) and LUMO (lowest unoccupied molecular orbital) energy levels of adsorbed molecules interact with each other and shift. If the energy of incident laser matches with charge transfer transition energy, resonance electron transition occurs between the Fermi level of the substrate and the molecular orbital of the adsorbate. Then the molecular polarization can be changed, which produces the SERS effect. The interaction between molecules and substrate forms a new excited charge transfer state.

Exactly matching the plasmon resonance frequency to the frequency of the electronic transition in the analyte in SERRS is quite difficult and restricting. But in practice it has been found that SERRS works quite well even with a separation between the two maximum resonance frequencies of about 250 nm. [48, 49]

2.3 Simulations

2.3.1 Simulations by the Finite Element Method

We have used the finite element method (FEM) provided by a commercial software package (COMSOL) to calculate the near field distribution of electromagnetic fields in nanoscale metal/oxide composites. In the input file the geometry of the model is described by several parameters, which are obtained in our experimental results. The material properties are described by the refractive indexes which are from the *Handbook of Optical Constants of Solids* edited by Palik. [50]

The basics of the calculations are Maxwell equations and material equations on a net of coordinates. The materials are expressed by their refractive indexes. The output of the software is used to plot absorption diagrams as function of wavelengths as well as the intensity spatial distribution in the nanostructures. An electromagnetic field distribution diagram is shown as

an example in Fig. 2.5. For the sake of simplicity, we consider only the smallest unit in the periodic structure in the simulations, and the symmetry of the structure will be realized by exploiting perfect electric/magnetic conductor boundaries. A sketch of the unit is shown in the upper left corner in Fig. 2.5. Moreover, we will not show the light field intensity in the whole calculation volume in the next chapters. Only the upper 280nm layer of the nanostructure is interesting for us.

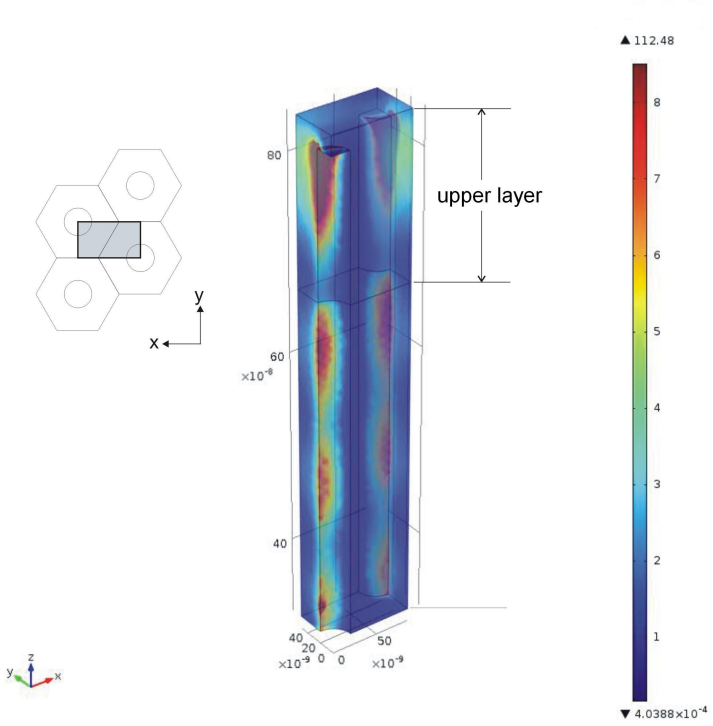

Fig. 2.5: An example of a near field intensity distribution for periodically arrayed Au nanowires. Note the shaded rectangular in the upper left corner. This area corresponds to the x-y plane of the volume on the right side. The circles on the upper left side correspond to the Au nanowires. This part is not shown in the volume on the right side.

2.3.2 Monte Carlo Simulation

Monte Carlo method (also known as statistical simulation method), is a numerical calculation method, which follows probability and statistical theory and refers to the use of random numbers (or pseudo-random numbers) to solve computing problems. [51, 52]

There are two main steps to apply to the Monte Carlo method when solving practical problems:

1. generating random variables with corresponding *probability distributions function* (PDF) is needed.

2. the numerical feature of the model is estimated by statistical methods, to obtain the numerical solution of the practical problem.

The Monte Carlo method is an effective method for finding numerical solutions for problems that are difficult to obtain analytical solutions or are not resolved at all because of computational complexity.

3. EXPERIMENTAL TECHNIQUES

3.1 Spectrophotometry

The UV/Vis spectrophotometer is typically used for quantifying the reflection or transmission characteristics of a material as a function of wavelength. As described in the previous chapter, when UV or visible light passes through the transparent material, an electron transition from the ground state to the excited state occurs by absorbing photons, and it results an absorbance as function of wavelength of incident light.

This absorbance $A(\lambda)$ is commonly defined as

$$A = -\log T = \log\left(\frac{I_0}{I_1}\right), \tag{3.1}$$

where T is the transparency, I_0 and I_1 are the intensities of the incidence light and the transmission light respectively. Moreover sometimes the optical path length d in the target should also be considered. Therefore, the absorbance of the material can be defined as:

$$\alpha = -\frac{1}{d}\log T. \tag{3.2}$$

A Cary 50 UV/Vis spectrophotometer and a Thermo Fisher Evolution 201 spectrophotometer were used for the experiments in this thesis.

3.2 Scanning Electron Microscopy

A scanning electron microscope (SEM) is a type of electron microscope that produces images of a sample by scanning it with a focused beam of electrons. The electrons interact with atoms in the sample, producing various signals that can be detected and that contain information about the sample's surface topography and composition. The electron beam is generally scanned in a raster scan pattern and the beam's position is combined with the detected signal to produce an image. SEM can achieve resolution better than 1 nanometer.

The most common mode of detection is by secondary electrons emitted by atoms excited by the electron beam. On a flat surface, the plume of secondary electrons is mostly contained by the sample, but on a tilted surface, the plume is partially exposed and more electrons are emitted. By scanning the sample and detecting the secondary electrons, an image displaying the topography of the surface is created.

SEM is one of the most versatile instruments available for the examination and analysis of the microstructure morphology and chemical composition characterizations. Since the discovery that electrons can be deflected by the magnetic field in numerous experiments in the 1890s [53], electron microscopy has been developed by replacing the light source with high energy electron beams [54]. We used a SEM setup of the group of Prof. W. Daum, a commercial SEM (Zeiss) in the group of Prof. M. Schilling, and also FE-SEM TESCAN MIRA3 in group of Prof. A. Waag.

3.3 Raman Spectroscopy

Raman spectroscopy is a nondestructive technique for the optical characterization of physical, chemical, and electronic properties of a sample. A Raman spectrometer consists of a Laser, the scattering geometry with optical elements and a spectrometer with single photon sensitivity. We have used a) a LabRam 800 Raman microscope (Jobin/Yvon HR 800) with 532 nm excitation in our laboratory and b) a similar setup at the PTB (Physikalisch-Technische Bundesanstalt), Abt. 3.14, Dr. Rainer Stosch. Confocal microscope are integrated and back scattering geometry is used in both setups. A photo of Jobin/Yvon HR 800 and a sketch of back scattering geometry is shown in Fig. 3.2 and Fig. 3.2, respectively.

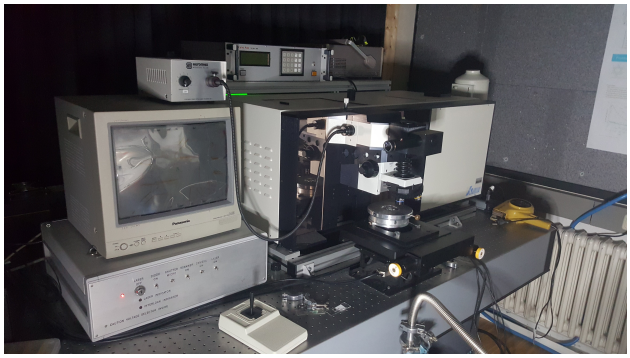

Fig. 3.1: A photo of Raman spectrometer Jobin/Yvon HR 800.

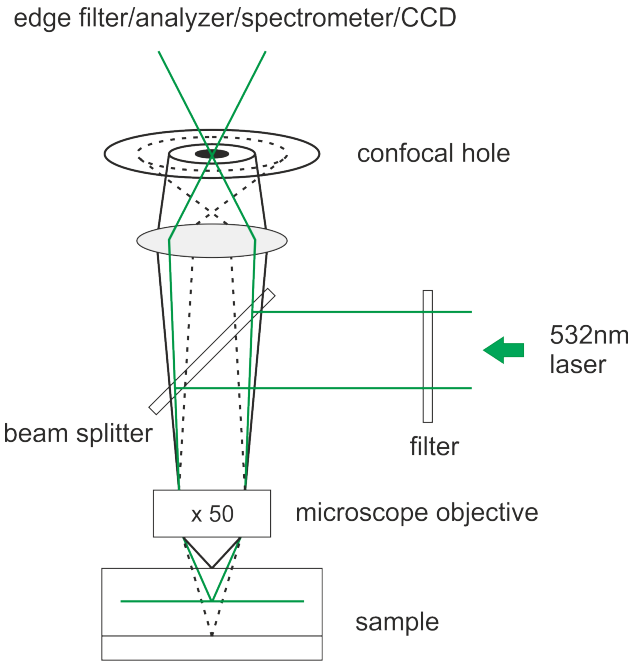

Fig. 3.2: Sketch of back scattering geometry used in both Raman setups.

3.4 Electrochemical Workstation

Two electrochemical setups have been used in the synthesis of nanostructures. a) VersaSTAT 3 workstation from Princeton Applied Research, and b) a self-built electrochemical system, which consists of one power supply, one multimeter and a computer, for higher potential experiments.

Fig. 3.3: A photo of VersaSTAT 3 workstation.

4. PERIODIC NANOSTRUCTURES

As mentioned in section 1.2, large area periodic nanostructures can be fabricated by the self-assembly template route. In this work, two sorts of templates, *Anodic Aluminium Oxide* (AAO) templates and *Polystyrene Sphere* (PS) templates are fabricated based on the top-down and bottom-up approaches, respectively. And our follow-up study on phenomena in long range periodic nanostructures are based on those templates.

4.1 Au Nanorod Array Based on AAO

4.1.1 Introduction

Anodic aluminum oxide (AAO) has been studied for over 80 years. [55] Since the pioneering work done by Keller et. al., [56, 57] who also revealed the structural details of porous anodic alumina first using an electron microscope in 1953 [57], a great interest in the porous AAO was attracted, cause its ordered microstructure and resource-conserving preparation. Later, after the development of highly ordered alumina membranes by Masuda and Fukuda in 1995, [58] more derived nanostructures based on this material have been reported. [59, 60]

Although the synthesis and application techniques of AAO have been successfully developed, the mechanisms of formation of the nanoscale pores is still controversial. [61]

In this section the preparation techniques of arrayed gold nanorods by utilizing porous AAO as a template is described in detail.

4.1.2 Preparation

4.1.2.1 Preparation of AAO Templates

Generally, an AAO film consists of a barrier layer and a porous oxide layer, an idealized scheme for that is shown in Fig. 4.1. The barrier layer is formed atop of the aluminum substrate with a uniform thickness, extremely thin and dielectrically compact. The porous oxide layer grows from this barrier layer. [62] As shown, the cells are hexagonally ordered with uniform size,

and each cell contains a pore in the center, which is perpendicular to the film surface.

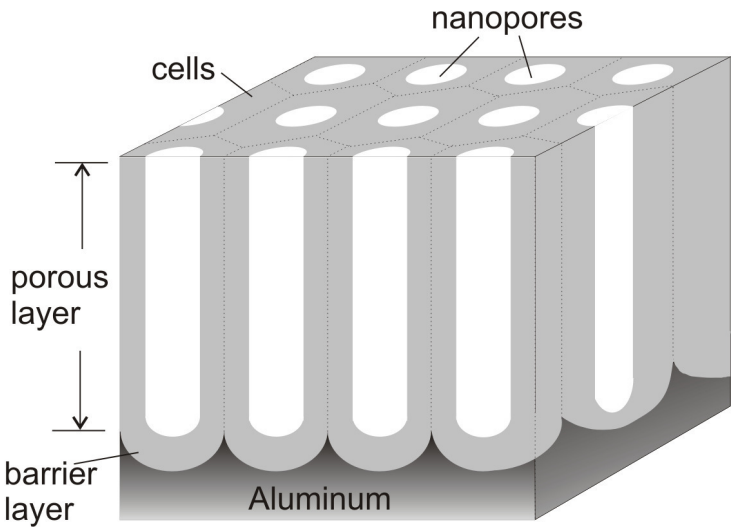

Fig. 4.1: AAO porous structure obtained from anodization.

For the synthesis of this kind of porous aluminium oxide, an anodizing reaction is performed in an acidic electrolyte, for instance, sulfuric, phosphoric, chromic [62] or oxalic acid, also in some mixed electrolytes [63, 64, 65]. In conventional processes which are named "mild anodization"(MA), self-ordered arrays of nanoporous AAO can be obtained within three narrow process windows, known as 'self-ordering regimes', see Tab. 4.1 [66]. In fact

Acid	Anodizing potential range(V)	Optimum potential(V)
0.3 M H_2SO_4	10 - 25	25
0.3 M $H_2C_2O_4$	30 - 100	40
1 M H_3PO_4	160 - 195	195

Tab. 4.1: Typical anodizing conditions in self-ordering regimes.

there is also another type of synthesis processes called "hard anodization" (HA) processes. However for the sake of simplicity the HA processes will be ignored here for AAO synthesises. Information about HA processes can be found in the literature [55].

For this thesis, we only used MA methods to fabricate the porous AAO membranes.

The following equations show the general reaction paths on different electrodes in the synthesis. On the anode, the reaction is given by

$$2Al + 3H_2O = Al_2O_3 + 6H^+ + 6e^- \ , \tag{4.1}$$

On the cathode, the reaction equation is:

$$6H^+ + 6e^- = 3H_2 \ . \tag{4.2}$$

In this thesis all AAO membranes are produced in a horizontal anodizing reactor, which is designed by Yan [66]. Fig. 4.2 shows a sketch of this reactor: Atop a temperature controller a copper plate is fixed. The copper plate is used as a connector for both electric and thermal conduction at the same time. A chemically polished aluminum foil is connected as an anode into the circuit via the copper plate. Electrolyte is filled into a Teflon cell and homogenized by a Teflon based stirrer driven by a motor. As a cathode, a platinum mesh is fixed over the stirrer. An electric power supply connects two electrodes and records the current data during the anodizing process.

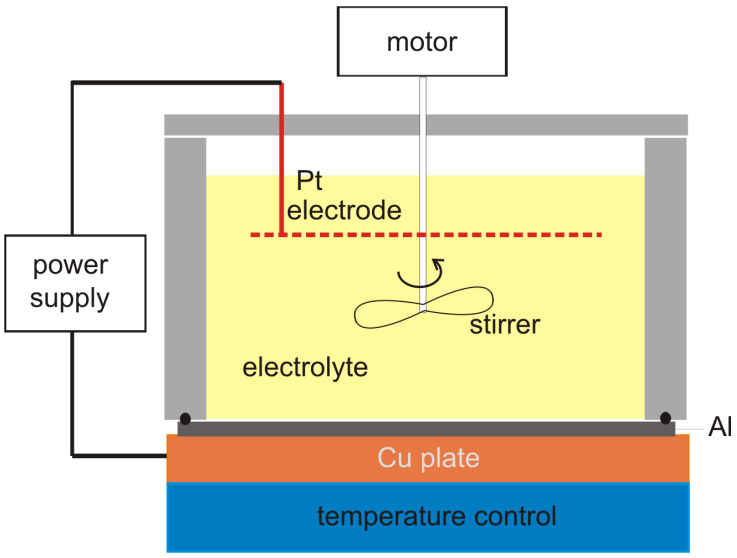

Fig. 4.2: Anodization setup.

To synthesize a porous AAO membrane, a pre-treatment of aluminium substrate is necessary. First, an aluminium foil (thickness 1 mm with high purity 99.99%, Beijing Cuibolin Ltd.) is ultrasonically cleaned in acetone and deionized water for 20 minutes to remove contaminations, respectively. Then the aluminium foil is annealed in air at $400-500°C$ for $4-5$h to reduce the stress in the material. Subsequently, an electrochemical polishing process is carried out in a mixture composed solution of $HClO_4$ and C_2H_6O with a volume ratio of 1 : 4, under a 20 V polishing voltage for 4 minutes. After polishing, the aluminum surface should be smooth and shiny [67].

Following the pre-treatment, the polished aluminium foil is fixed in the reactor. Consequently the first anodizing reaction is started by exploiting the

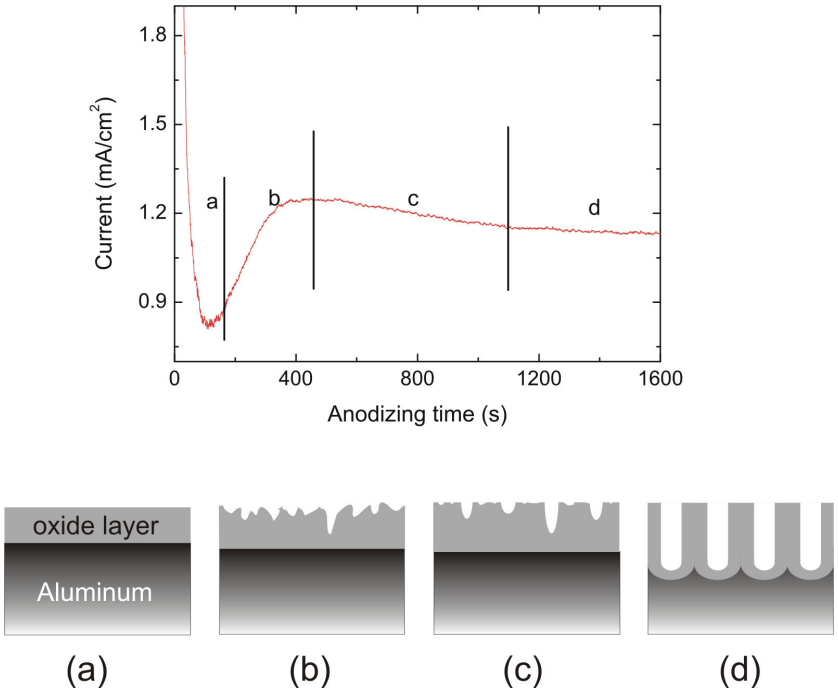

Fig. 4.3: Current curve and the formation of pores at certain anodizing time [68].

forming potential. Although in different electrolytes, in fact, the current-time (I/t) curves of 'mild anodization' (MA) processes present the same tendency. As an example, an I/t diagram of an anodizing process in oxalic acid is shown in Fig.4.3.

According to the I/t diagram we divide the formation process into four different stages: a) After switching on a constant voltage supply, the current decreases steeply with time until the local minimum is reached. In this stage, an oxide layer grows on the interface of the electrolyte and aluminum, which is non-porous with a homogeneous thickness. b) Subsequently the current increases to a steady point. In this stage, we think, pore precursors are randomly dissolved into the electrolyte from the oxide layer surface and the origin of these precursors are surface defects. c) The current decreases gradually. Further growth and widening of pores result from the dissolution, and at the same time the growth of the barrier layer is more stable. d) Finally the current is nearly constant. At this stage, an equilibrium between formation and dissolution of the oxide layer is reached at the electrolyte-oxide interface and oxide-metal interface [66].

In order to get a highly ordered honeycomb-like structure, a two-step anodization method is exploited: After the first anodization, the self-organized porous oxide layer is removed by a chemical etching, which is carried out in

a mixed solution containing 6% H_3PO_4 and 1.8% H_2CrO_4 in a water bath at 60°C. After this etching, small pits, which will work as seeds for the next anodization, appear ordered on the surface of remaining Al substrates. Then we repeat the anodization process on this substrate once again.

Details of anodization parameters in the whole process are shown in author's publication [36].

In order to carry out a further electrochemical deposition as a post-treatment, the Al substrate and alumina barrier layer is removed. For that, HCl and $CuCl_2$ mixture solution and 5% H_3PO_4 solution are used, respectively.

After the post-treatment, we obtain free-standing porous AAO membranes.

To characterize the honeycomb-like structure morphologically, a few parameters, such as pore diameter, interpore distance and membrane thickness are desired. These parameters can be determined mainly by anodizing conditions, see Tab. 4.2. Considering the size-effect of LSP, which was described in Section 2.1.2, sulfuric acid made AAO membranes, shown in Fig 4.4, are applied as template for later Au nanowires deposition.

Acid	0.3 M H_2SO_4	0.3 M $H_2C_2O_4$	1 M H_3PO_4
Forming potential(V)	25	40	195
Pore diameter(nm)	25	60	200
Interpore distance(nm)	63	100	500

Tab. 4.2: Typical pore parameters of obtained AAO [68].

4.1.2.2 Preparation of Au/AAO Arrays

Before electrodeposition, a 300 nm Ag layer is sputtered on one side of AAO as an electrode for the electrodeposition of the nanowires. A platinum mesh is employed as a counter electrode, and a Ag/AgCl (saturated KCl solution) electrode is used as a reference electrode. As Yan reports[66], Auruna 5000 (gold content 7 g/L)is used as a electrolyte with a pH value of 6. A constant current mode with 382 $\mu A/cm^2$ is used to deposit Au nanowires into the pores, and the average growth rate is about 3 nm/second.

After deposition of Au nanowires, the Ag layer is removed by dropping HNO_3 on the Ag surface. The HNO_3 can totally dissolve the silver meanwhile keeping the Au structure intact. Now, the synthesis of AAO/Au component of the nanostructure is finished.

Furthermore, in order to obtain a bare Au nanowires array in air, we can also etch AAO layer partly away from the AAO/Au structure surface by

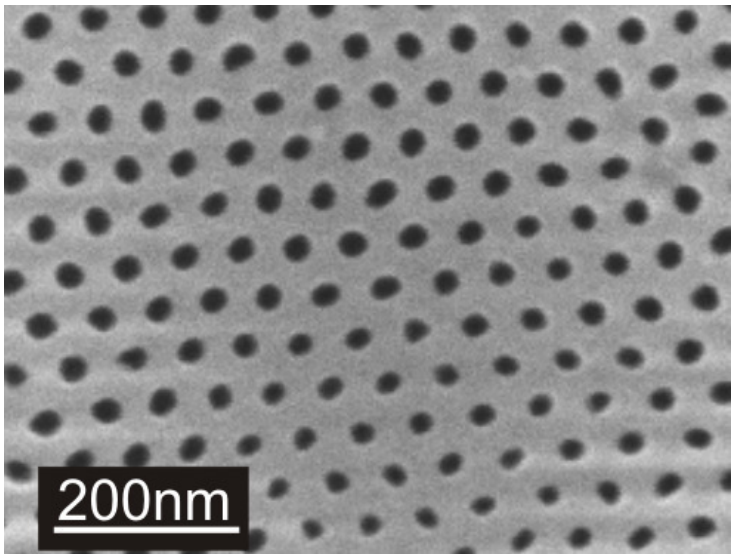

Fig. 4.4: SEM image of a H_2SO_4 made AAO [68].

exploiting H_3PO_4.

We have prepared both structures for different aims in our experiments.

As a simple summary, the whole progress of synthesis are shown in Fig. 4.5. It contains: a) Pre-treatments of Aluminium. b) Process of anodization. A nanoporous structure is formed in the phase. c) and d) Post-treatments of AAO. These are used to remove the remaining aluminium substrate and the barrier layer, respectively. e) Sputtering an Ag layer as an electrode. f) Au nanowires deposition. g) Dissolution of Ag layer. h) Etching AAO partly away from the surface. For getting a highly ordered structure, process b) should be performed twice, before the post-treatments. Both products shown in g) and h) are used in our experiments. Details of all chemical synthesis process are shown in author's previous publication [36].

4.1.3 Characterization

Fig. 4.6 shows typical morphological details of Au nanowires by a SEM image, which has been provided by Yan [68].

We can also etch AAO layer partly away from the AAO/Au structure surface by exploiting H_3PO_4. Fig. 4.7 shows the SEM image of this bare Au nanowires structure.

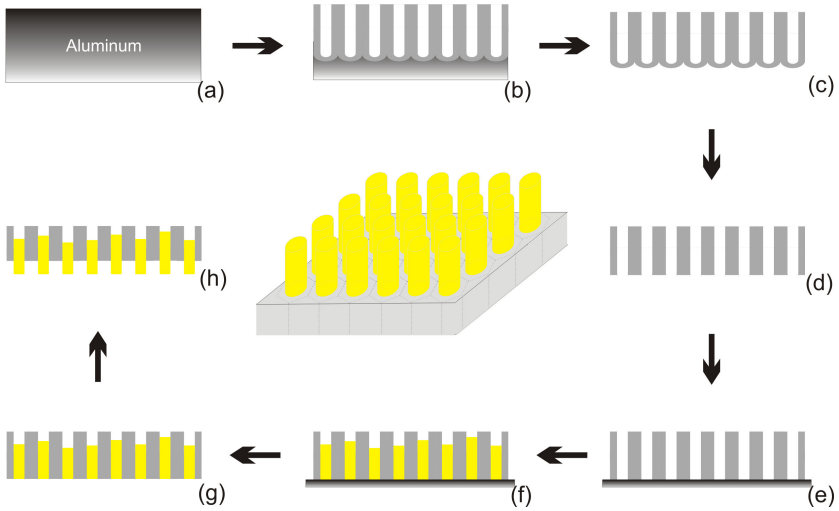

Fig. 4.5: Preparation process of Au nanowires within AAO.

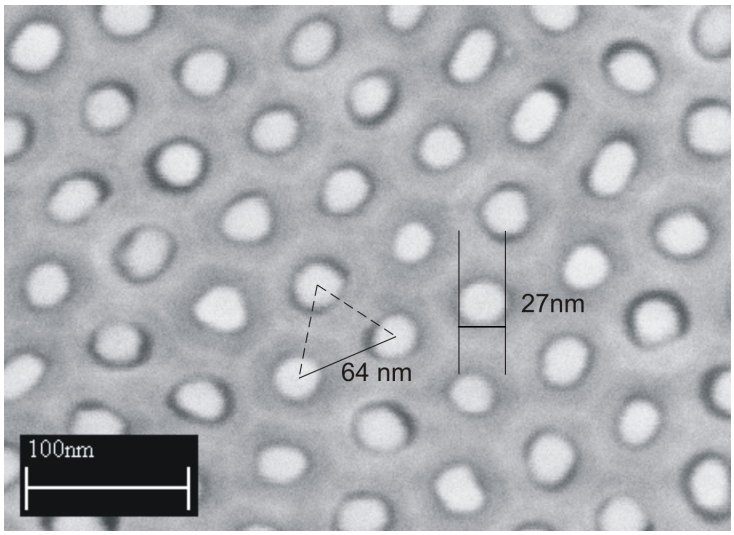

Fig. 4.6: Details of Au nanowires in AAO pores. Note that small gaps between Au nanowires and AAO material exist.

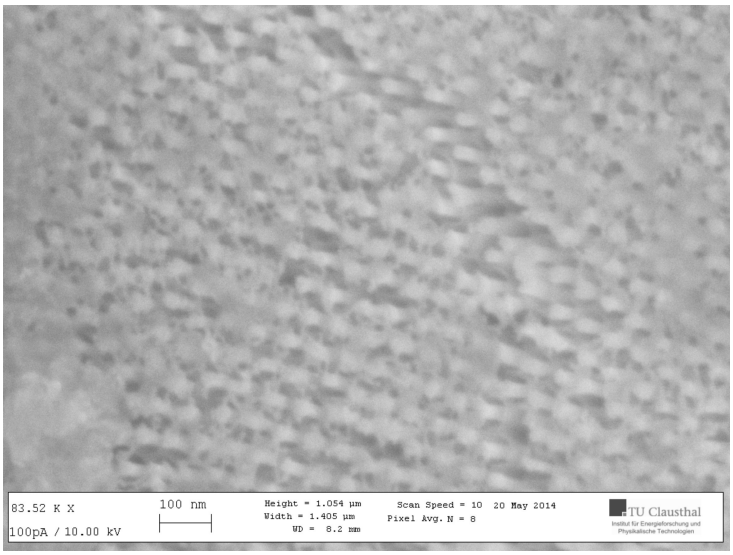

Fig. 4.7: SEM image of an etched AAO/Au structure with etching time 30 min. The AAO membrane is prepared in sulfuric acid. We found that an etched AAO/Au structure with clean surface has a very strong charging effect during the SEM process. We show here a SEM image of AAO/Au with additional pollution.

4.1.4 Simulation

By exploiting the Finite Element Method (FEM), absorption and Rayleigh scattering processes are numerically calculated.

We developed two models to fit our different experiments: Model A is made for simulation of a non-etched AAO/Au, in which Au wires are totally surrounded by AAO material except the top surface. Meanwhile Model-B is built for the case of an etched AAO/Au structure, in which a 280 nm AAO layer is removed form the top surface. Therefore, in Model-B, the upside of Au wires is exposed in air.

In the simulation of model A, we are interested in the Joule heat loss of Au wires. The power of Joule heat loss is shown as a function of the incident light wavelengths in Fig. 4.8. We can see that in the higher energy range between 400 and 520 nm the heat loss slightly decreases firstly until 440 nm, and then the curve goes up. At about 520nm the heat loss curve reaches a maximum. After that, from 520 to 900 nm, the heat loss keeps growing down, with a gradually decreasing slope.

In the next section, we will compare this Joule heat loss with the absorbance of AAO/Au structure, to find out the origin of the absorbance (or transparency) in our AAO/Au structure.

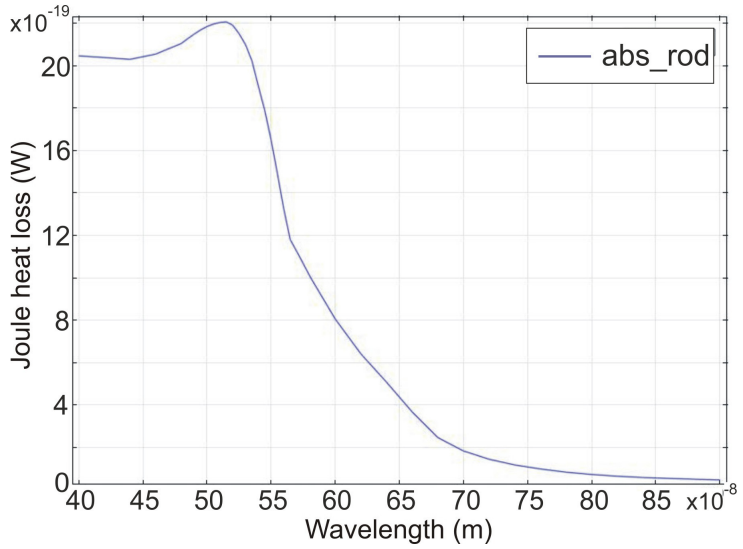

Fig. 4.8: Joule heat loss of a single Au nanowire.

We are also interested in the distribution of near electromagnetic field in both model A and B, when they are illuminated by a 532 nm plane electromagnetic wave, which has a wave vector along $-z$ direction and has y-polarization. For both models, we only show a spatial volume with 280 nm depth in z direction, as we detailed in section 2.3.1. The numerically calculated light intensity distributions of model A and model B are shown in Fig. 4.9 (a) and (b) respectively. In the simulation we assume that the amplitude of the wave E is 1 V/m. Note that the legends show the E^2 value. In our case this value can be considered to be the light field enhancement coefficient.

Image (a) shows the light distribution in the upper 280 nm AAO layer. We notice that for a y-polarized light the intensity contribution is concentrated around the Au nanowire surface in y direction. In x direction the intensity has no enhancement. The obvious enhancement region appears only in the upside of the AAO, near by the upper surface. Let the coordinate origin be in the center of the Au nanowire. Starting from the origin, we consider the intensity of the contribution along the y-axes. At the interface between the Au nanowire and AAO the enhancement decays along y directions dramatically. There is also a similar decay in $-z$ direction.

Distribution image (b) shows that the intensity enhancement is concentrated also in y direction. Moreover in this 280 nm air layer another obvious enhancement region appears. Comparing Model-A with Model-B the near-field has a higher average intensity in the volume as shown.

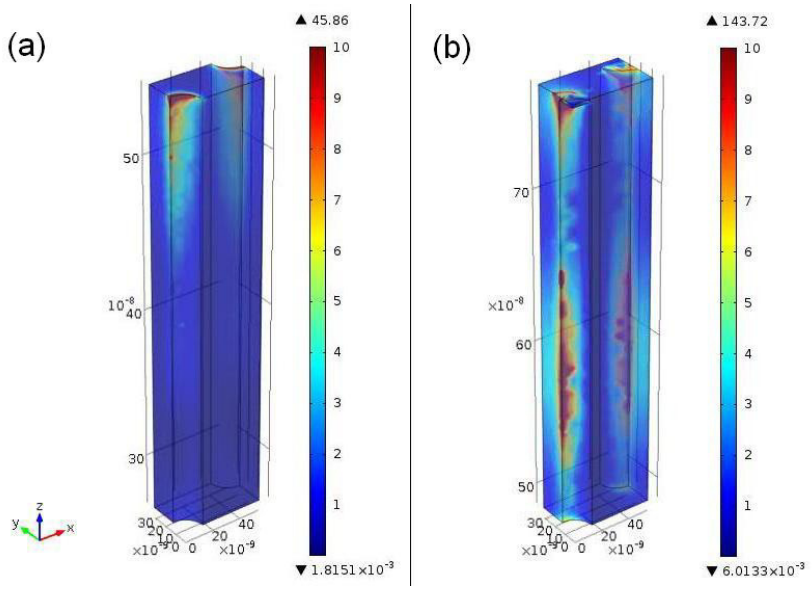

Fig. 4.9: Near-field distributions of light intensity.(a) Light distribution in the upper 280 nm AAO layer. (b) Intensity distribution in a 280 nm air layer. Legends show the E^2 values without units.

4.1.5 Results and Discussion

Fig. 4.10 presents the absorbance of pure AAO. As it is shown, porous AAO has a band gap of around 3.75 eV, and it is almost transparent in the visible range of the spectrum. For a 532 nm (2.33 eV) laser our pure AAO nanoporous membrane is totally transparent.

After the deposition of Au nanowires into AAO, a new transmission character emerges, which is shown in Fig. 4.11. Now, by bare eyes a brownish-red color of the AAO/Au structure can be observed. We have reasonable grounds for believing that the transparency modification is attributed to the strong absorption of the Au nanowires LSP resonance (LSPR) that occurs in transverse direction (T mode) at 520 nm. This can be proven by comparing the absorbance curve with the numerical calculated Joule heat loss in Fig. 4.8. When rotating the film to a non-vertical position as reference to incident light axis, another pronounced mode can be found. It results from the longitudinal mode of the Au nanowires' LSPR. Therefore, for a 532 nm laser our AAO/Au nanowire structure has a low transparency.

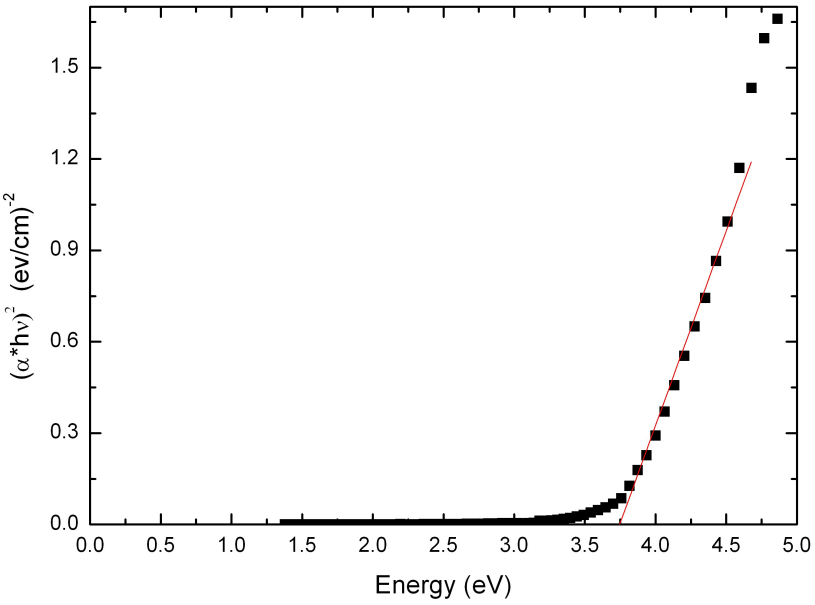

Fig. 4.10: Absorbance spectrum of AAO [68].

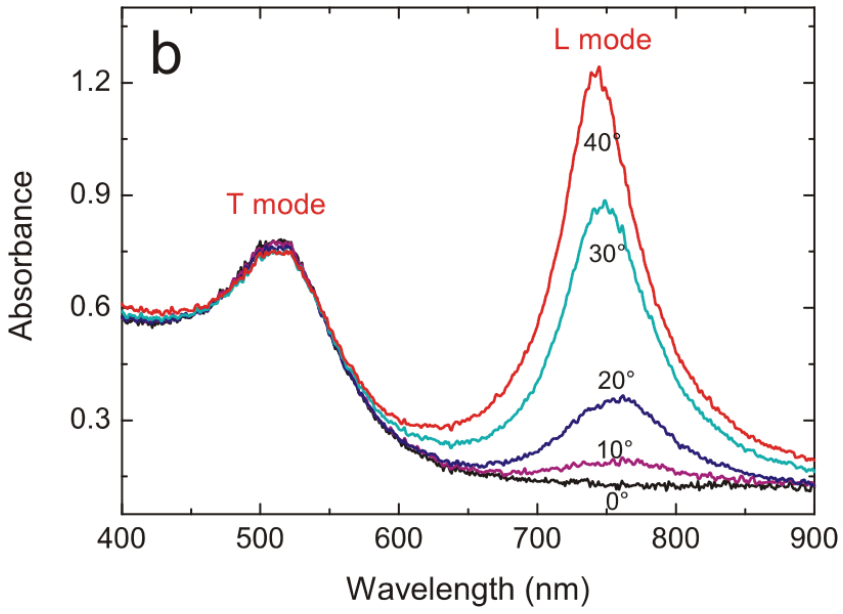

Fig. 4.11: AAO/Au transmission under different angles of incident light [68].

4.2 Nickel Inverse-Opal Nanostructures

4.2.1 Introduction

The metallic inverse-opal structure is of both applied and fundamental interest. So far, many papers have delineated the preparations of metallic inverse opals also for photonic, magnetic, sensing, and electrochemical devices. From application point of view, a Ni inverse-opal structure which is prepared in this work, is a nanoporous structure. It has a large surface area and also a high conductivity. Therefore, it is one of the potential candidates of electrode structure in batteries, such as in Ni-Cd system, to further improve the capacity of batteries and performance of the quick charging. Moreover, a Ni inverse-opal structure can be also applied as a highly effective catalyser in chemical industry, transpiration cooling materials in space technology, etc. At the same time, the Ni inverse-opal structure can perform as a two and three-dimensional articial spin ice and attracts also theoretical attentions. [69]

4.2.2 Preparation

To fabricate Ni inverse opals, an assembly of microspheres made of silica or polystyrene ($(C_8H_8)_n$, *PS*) is often used first to produce colloidal crystals. Following that an electrochemical or a chemical deposition is carried out to fill Ni within the interstitial voids among those close-packed microspheres. The encapsulated microspheres can be selectively removed, leaving a Ni skeleton as the inverse opal. [70]

In contrast to the top-down approaches such as the one described in section 4.1.2.1, a periodic template, a self-assembly of PS colloidal crystals, is usually fabricated by using bottom-up approaches.

A self-assembly PS template consists of a large amount of polystyrene spheres with a hexagonal close-packed structure. Several self-assembly methods are commonly used to achieve such structure, and can be categorized by technical details: electrophoretic deposition, vertical deposition, etc. [71, 72, 73]

Thereunder the vertical deposition method is one of the most widely used methods of preparing PS templates, due to small equipment requirements and cost. [74] In this work, the self-assembly opal structure PS templates are prepared by a vertical deposition method. Based on the PS template, inverse-opal structured Nickel layer are fabricated by electrochemical deposition.

4.2.2.1 Preparation of Opal Structure by Polystyrene Nanosphere Self-Assembly

The working principle of the vertical deposition method is described in the following: A substrate is placed vertically in the suspension of monodispersed colloidal microspheres, and a relative motion of the substrate and solution is established. During the evaporation of the solvent, the liquid surface sinks and the orientation of the microspheres is achieved by the surface tension of the solid-liquid interface. Therefore a layer of colloidal particles is formed at the junction of the substrate and the liquid surface, i.e., colloidal crystals are formed. A sketch of working device is shown in Fig. 4.12.

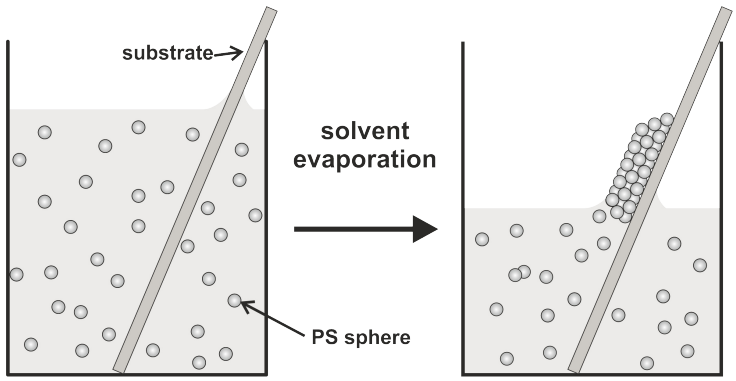

Fig. 4.12: A sketch of working principle of vertical deposition.

With this method the thickness of the colloidal crystal can be controlled by the concentration of the microspheres suspension and the rate of solution evaporation. For larger size microspheres, a temperature gradient can also be introduced to accelerate the convective motion of the microspheres in the liquid to achieve perfect deposition of colloidal crystals. [74]

In the experiment, aqueous suspensions of highly monodisperse PS spheres (500 nm in diameter) and ITO (Indium Tin Oxide) coated glass (2 cm $\times$ 2 cm, *Sigma-Aldrich*) with a sheet resistance of 8 ohms were used. The working procedure of the vertical deposition in this work holds:

1. Cleaning of ITO glass substrate. The ITO glass was washed with a mixture of detergent and water, and then ultrasonic cleaned for 15 min with acetone, ethanol and deionized water, respectively. Then ITO glass was placed in a beaker containing deionized water.

2. Preparation of microspheres suspension. 10 ml of deionized water was placed in a clean weighing flask and then 175 μL of a PS microsphere

solution with a solid concentration of about 12% was pipetted into the weighing flask to obtain suspension with solid concentration of 0.24%.

3. Evaporation of solvent. Place the prepared ITO glass in the weighing flask containing the suspension, with approximately 80 degrees angle with the liquid level. The weighing flask was placed in a thermostat incubator(VWR INCU-Line IL 10), and the temperature was controlled at 45°C. Any vibration should be avoided during the evaporation process, which can take around four days. After that, a PS sphere nano inverse-opal template is achieved.

4.2.2.2 Preparation of Nickel Inverse-Opal Nanostructures

Based on the PS sphere inverse-opal templates, nickel structures are fabricated by electrochemical deposition (electroplating). A sketch of the working device is shown in the Fig. 4.13. The whole system consists of a computer, an electrochemical workstation and a reactor, in which ITO/PS sphere inverse-opal templates and a Pt electrode are immersed by the electroplating solution. The deposition area, which immersed under the electroplating solution, was controlled to be around 2 cm^2 in each fabrication. The electroplating reaction happening on the ITO electrode is

$$Ni^{2+} + 2e^{-} = Ni, \tag{4.3}$$

In practice, many different plating solution recipes can be used in electrochemical deposition of Ni, for instance, *Watts Baths* (with composition $NiSO_4 \cdot 6\,H_2O$, $NiCl_2 \cdot 6\,H_2O$ and H_3BO_3), *nickel sulfamate bath* (with composition $Ni(SO_3NH_2)_2$, $NiCl_2 \cdot 6\,H_2O$ and H_3BO_3) and *all-chloride bath* (composition $NiCl_2 \cdot 6\,H_2O$ and H_3BO_3).[75] Moreover, the deposition process can be also influenced by adding brighteners, e.g., *benzenesulfonic acid* ($C_6H_5SO_3H$), *N,N-diethylethynamine* ($C_7H_{13}N$). In this work a Ni plating solution consisting of $NiSO_4 \cdot 6\,H_2O$ (130 g L^1), $NiCl_2 \cdot 6\,H_2O$ (30g L^1) is used without any brightener. The electroplating is conducted at 3 μA, and its duration is adjusted between 1 and 5 min, allowing the deposition of Ni structure into a desirable height.

After Ni deposition, the PS microspheres were carefully removed by immersing in ethyl acetate 95 wt% solution for 16 hours at room temperature, then washed by acetone and dried in air.

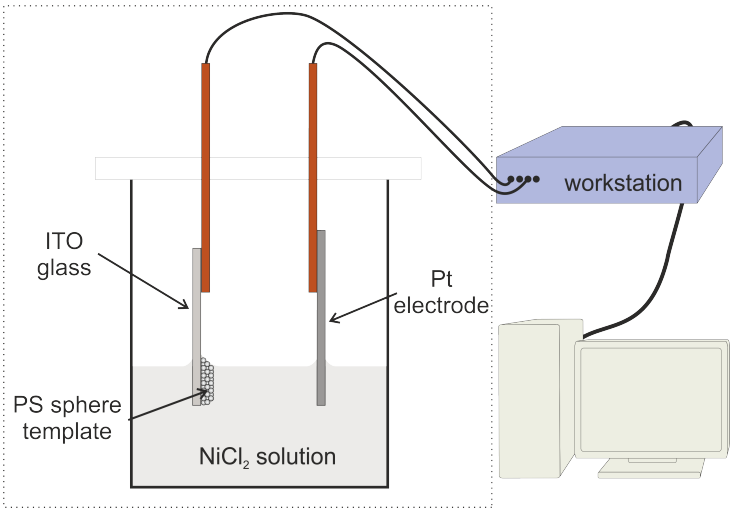

Fig. 4.13: A sketch of working device for Ni deposition.

4.2.3 Characterization and Discussion

SEM experiments were performed by using TESCAN MIRA3 after the sample were dried. Fig. 4.14 shows the SEM pictures for the Ni inverse opals with few layers in top-view. Apparently, the Ni formed a continuous network, encompassing hexagonal arrays of pores left by PS microspheres, which have a diameter of 500 nm. As shown in Fig. 4.14 a, a long range (dozens of micrometers) integrity is achieved. The thickness(or number of layers) of the Ni structure is controlled by the duration of the electrochemical deposition. For a few-layered structure shown in the figure, 100 seconds deposition is applied in the experiment. The growth of Ni is perpendicular to the surface of ITO surface, deposition rate is spatially homogeneous and top-surface of the deposition displays an impressive height consistency as shown in the SEM image.

In literatures, Ni overgrowths and height variations were observed once the electroplating was overextended to layers above 7. [70] Hence, for our purpose of study on 2D metamaterial, the thickness for the inverse opals was limited to few layers to achieve 2D properties.

On the left-down corner of Fig. 4.14 a, as an example, two defects of structure show up. These are formed due to air bubbles, which stick on the surface of ITO glass or in the PS colloidal crystal during immersing the PS sphere template in to the depositing solution. A functionalization of ITO surface would be helpful to avoid such defects in the further experiments.

Remarkably, as shown in Fig. 4.14 b, the size of the voids agreed with the diameter of the PS microspheres, showing that a obvious swelling of the PS

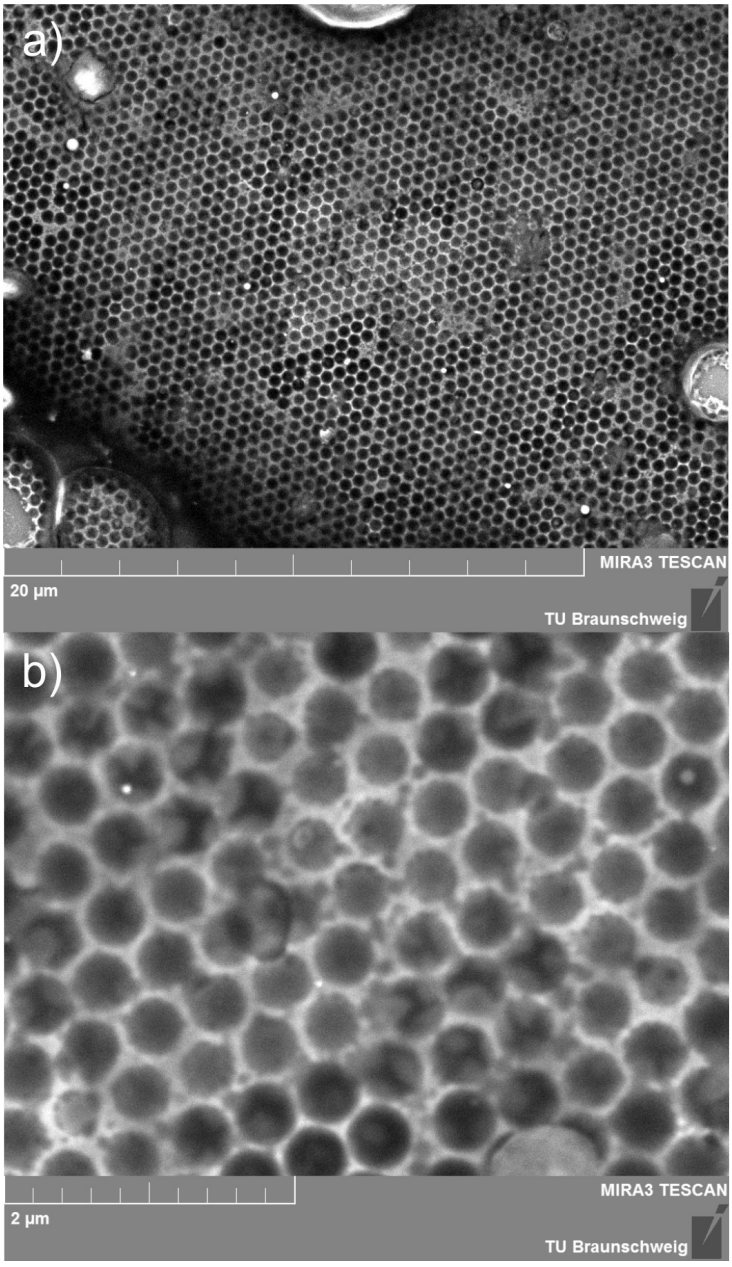

Fig. 4.14: SEM image of Ni inverse-opal nano structure. The Ni network maintained a remarkable structural integrity without notable defects.

microspheres did not occur during the removal process.

This structure can be applied in both application and study on spin ice as a future topic.

5. INTERACTION BETWEEN EXCITONS AND SURFACE PLASMONS

5.1 Introduction

In condensed matter physics quasi particle concepts are broadly used to model periodic many body systems. The complex interactions among lattice, spin, orbital, and charge and etc. lead to the complexity and charming variety of characters of a matter. To describe interactions between quasi-particles is one of the most interesting elementary tasks from condensed matter of physical point of view. In this chapter, the interaction between two quasi particles surface plasmon and exciton will be discussed.

In the last decade, increasing attention has been captured by surface plasmons of metallic nanostructures and the interaction of surface plasmons with quantum emitters such as, quantum dots or dye molecules. [76, 77, 78, 79] Such nanostructures offer the opportunity to control light-matter interaction on subwavelength length scales. Except the fundamental interest, which has been mentioned hereinabove, possible applications based on such interaction are related to sensing and photonic information processing. [80, 81]

The theoretical modelling of light-matter interaction usually relies on classical electromagnetic models. [82, 83] It is based on a frequency-dependent, complex dielectric function $\epsilon(\omega)$ that is used to represent each individual part of the nanostructured system. If the size is reduced to the nanometer scale, however, the bulk dielectric function $\epsilon(\omega)$ has to be corrected in order to extend the validity of the classical approach. [84, 85] Besides, numerical simulations of Maxwell's equations can not completely represent the interactions between quasi-particles, for example, plasmons and excitons. [86] Therefore, a more microscopic, quantum mechanical point of view is required. Such an approach would also provide a more complete understanding of plasmon-exciton interactions in nanostructured, plexcitonic systems. [87]

Several quantum mechanical treatments are presently evaluated. [88, 89, 90, 91, 86, 92] In particular, time dependent density functional theory (TDDFT) relying on quantum modeling or quantum-corrected modeling, seems to be

promising, but it suffers from a limited calculation volume. [90, 91] The Dicke model can be applied to a many emitters case within the low excitation limit. [92] The Zubarev Green's functions approach introduced by Manjavacas [86] can be applied to describe the optical absorption of systems, which consist of a single exciton-supporting quantum emitter and a single nanoparticle or a nanoparticle dimer. It is still challenging to deal with extended plexcitonic systems having a larger number of internally interacting nanostructures by exploiting a quantum treatment.

In this work, strong coupling between surface plasmon and molecular excitons in nanoarray-molecule plexcitonic systems has been achieved, and it's demonstrated, that collective surface plasmons within the internal interacting plasmonic structures can be treated approximately as single quasiparticles. This treatment leads to an analytic and microscopic description of the optical response of the hybrid plexciton. This approach is helpful for a fundamental understanding of the underlying phenomena and also to guide the design of devices based on strong coupling between exciton of organic molecules and surface plasmon, for which dielectric function simulation is only of limited suitability.

5.2 Experiment

Periodic Au nanorod arrays with a quasi-hexagonal superlattice are prepared based on electro-deposition of Au wires into anodic aluminum oxide (AAO) porous templates. [93, 94, 95] The templates establish the overall geometry by defining the diameter and distance of the Au nanorods, and they also contribute to the effective dielectric constant of the array. A respective preparation scheme is given in Fig. 5.1(a).

AAO nanoporous templates are fabricated by a standard two-step anodization process . [67, 95] The aspect ratio (AR) of the Au nanorods in the arrays is controlled by varying the duration of electrochemical deposition to be in the range of 7 to 15. A typical SEM image of the top-plane is given in Fig. 5.1(b). Here, the white dots correspond to the Au nanorods, which are surrounded by the AAO template in the plane. The Au nanorods have a diameter of $D_w \approx 23\ nm$ and form a hexagonal superlattice with an inter-rod distance of $D_{int} \approx 63\ nm$. In Fig. 5.1(c) absorption spectra are shown taken at room temperature using a UV/Vis-NIR spectrometer (PE Lambda 900) of an Au nanorod array with AR = 15. Part of this work is published in Ref. [36].

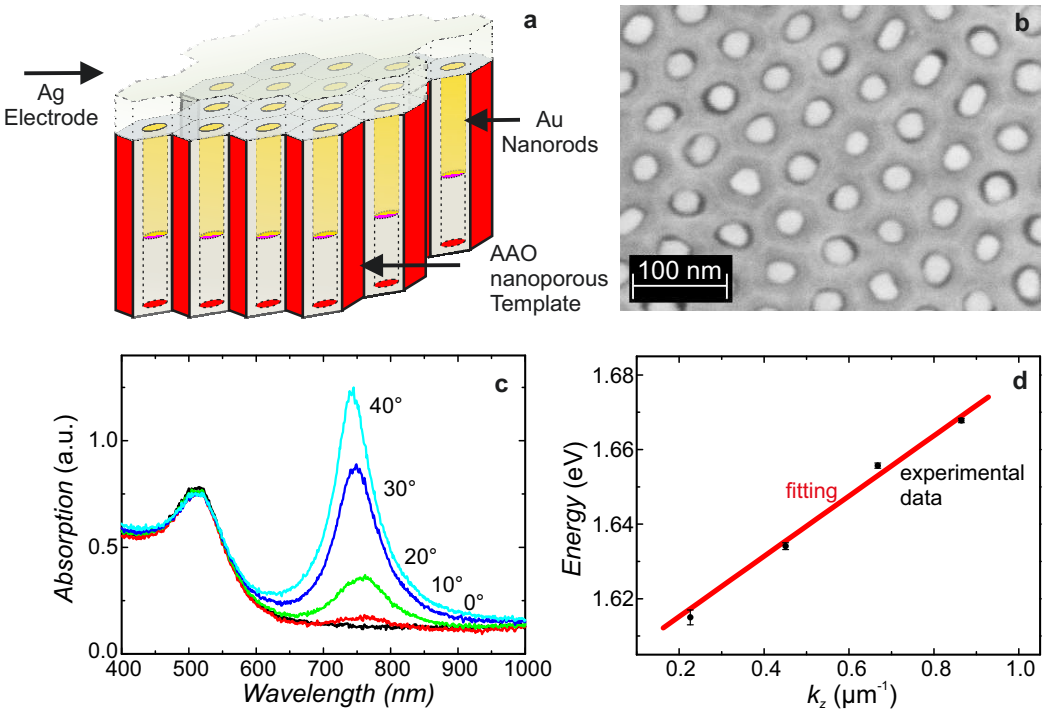

Fig. 5.1: a) Preparation scheme of Au naonorod arrays. Au rods are deposited into the open holes of the AAO template. b) SEM image of the top-plane after removing the Ag electrode. White dots arranged with the hexagonal supperlattice correspond to the cross section of the Au nanorods. c) Normalized absorption spectra of the Au nanorod array with varying angle θ of incidence with respect to the top-plane. d) Dispersion of the collective L-mode within the array. [36] Reprinted with permission.

5.3 Results and Discussion

5.3.1 Experimental Results

A series of spectra was obtained while changing the incident angle from 0° to 40° between the incident direction and the normal of the array plane. Two maxima are observed if the incident light polarization has an electric field component both along and perpendicular to the long axis of nanorods. The two peaks at $\lambda_{Max-T} = 510\ nm$ and $\lambda_{Max-L} = 750\ nm$ are attributed to the transverse (T) and longitudinal (L) resonance of the Au nanorods, respectively. [96] This assignment agrees well with the observation of an extreme low intensity of the L-mode when no electric field component parallel to the long axis of nanorods exists, as shown by the $\theta = 0°$ incidence (black curve) in Fig. 5.1(c). Meanwhile, the intensity of the T-mode should not depend on the incident angle of a linear polarized light, because of its localized surface plasmon-like behavior and the invariant extinction cross-section with different angles.

Comparing these data with observations on isolated Au nanorods, two peculiarities become apparent: a) the energy of the L-mode is much higher compared to that of an isolated Au nanorod with the same aspect ratio. In the latter case it should be observed as a maximum in the infrared region with a wavelength larger than 1700 nm. [97, 98] The pronounced blue shift from 1700 nm to 750 nm corresponds to an effective interaction between the nanorods in the array.[99] As reported earlier, such an interaction between two parallel Au nanorods depends on D_{int} and also on the AR of each nanorod. When D_{int} is relative small and the AR is relatively large, the blue shift of the absorption maximum is larger. [100] For our case with AR = 15 and $D_{int} = 63$ nm it is only reasonable that not only two neighbors interact with each other. In contrast, the coherence length of the surface plasmon is estimated as $l_{coh} = t_{plasmon} \times v_{plasmon} = 320$ nm, which is a factor 5 larger than the superlattice constant D_{int}. The low energy maximum therefore corresponds to a collective longitudinal mode of the array. b) The L-mode shifts with the angle of incidence, [101] i.e. by 4% to higher energy while the angle of incidence increases from 10° to 40°. Figure 5.1(d) shows the resulting dispersion diagram of the L-mode energy as function of in-plane momentum. The resulting quasi-linear dispersion relation matches quite well to simulations. [102] From the dispersion a quasi-constant non-zero group velocity $\frac{\partial\omega}{\partial k} \approx 1.168 \times 10^8$ m/s of the propagative plasmon mode is derived.

Using templates with Au wire arrays is of advantage as the resonances can be tuned by varying aspect ratio, distance and the angle of incidence on the template. Thereby both a rough adaption and a fine-tuning of the working

wavelength/energy can be achieved allowing to use emitters with excitonic energy that cannot be adapted easily. In our studies we use the highly efficient and chemically stable Aza-BODIPY (boron-dipyrromethene). [103] For the preparation, 6 μL Aza-BODIPY solution in $CHCl_3$ with a concentration of 10^{-5} mol/L is dropped on the surface of the Au nanorod array and the solvent is allowed to evaporate.

As shown in Fig. 5.2(a), Aza-BODIPY has an absorbance maximum at around 648 nm (thin line), being very close in energy to the collective L-mode of Au nanorod arrays. Tuning the aspect ratio two limiting cases are achieved; (a) strong coupling with coinciding energies of the collective L-mode and the molecular excitons and (b) weak coupling with disagreeing energies. Please notice that a weak coupling in our context is associated with a vanishing splitting. In Fig. 5.2(a), an equidistant splitting by $\pm$153 meV of the previously observed absorption maximum into two broad but well separated maxima is observed. The respective maxima are hybrid plasmon-exciton branches. Such effects are characteristic for strong coupling and the two maxima can also be described within the scheme of Rabi oscillations of a two-level system. [104, 105] The absorption maxima of two hybrid branches in our observation are rather broad due to 1) variation of the coupling strength between the L-mode and exciton induced by sample inhomogeneities, and 2) lifetime effects of each of the hybrid branches due to strong coupling between broad L-modes and excitons.

In Fig. 5.2(b), corresponding data of the same porous AAO structure but including Au nanorods having a larger AR are shown. The L-mode energy is now observed as a maximum at 685 nm (thick red line). Applying the Aza-BODIPY solution under the same conditions there is only a small shift of the maximum by 16 nm. This effect can be attributed to the variation of the dielectric environment around the Au nanorods by the dye molecules. Hence, there is only a weak coupling of the exciton and the plasmon. Please notice that, comparing with Aza-BODIPY molecules, Au nanorods absorb the incident photons much more efficiently due to the more pronounced light-matter coupling of the plasmon. Furthermore, in both strong and weak coupling cases, the total number of Aza-BODIPY molecules on the array is so small, that no apparent peak of uncoupled Aza-BODIPY is observed. This can be derived from Fig. 5.2(b).

5.3.2 Modelling

In order to model the absorption of plexcitonic systems, a Zubarev's Green function method is evaluated following the work of Manjavacas et al. [86]

Here, the interaction between one quantum emitter and one single or one

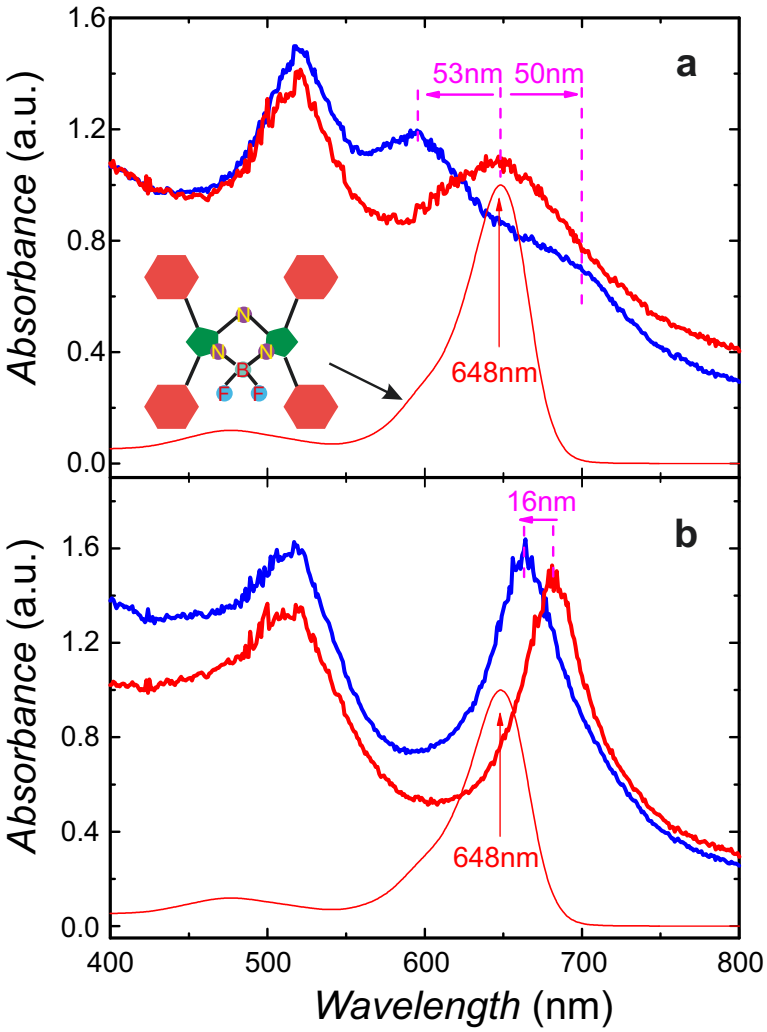

Fig. 5.2: Optical absorption of Au nanorod AAO templates (thick red line) and templates decorated with Aza-BODIPY molecules (thick blue line). For comparison the optical absorption of Aza-BODIPY in dilution is shown (thin red line). The inset shows a sketch of the molecular structure of Aza-BODIPY. a) Data of a template with coinciding characteristic energies, denoted as strong coupling. b) Data of a template with differing characteristic energies of plasmons and molecules, denoted as weak coupling. [36] Reprinted with permission.

pair of metallic nanoparticles is considered.

The mathematical derivation of model is given in the author's previous work [36] and the supporting information for literature [86].

The Hamiltonian of the hybrids is described with $H = H_0 + H_{int} + H_{decay}$ in Manjavacas's model, where H_0 describes the noninteracting evolution of the emitter and plasmons; H_{int} describes the elastic plasmon-emitter interaction; H_{decay} describes inelastic interactions. Each term, for instance, $H_{int} = -\sum_{j\neq i}^{N}\sum_{i=1}^{N}\Delta_{d_i d_j}[d_i^\dagger d_j] - \sum_{i=1}^{N}\Delta_{d_i c}[d_i^\dagger c + c^\dagger d_i]$ includes $\sim O(N^2)$ creation-annihilation operator pairs and corresponding coupling strengths $\Delta_{d_i d_j}$ and $\Delta_{d_i c}$, while N specifies the number of metallic particles and $d^\dagger$ and $c^\dagger$(d and c) are the creation(annihilation) operators for the nanoparticle plasmon and emitter.

In our case, the hexagonal array consists of a certain density of nanorods: Within the coherence length ($\approx$ 320 nm) of collective L-modes, approximately two shells of nearest neighbor Au nanorods have to be considered. Even if we consider only the first shell of one rod, 7 nanorods are involved in the hamiltonian. So, 28 distance dependent coupling strengths ($\Delta_{d_i d_j}$ and $\Delta_{d_i c}$) are for instance involved in the H_{int} term in the Hamiltonian. Furthermore, considering itinerant surface plasmons and long-distance interactions, an exact diagonalization of this many-body system is not possible up to now. Therefore, an approximation should be applied.

Here, we introduce a quasi-particle approach, treating the collective L-mode as emergent from a single quasi-particle instead of calculating a representational N-particle model. In other words, a collective mode will be quantized as a boson, then this boson is applied in Manjavacas's one emitter/one particle model. [86]. The basic idea of this approximation is sketched in Fig. 5.3. Thereby, our model simplifies from a system with a large number of plasmons (corresponding to a large number of metallic nanoparticles) and one molecular exciton to a system which consists of one single boson ($N = 1$) and one exciton. The N-particle problem, therefore, can be transfered to a problem of interaction between two single particles.

Based on the one emitter/one particle model from Ref. [86] and the quasi-particle approximation, the optical absorption spectrum of the plexciton system in the array, is then given by

$$\sigma(\omega) \propto -\mathrm{Im}\left\{\left[\hbar\omega - \epsilon_p + \delta\omega_p + i\frac{\Gamma_p}{2} - \frac{\Delta_{pe}^2(1-2n_e)}{\hbar\omega - \epsilon_e + (1-2n_e)\left(\delta\omega_e + i\frac{\Gamma_e}{2}\right)}\right]^{-1}\right\}. \tag{5.1}$$

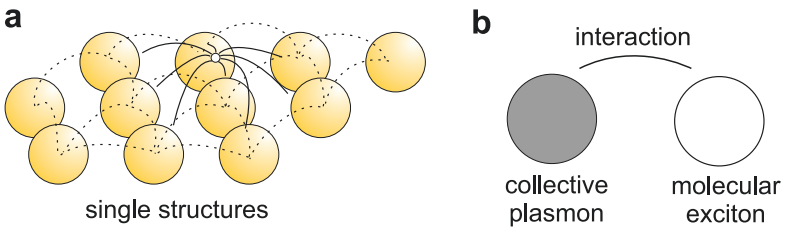

Fig. 5.3: a) A scheme of the quasi-particle approach with a large number of nanoparticles in an array. Long-distance interactions and varying coupling strengths have to be considered. b) The collective surface plasmon is replaced by a boson. [36] Reprinted with permission.

Tab. 5.1: Model parameters derived from a fitting.

Model parameters	
ϵ_e	1.933 eV
ϵ_p	2.032 eV
$\delta\omega_e$	0.05665 eV
$\delta\omega_p$	0.02107 eV
Δ_{pe}	0.1475 eV
Γ_e	0.3805 eV
Γ_p	0.246 eV
n_e	0.03958

Here, $\hbar\omega$ is the energy of one incident photon; ϵ_p and ϵ_e represent the energies of surface plasmons in the Au nanowire array and the molecular exciton, respectively; $\delta\omega_p$ and $\delta\omega_e$ denote energy shifts; Γ_p and Γ_e are the inelastic decay rates of the plasmon and exciton, respectively; Δ_{pe} is the plasmon-exciton coupling strength; n_e is the expectation value of initial occupation of the excited state of the exciton.

We note that $\epsilon_p - \delta\omega_p$ in Equation 5.1 (as well as $\epsilon_e - \delta\omega_e$, when n_e is much smaller than 1), can be treated as one term and represents a shifted energy level.

In Fig. 5.4(a) the experimental collective L-mode data as a function of energy are shown as black dots. Normalized data are converted from the blue curve in Fig. 5.2(a), and the T-mode contribution is removed. The data were analyzed using the single quasiparticle model according to Equation 5.1. In Table 5.1 the evaluated model parameters are shown.

The modeled spectrum exhibits a distinct mode splitting in accordance with the observation with the coupling constant (half of the peak splitting) being $\Delta_{pe} \approx 147.5$ meV. This value is reasonable, if compared with the re-

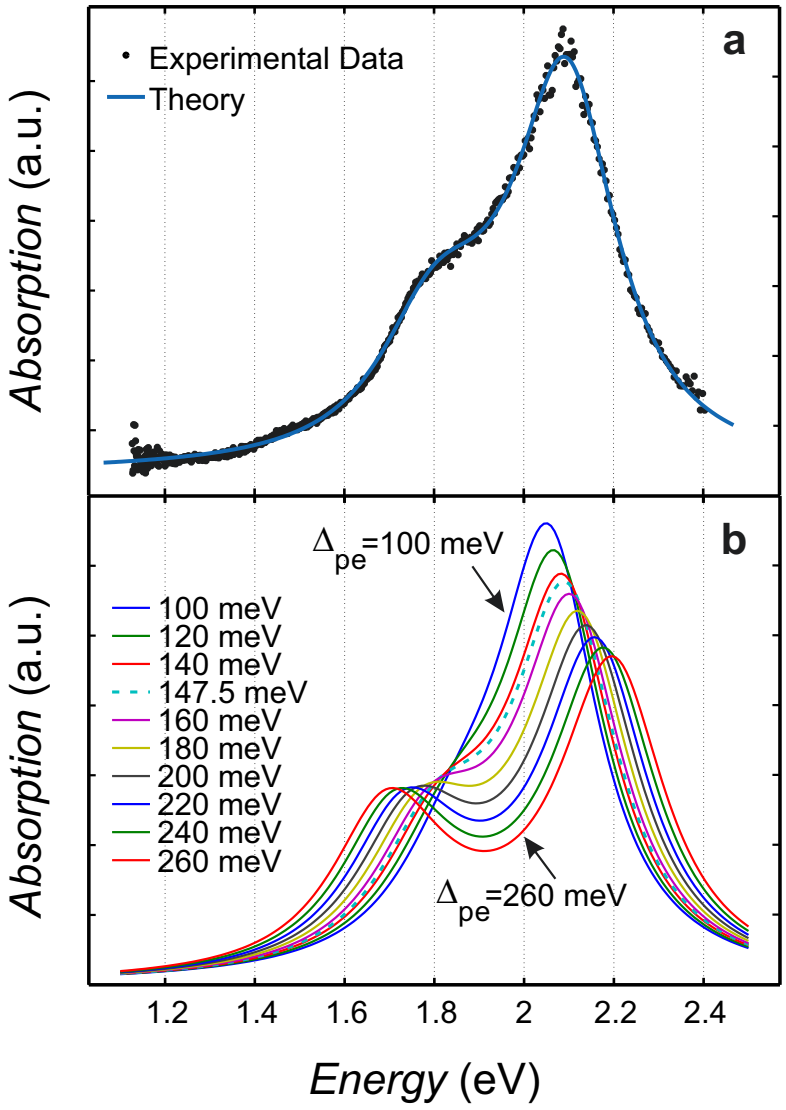

Fig. 5.4: a) Experimental collective L-mode data as function of energy fitted by the described quasiparticle model. The parameters evaluated by fitting are shown in Table 5.1. b) Variation of coupling constant to visualize the resulting coupling effect. The T-modes have been removed from the spectra. [36] Reprinted with permission.

ported value of the coupling constant of ∼140 meV between plasmons of single Ag nanoparticles and molecular excitons in porphyrin dyes DTBC. [106] Besides, the values of inelastic decay rate of the hybrid plasmon branch and exciton branch ω_p, 0.246 eV and ω_e, 0.3805 eV, are also in accordance with the measurement results shown in Fig. 5.2(a).

In Fig. 5.4(b), we show the pronounced effect of the coupling constant Δ_{pe} on the line shape of the absorption. For this a series of normalized data with varying Δ_{pe} are calculated. As shown, for $\Delta_{pe} = 260$ meV, the dip is deep and the separation between the two resulting maxima is obvious. For decreasing Δ_{pe}, the dip becomes more shallow and at $\Delta_{pe} = 100$ meV it almost disappears. Comparing with the upper experimental spectrum, the quality of the data representation using the quasiparticle model is very satisfying.

5.4 Conclusion

As summary, a collective surface plasmon mode with a quasi linear dispersion behavior has been achieved in Au nanorod arrays. Based on that the experiments of strong coupling between the surface plasmon and molecular excitons have been carried out and the coupling is fine-tuned via changing the angle of incidence. A quasi-particle model, which extends the applicability of the Zubarevs Green function method to a many-particle system, has been introduced to theoretically describe the interaction between collective plasmons and excitons in the array system. Such a subwavelength optical system, which has properties such as linear dispersion of waveguide and at room temperature switchable hybrid states, could be a promising candidate to achieve optical transistor for integrated optical circuit.

6. APPLICATION: SURFACE ENHANCED RAMAN SCATTERING

Detecting and quantifying target analytes with high specificity and sensitivity is of fundamental importance to analytical science and technology. In this chapter, *Surface-enhanced Raman scattering* (SERS) and *Isotope dilution surface-enhanced Raman scattering* (IDSERS) will be discussed. The former is a qualitative technique while the latter can be carried out as a quantitative tool.

6.1 SERS

SERS is a rapid and cost-efficient universal method for detecting analytes. By adsorbing molecules on rough metal surfaces or nanostructures Raman scattering signal can be enhanced with a factor as much as millions. It allows to measure samples with insignificant quantity, and measure faster or with smaller laser power.

After 40 years development and with more than 15.000 publications, the SERS technique has become a powerful application. However, the mechanisms contributing to the enhancement effect are still poorly understood. This is owed to the fact that SERS is a complex light-matter interaction process, which involves usually radiative and non-radiative electron transfer, virtual photon transfer, mesoscopic physics of the nano-particles (especially on surface/interface), charge transfer resonance between nanoparticles and molecules, the chemical change of the molecules, and environmental influences. Therefore, a classical electromagnetic model is insufficient for a full description. Several essential questions are still poorly understood and limit a further fundamental development of this technique.[107, 108]

In this section, SERS experiments on different organic molecules will be discussed in order to demonstrate that a nanorod array is a suitable platform for the theoretical treatment of SERS-related phenomena.

6.1.1 Introduction

Surface plasmons are of great interest for potential applications since they emerge from sub-wavelength structures. For instance, surface plasmonic waveguides are highly compact and exhibit a transverse mode confinement below the diffraction limit. The surface plasmonic sub-wavelength apertures present extraordinary transmission characters, and are applied in optical switching. [109]

Another spectacular application is surface-enhanced Raman scattering. As described in the section 2.2.3 the Raman effect (in the context of molecules) describes the inelastic scattering process between a photon and a molecule, due to a fundamental vibrational or rotational modes of the latter. SERS utilizes a highly localized electromagnetic field close to the metallic nanostructures to enhance the spontaneous Raman scattering of individual molecules. In 1974, Martin Fleischmann and his colleagues observed the first SERS spectrum. In 1977 Jeanmaire and Van Duyne showed the most representative features of SERS: An enhancement of the Raman cross-section per molecule by a factor of a million. Although 40 years have passed since SERS effect was first discovered, its theory remains incomplete to explain the enhancement of the Raman cross-section. The current understanding of signal enhancement in SERS is that there are two separate mechanisms responsible for the enhancement of Raman scattering, the electromagnetic mechanism (EM) and the chemical mechanism (CM), respectively.

The EM is based on the enhancement of the local electromagnetic field around the metallic nanostructured surface due to surface plasmons, resulting in the enhancement of the light excitation. In fact, after the first demonstration of SERS on the roughened surface of metal, a large number of studies have been carried out optimizing the surface using metal colloids or dispersed metal nanoparticles. The spatial extent of the enhanced local electromagnetic field is usually in the range of several tens of nanometers. If two or more metal nanoparticles on the surface are sufficiently close, the enhanced light fields associated with them may overlap and interact, resulting in a significant increase in the intensity of the electromagnetic field between the nano units. These spots between the metal surfaces are often referred to as hot spots, and if the sample molecules migrate to such hot spots, the Raman signal can be enhanced to allow even single molecule detection through SERS.

The CM have been proposed as a supplementary contributor (or as an alternative explanation) to the plasmonic theory. Such CM effects are related to specific interactions between the molecule and the surface, where transfer and exchange or sharing of charges between molecule and substrate

are considered as most likely basic process. In detail, CM effects could be classified in the following categories: (1) metalligand complex formation, (2) the creation of new metal-to-molecule or molecule-to-metal charge transfer resonances, or (3) the transient residence of hot electrons or electron hole pairs out of the metal on the ad-molecule. [107]

Moreover, other physical or chemical effects are also involved in the SERS measurements, for instance quenching and enhancement of fluorescence, luminescence of metallic nanostructures, nonlinear processes such as light-induced degradation of molecules, etc. Those further complicate the analysis of SERS measurements. In this chapter experimental details which influence the SERS spectra will be discussed in order to clarify the physicochemical processes of SERS. Furthermore, isotope-dilution SERS will be studied with respect to metrological applications.

In most cases SERS is attributed to a strong amplification of the electromagnetic fields near the plasmon resonances of metallic nanostructures. From the point of view of SERS substrate fabrication, two main routes for SERS detection can be categorized: the first one uses nanoparticles assembled as a SERS substrate. For this, the nanoparticles are usually synthesized with wet chemical methods first, followed by a size-selecting procedure (optional) and aggregation. The second approach is using pre-formed SERS substrates. For this usually a spontaneous formation process of nanostructures on the SERS substrate is employed, and the resulting nanopattern can only be influenced to a certain degree. Methods include templating, sputtering, photo or electron beam lithography. From the point of view of state of SERS substrate during measurements, there are three different categories (here taking nanoparticles assembled SERS subtrates as an example): 1. solution-based direct-readout SERS detection, called *wet state method*; 2. colloidal nanoparticles to form thin solid films for SERS detection, called *dry state method*; 3. SERS detection based on a transition from the wet state to the dry state, sometimes referred to as *state translation nanoparticle-enhanced Raman spectroscopy* [110]

We classify SERS substrates into two types: type I allows for target molecules to move around in the light field (*motion structures*), while type II spatially confines molecules (*motionless structures*). In a motion structure (for instance metallic colloids), target molecules can spontaneously move in and out of the focusing area of the excitation laser or the light field around the target molecules can spontaneously fluctuate. In this case, the Raman signal contains an averaged contribution of all molecules probed during the measurement time. As shown in Fig. 6.1 a, at moment 1, two molecules (red dots) located in the focal spot of the excitation light are measured. At moment 2, one of them exits the focal area together with its connected

nanoparticle No. 4, e.g., due to *Brownian motion*. Now a third molecule enters the newly formed hot-spot between nanoparticle No. 1 and No. 3. In addition, one molecule which is connected with particle No. 5, enters the focusing area. Overall, such processes can lead to both increase and decrease of Raman signals.

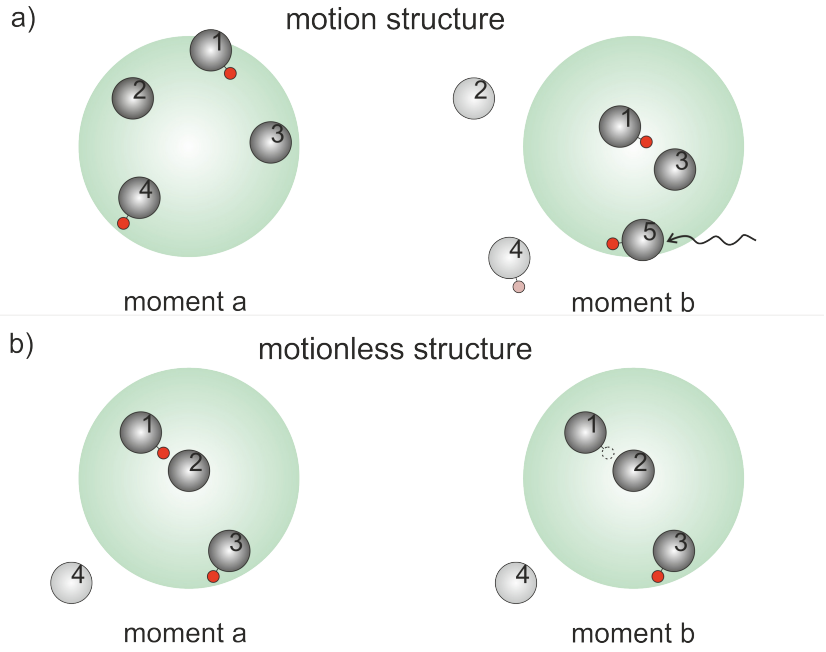

Fig. 6.1: Motion and motionless structures of a SERS measurement. Target molecules are shown as red dots. Nanoparticles are metallic circles with numbers in the figure and a green circle is the focusing area of the excitation laser.

In contrast, in a confining, motionless structure (e.g., dried metallic colloids) no molecules are able to go in or out of the focusing area and the local light field will not change, if we assume that the excitation light is stable. As shown in Fig. 6.1 b, only a photochemical reaction (degradation) could influence the total number of molecules, which are located in the focusing area. An overall decrease of Raman intensity would be possible only due to a decreasing number of molecules.

The differences between motion and motionless structures highlight the role of statistics on the SERS signal intensity. In this section, Au nanorod arrays were used as motionless structured SERS substrates. We will first consider the degradation related Raman signal loss in such a motionless structure. Other effects will be discussed in the following sections.

Regarding degradation processes within motionless structures, we assume

that the possibility of degradation of one molecule in a stable light field is b. Hence, b should be function of intensity of excitation light $b(\Pi)$, where Π is the excitation light. Therefore, we get the SERS intensity expression as function of time t.

$$I = ae^{-bt}, \tag{6.1}$$

where a consists of all the physical process parameters/influences (including the setup responding function) in the SERS measurement. We define the starting time of the measurement as $\tau_0 = 0$, therefore we have $I_0 = ae^{-b\tau_0} = a$. Regarding Raman measurements in which the signal is collected during a time period from τ to τ', the measured value (mean value) can be expressed as an integration:

$$\begin{aligned}
\bar{I}_{\tau\to\tau'} =& \frac{1}{\tau'-\tau}\int_{\tau}^{\tau'} ae^{-bt}dt \\
=& \frac{a}{-b(\tau'-\tau)}\, e^{-bt}\Big|_{\tau}^{\tau'} \\
=& \frac{a}{-b(\tau'-\tau)}(e^{-b\tau'} - e^{-b\tau}),
\end{aligned} \tag{6.2}$$

Therefore, we can assume that the start and end points of the n-th measurement are τ_n and τ_{n+1}, respectively, and a constant accumulation time between any pair of start and end points is $\Delta\tau$. Therefore, for the intensity of the n-th measurement $\iota(n)$, we define $\iota(n) = \bar{I}(\tau_n) = \bar{I}_{\tau_{n-1}\to\tau_n}$. The overall Raman intensity is then according to equation 6.2,

$$\begin{aligned}
\iota(n) =& \bar{I}(\tau_n) \\
=& \frac{a}{-b(\tau_n - \tau_{n-1})}(e^{-b\tau_n} - e^{-b\tau_{n-1}}) \\
=& \frac{a}{-b\Delta\tau}(e^{-b\tau_n} - e^{-b(\tau_n-\Delta\tau)}) \\
=& \frac{a}{-b\Delta\tau}(1 - e^{b\Delta\tau})e^{-b\tau_n} \\
=& \frac{a}{-b\Delta\tau}(1 - e^{b\Delta\tau})e^{(-b\Delta\tau)n} \\
=& a'e^{-b'n},
\end{aligned} \tag{6.3}$$

where $a' = \frac{a}{-b\Delta\tau}(1 - e^{b\Delta\tau})$ and $b' = b\Delta\tau$.

As shown in equation 6.3, the intensity $\iota(n)$ is still a first order exponential decay function of order n, and only the corresponding indexes are modified.

More generally, for a higher order exponential decay function $I = \sum_i a_i e^{-b_i t}$, a corresponding $\iota(n)$ holds

$$\begin{aligned}\iota(n) =& \frac{1}{\Delta\tau}\sum_i \frac{a_i}{-b_i}(1-e^{b_i\Delta\tau})e^{(-b_i\Delta\tau)n} \\ =& \sum_i a_i'' e^{-b_i'' n},\end{aligned} \tag{6.4}$$

for a multi-window measurement (covering a larger energy-range composed of N individual spectra). In addition we have to consider here the m-th window in one spectrum. Therefore, we have $n' = (n-1)N + m$

$$\begin{aligned}\iota_{N,m}(n) =& \bar{I}(\tau_{n'}) \\ =& \frac{a}{-b\Delta\tau}(1-e^{b\Delta\tau})e^{(-b\Delta\tau)n'} \\ =& \frac{a}{-b\Delta\tau}(1-e^{b\Delta\tau})e^{(-b\Delta\tau)((n-1)N+m)} \\ =& [\frac{a}{-b\Delta\tau}(1-e^{b\Delta\tau})e^{b(N-m)\Delta\tau}]e^{[-bN\Delta\tau]n} \\ =& Ae^{-Bn},\end{aligned} \tag{6.5}$$

where both A and B are not n dependent. Similarly, for a higher order exponential decay,

$$\begin{aligned}\iota_{N,m}(n) =& \sum_i [\frac{a_i}{-b_i\Delta\tau}(1-e^{b_i\Delta\tau})e^{b_i(N-m)\Delta\tau}]e^{[-b_i N\Delta\tau]n} \\ =& \sum_i A_i' e^{-B_i' n},\end{aligned} \tag{6.6}$$

6.1.2 Experiment and Characterization

A LabRam HR 800 Raman microscope (Jobin/Yvon HR 800) with a 532 nm excitation laser (Setup 1) and a similar setup from Renishaw (Setup 2) at the PTB (Physikalisch-Technische Bundesanstalt), Abt. 3.14 (within Dr. R. Stosch's group) were used to perform the SERS experiments in this section. Target molecules were dissolved in ethanol with different concentrations and dropped on the surface of AAO/Au nanorod arrays substrates, which have been described in section 4.1, as motionless substrates. All measurements were carried out at room temperature.

SERS measurements on dye molecule *Rhodamine 6G* ($C_{28}H_{31}N_2O_3Cl$), which is usually discussed in literature as a standardized probe-molecule were carried out by using Setup 2 for verification of the enhancement ability of the AAO/Au nanorod array substrates.

Rhodamine 6G is a highly fluorescent rhodamine family dye. It is extensively used as a tracer dye in fluorescence microscopy or a laser dye due to its intensive fluorescence, which can be easily pumped and detected. Using a 532 nm excitation energy from a Nd:YAG laser or nitrogen laser, rhodamine 6G is easily pumped and has high fluorescence quantum yield and a remarkably high photostability.[111, 112, 113] As shown in Fig. 6.2, the absorption and emission spectra of Rhodamine 6G contain features at 538 nm and 585 nm (corresponding to the energy range 200 cm^{-1} to 1700 cm^{-1} when using a 532 nm laser as excitation), the fluorescence covers the full measurement range of Raman spectra shown in Fig. 6.3. Without a SERS effect/fluorescence quenching, the Raman signal would be submerged in the fluctuation of fluorescence.

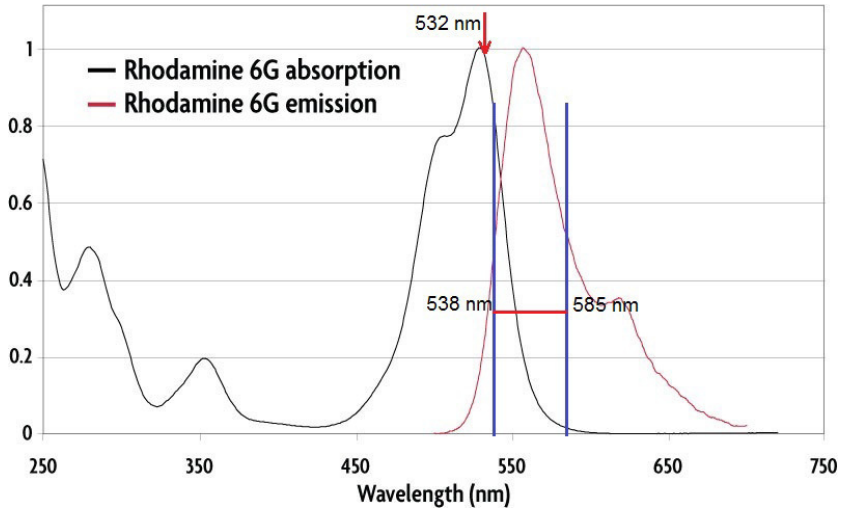

Fig. 6.2: Absorption and emission spectra of Rhodamine 6G in ethanol. With a 532 nm laser excitation, the lines at 538 nm and 585 nm corresponds to 200 cm^{-1} and 1700 cm^{-1} in Raman spectra, respectively. Without quenching effects, fluorescence should be proposed to cover the full measurement range between 200 cm^{-1} and 1700 cm^{-1} in Raman spectra.

In the SERS experiment, rhodamine 6G dye molecules (Sigma-Aldrich) were diluted with ethanol to achieve a relative low concentration at 10^{-6} mol/L. 5 μL rhodamine 6G solution was dropped on the surface of the AAO/Au nanorods substrate, dried and measured with the same parameters except the grating and filter. As shown in Fig. 6.3, the identical sample was measured with gratings of 1200 lines and 1800 lines, respectively. Regarding the sharp characteristic peaks, it is clear that the broad fluorescence of R6G was quenched and the Raman signal was enhanced.

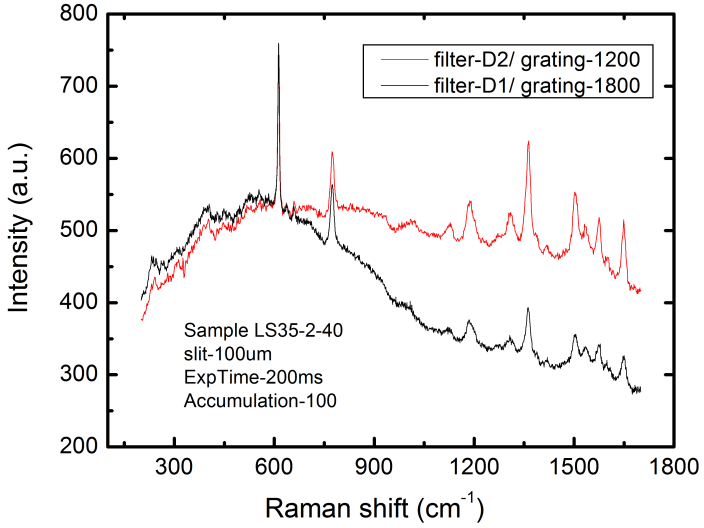

Fig. 6.3: SERS spectra of Rhodamine 6G(R6G). Setup parameters and fluctuation of size of nanounits influence the spectra.

For further confirmation and comparison of results, the molecules *Malachite Green*, (*4-[4-(Dimethylamino)phenyl](phenyl)methylidene-N,N-di -methylcyclohexa-2,5-dien-1-iminium chloride*, $C_{23}H_{25}ClN_2$ (chloride)) were also measured as a target. As shown in Fig. 6.4, the black curve is the Raman spectrum from compressed malachite green power, which was measured in air with the following parameters using setup 1: 532 nm laser, 150 μm pin hole, D3 filter, x50 magnification, 20 second acquisition time, and 10 times accumulation. 7 maxima around 1295 cm^{-1}, 1340 cm^{-1}, 1368 cm^{-1}, 1400 cm^{-1}, 1485 cm^{-1}, 1590 cm^{-1} and 1620 cm^{-1} could be detected as characteristic peaks in this spectrum. Next, the powder of malachite green molecules was dissolved in ethanol with a concentration of 10^{-4} mol/L. By using a micropipette 5 μL of malachite green solution was dropped onto the surface of a AAO/Au nanorod array substrate and onto the surface of a silicon wafer, respectively. Both samples were dried in air for more than 24 h, and then measured in air under the same conditions with Setup 1: 532nm laser, 150 μm pin hole, D2 filter, x50 magnification, 10 second acquisition time, and 10 times accumulation. The Raman spectrum obtained on the AAO/Au nanorod array substrate is shown as the red curve, in which most of the 7 characteristic peaks are well resolved. On the other hand, the spectrum from malachite green molecules deposited on the silicon wafer (green curve) only a single feature can be confidently distinguished from the background

and noise (the most intensive peak around 1620 cm^{-1}). The Raman signal enhancement emerging from the AAO/Au nanorod array is immediately evident. More details will be discussed in the next section.

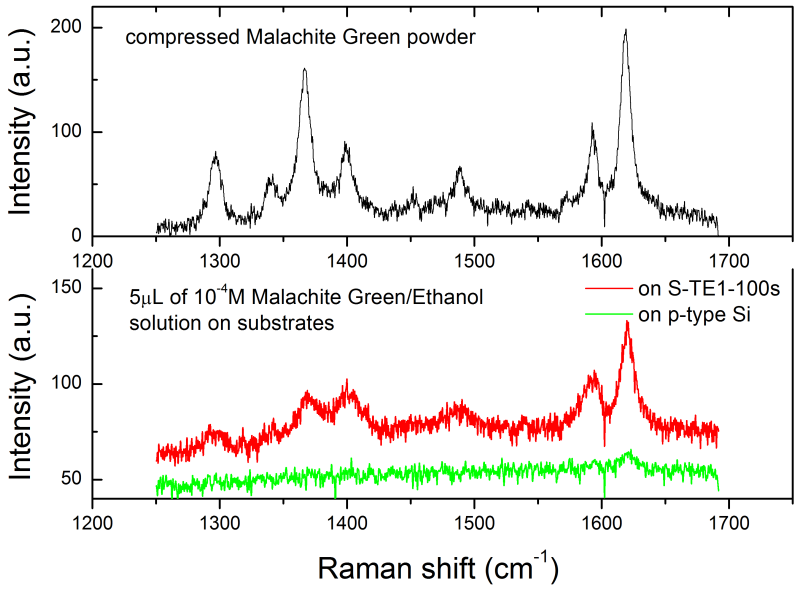

Fig. 6.4: Raman spectrum of macroscopic malachite green powder(black curve), spectrum of low concentrated Malachite Green on a SERS substrate(red curve) and on a silicon wafer(green curve).

Besides those static characterization experiments, time-dependent intensity measurements were additionally carried out, to shed light onto additional "dynamic" processes of such complicated light-matter interactions. Target molecules on AAO/Au substrates were measured via Setup 1. As motionless systems, these allow for a more precise characterization of the "dynamic" process, because the effects from a varying number of target molecules as sketched in Fig. 6.1 a) can be avoided in these experiments.

10^{-3} mol/L Malachite Green in ethanol was dropped onto an AAO/Au substrate and dried in air. A constant laser beam with a power-level of around 32.7 μW was focused onto the surface during the whole series of measurements, and the focal spot was not moved. Eight spectra are presented in Fig. 6.5. For each spectrum 10 s acquisition time and 10 accumulations were applied. After the acquisition the laser would be immediately blocked by switching a mirror in the optical-path, and it would only be re-directed onto the sample at the start of the next measurement. We estimate that

a maximal variation in illumination time of 2 – 3 seconds may occur on an overall acquisition time of 10 × 10 s. As shown in Fig. 6.5, there is a clear decay of the absolute intensity of observed modes. More details will be discussed in the next section.

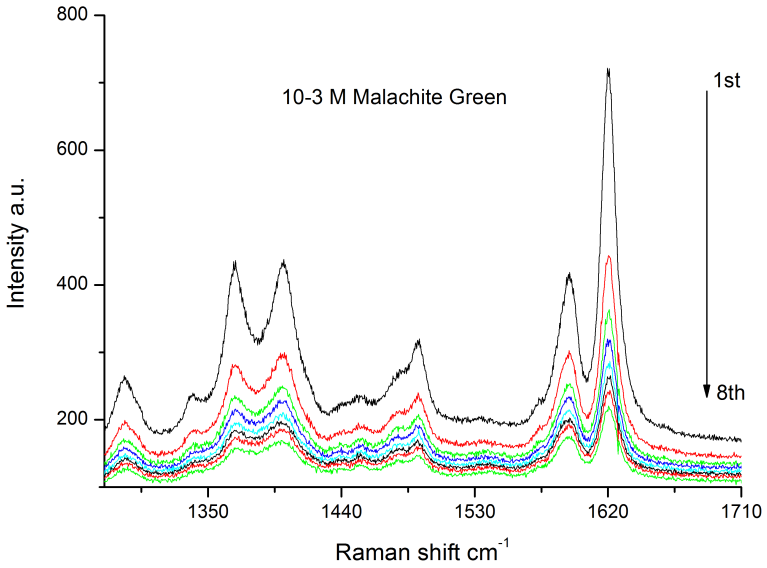

Fig. 6.5: A series of SERS spectra of malachite green. Light-induced degradation leads to a decay of Raman intensity.

6.1.3 Results and Discussion

Characteristic peaks from both Raman spectra in Fig. 6.3 are fitted with Lorentz line-shapes. All 6 modes, which have relative high intensities, are presented in Table 6.1. Regarding the intensity ratios, a mode dependence rather than a constant factor can be clearly found.

As shown in Fig. 6.6, the intensity ratio between Raman modes in table 6.1 are plotted as a function of wavenumber. In this work, we attribute such deviations from a constant ratio to different response functions of gratings (setup) or different frequency-dependent light scattering probabilities by nanoparticles (plasmon resonance dispersions), because the ratio shows a clear tendency instead of a random behavior, and the intensity of the background in the higher energy regime follows this tendency as well. This can be taken as evidence that electromagnetic enhancement/response is different for every Raman mode.

peak (cm^{-1})	intensity (grating 1800)	intensity (grating 1200)	ratio
612.8	239.4	223.8	1.06971
774.1	85.6	87.8	0.97494
1188.1	32.5	58.7	0.55366
1362.2	70.4	151	0.46623
1502.9	47.5	96.5	0.49223
1648.5	41.9	85.5	0.49006

Tab. 6.1: Mode intensities fitted from the spectra in Fig. 6.3.

An instrument calibration could minimize the influence from a nonlinear response function of the setup. In principle, a quantification of the "original" absolute intensity of Raman modes (without a drift by plasmon resonance dispersions) or the "original" intensity ratios among Raman modes is based on a good understanding of surface plasmons in the system. For visually explaining this point, one SERS measurement comparison will be discussed as an example as follows: In Fig. 6.7, two SERS measurements on Rhodamine 6G were performed on an identical AAO/Au substrate. All conditions of the measurements are the same, except for the focal area of the excitation laser on the substrate. The two measurement spots are separated by dozens of micrometers.

Comparing the background signals obtained at spot 1 and spot 2 (Fig. 6.7) we see an increase in intensity in the lower energy range, and simultaneously a decrease in intensity towards higher energies. The cross-over point is located around 1000 cm^{-1} (dashed line). This difference in background intensity is solely position dependent. All Raman modes marked with arrows in each spectrum are normalized in intensity by the 612.81 cm^{-1} mode, which is marked with a blue circle. The normalized intensities (or rather, intensity ratios) of the 5 marked Raman modes are plotted in Fig.6.8. In this figure, the absolute intensity of a mode was obtained after subtracting the fitted SERS background, $I_{sers} = I_{spectrum} - B_{background}$. As shown, for spot 2 normalized modes above 1000 cm^{-1} are enhanced and the normalized intensity of modes below 1000 cm^{-1} are decreased. Thus the signal intensity evidences the same variation as the background.

In a SERS experiment – especially when using motionless structures or on-chip SERS experiments – such position-dependent intensity variations are frequently observed. From a chemical point of view this is unexpected, as the chemical properties and adsorption should be spatially homogeneous. Therefore, it is expected that the surface plasmon would not only enhance the SERS mode homogeneously in a certain energy region, but also lead to

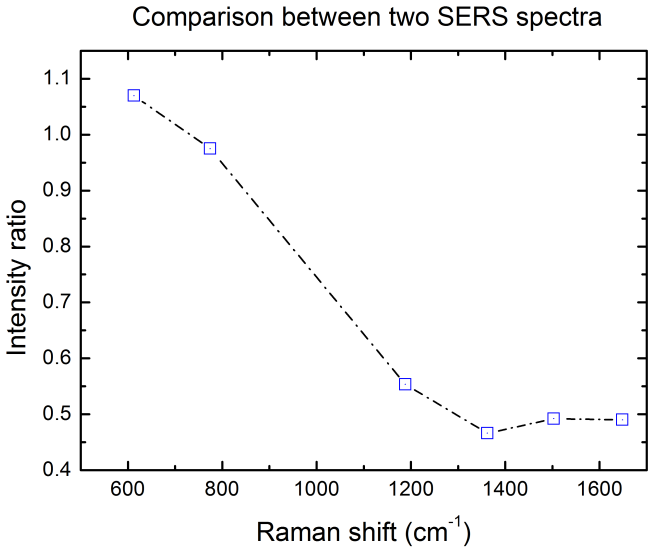

Fig. 6.6: Comparison of mode intensity in two rhodamine 6G SERS spectra in Fig. 6.3. Each mode gains its own intensity ratio. However, the change of the ratio from low-energy mode to high energy mode has a smooth transition.

a drift of relative intensities. Such a drift was reported by Itoh, et al. [114] in 2007. This effect was named "second enhancement" and attributed to resonance Raman processes. Lin et. al. reported such a drift as *plasmonic spectral shaping effect* (PSSE) in 2017, and proposed that this phenomenon originates from the LSPR-modulated photoluminescence of metallic nanostructures. [115]

Comparing the evaluation procedure corresponding to Fig. 6.8, a correction $I_{sers} = (I_{spectrum} - B_{background})/B_{background}$ is proposed here, and the results are plotted in Fig. 6.9. As shown in the figure, two spectra coincide much better, and the splitting tendency in the higher energy region is suppressed.

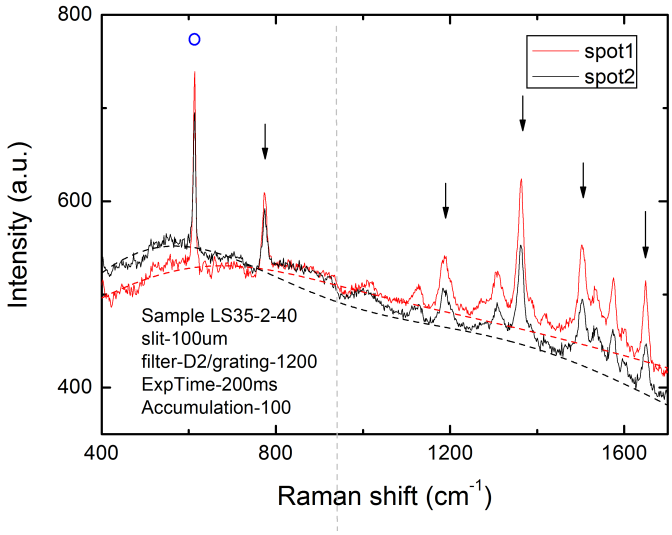

Fig. 6.7: Two SERS spectra from two spots on identical Au/AAO SERS substrate.

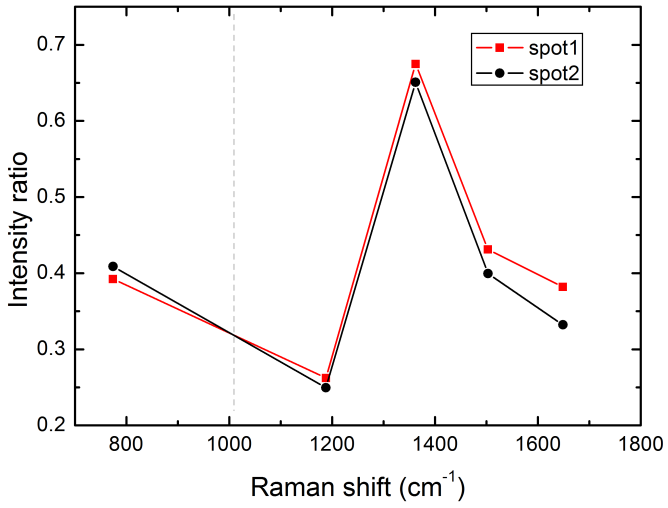

Fig. 6.8: A direct comparison between normalized intensities of Raman modes in two spectra in Fig. 6.7. A gap shows clearly in the high energy range.

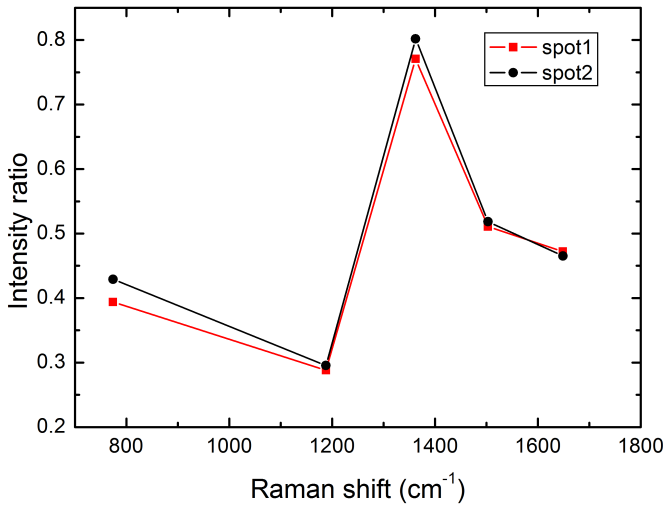

Fig. 6.9: Comparison between normalized intensities with a correction. in contrast to Fig. 6.8, the gap in the high energy range disappears here.

In order to discuss the relative intensities related to chemical properties, on-chip SERS experiments on malachite green molecules were also carried out. Raman spectra in Fig. 6.4 from malachite green power and SERS were fitted by Lorentz line-shapes. The intensities of all 7 noticed characteristic peaks are presented in Table 6.2. It should be noted that the characteristic peaks gain a varying enhancement ratio instead of a constant factor. This is related to a selective enhancement in such a SERS process.

peak (cm^{-1})	powder intensity	SERS intensity	ratio
1295	78.4±4	10.8±1.3	7.26±1.24
1340	40.7±3.3	6.6±1.7	6.17±2.09
1368	**145.6±5.1**	**24.5±1.2**	**5.94±0.50**
1400	**74.3±4.6**	**30.7±1.3**	**2.42±0.25**
1485	52.2±3.1	25.8±4.4	2.02±0.47
1590	84.3±4.9	34.2±1.5	2.46±0.25
1620	189.1±8.9	61.9±1.7	3.05±0.23

Tab. 6.2: Mode intensities fitted out from Malachite Green SERS spectra in Fig. 6.4.

The fitting results are plotted in Fig. 6.10, where each symbol corresponds to one characteristic peak. Two neighboring symbols (3^{rd} and 4^{th})

are highlighted here: the characteristic peaks at 1368 cm^{-1} (573.76 nm) and at 1400 cm^{-1} (574.81 nm). A dramatic drop as observed here within an energy range of about 1 nm can not be explained simply by considering the wavelength-dependent response function of our setup, and it would also not be accounted for by a classical electromagnetic model, which excludes all microscopic states of molecules and surface plasmons.

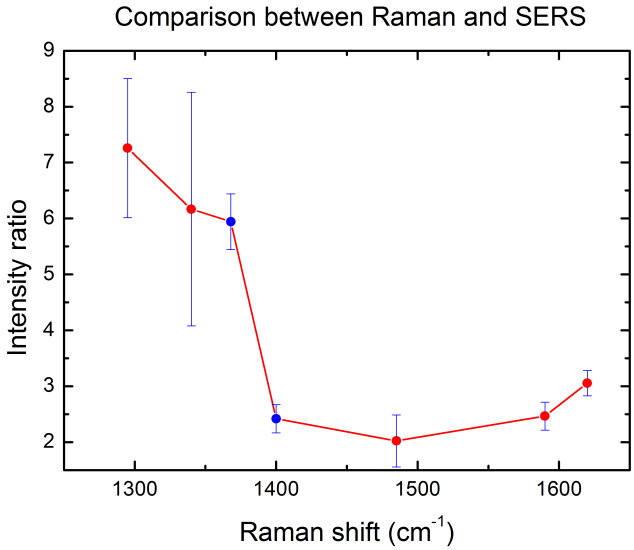

Fig. 6.10: Intensity ratio of characteristic modes of Malachite Green in Tab. 6.2. A mode-selective behaviour shows up in this case.

The intensity ratio between these two characteristic peaks in each spectrum also changes in the SERS process. For the powder malachite green sample, the ratio, defined by I_{1368}/I_{1400} is 1.96, while in the SERS spectrum it is 0.80. A selective enhancement factor for each Raman mode indicates that not only an enhancement of near-fields around the Au nano-structure affects the SERS, but also other chemical bands or electron-related interactions are of importance. Such a mode-selective enhancement behavior is strongly dependent on the SERS substrate. This can also be seen by comparing the Rhodamine 6G Raman spectra from literature. [116, 117, 118, 119] Two SERS spectra of Rhodamine 6G on similar plasmonic structures (AAO-$CuCl_2$-Au multilayer substrate [116] and Au nanowires array [117], respectively) from literature are compared in Fig. 6.11 and 6.12 as follows:

The intensity of the Raman mode at 1313 cm^{-1} is of strong intensity in Fig. 6.11, and nearly the same as mode at 1505 cm^{-1}, while in Fig. 6.12, the intensity of the Raman mode at 1313 cm^{-1} almost vanishes. In fact, a closer

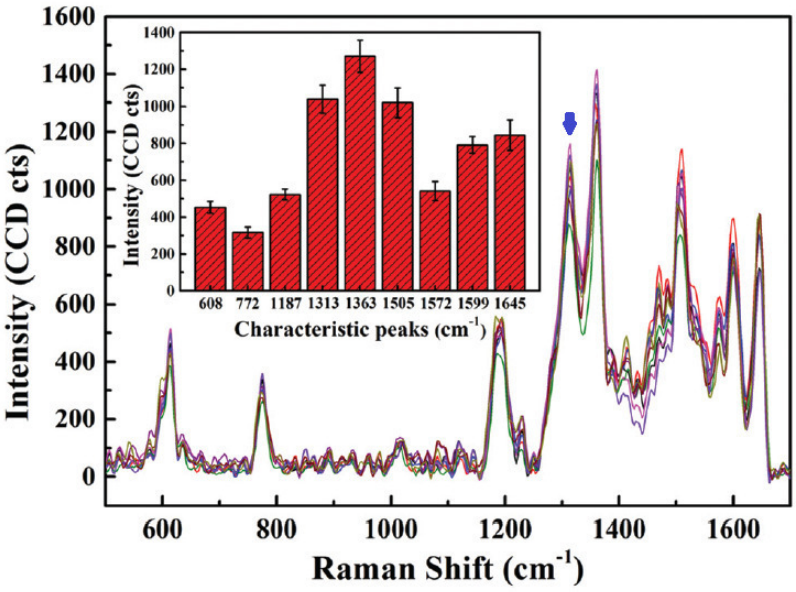

Fig. 6.11: Rhodamine 6G SERS spectra from reference [116] The Raman mode at 1313 cm^{-1} (blue arrow) is intensive. Figure adapted with permission from Royal Society of Chemistry.

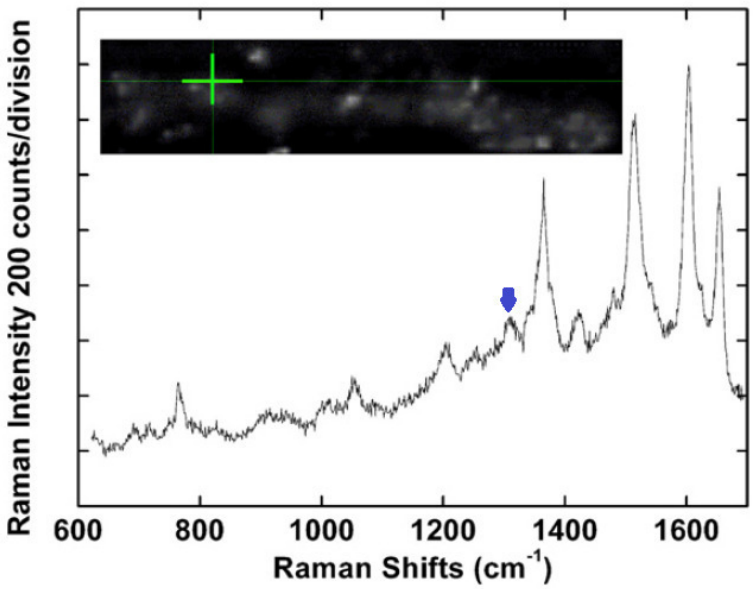

Fig. 6.12: Rhodamine 6G SERS spectra from reference [117] The mode at 1313 cm^{-1} vanishes, comparing to the spectrum in Fig. 6.11. Figure adapted with permission from IOP Publishing.

look reveals that almost every intensity ratio between modes is modified if we compare Fig. 6.11 and 6.12.

Several mechanisms and hypotheses have been proposed to explain such a mode-selective enhancement behavior in SERS, for instance *chemical enhancement mechanisms* and *transient charge transfer (TCT)* by Otto. Within the chemical enhancement mechanisms the following processes are considered: a metal-ligand complex formation or the creation of charge transfer resonance between molecule and metal, or the transient residence of hot electrons out of the metal on the ad-molecule. [107] Campion and Kambhampati measured the electronic absorption spectrum of *Pyromellitic dianhydride* (PMDA) on a Cu(111) surface using *Electron energy loss spectroscopy* (EELS) to see if any new electronic excitations resulted from chemisorption, and they demonstrated that a new low-energy electronically excited state is created when PMDA is adsorbed on copper. They attributed the mode-selective enhancement to new excited states from the chemisorption, and found that the bonding configurations on each surface could be different and the combined effects of the anisotropic molecular polarizability and surface screening would produce different spectra. [120] Zayak, et al., used first-principles DFT calculations and experimental data to explain chemical contributions to SERS for *benzene thiol* (C_6H_5SH) molecules chemisorbed onto Au atoms, which were located on (infinite) Au (111) surfaces. They calculated static contributions to the Raman tensor, and elucidated the vibrational mode dependence. [121] A comparison between the calculated relative enhancements and experimental relative enhancements was achieved by assuming that during a SERS measurement the absolute CMs can be obtained if 1. all modes normalize to a mode with zero deformation potential, which will not be affected by CMs at all, and 2. the electromagnetic enhancement is the same for all modes. With these assumptions the relative enhancement will reflect the importance of CMs. There are several limits to such approximations: 1. a mode with zero deformation potential must exist within the target molecule. This mode has to be calculated first as an experimental identification is problematic, because EM and CM always appear simultaneously for candidate molecules of CMs. 2. In a more general case, the electromagnetic enhancement is not the same for all vibrational modes, and a plasmon resonance dispersion correction needs to be applied. In addition, as the discussion based on Fig. 6.3 shows, different experimental setups lead to different response functions, specific characteristics of experimental setups must be taken into account. In a review article from Jensen, et al., they summarized all CMs with electronic structure effects as shown in Fig. 6.13. [122] They label different enhancement mechanisms as *CHEM*, *resonance*, *CT* and *EM*, respectively, and count the a), b) and c) contribu-

tions as CM(or a) and c), depending on the definition of a CM), and the rest is the EM. Although all effects are often grouped together, a separate treatment is of importance for an in-depth understanding. It should be noted that all these electronic structure CMs correspond to different Raman excitation wavelengths. It is very difficult to establish experimentally since only in certain specific limits they can be separated and studied.

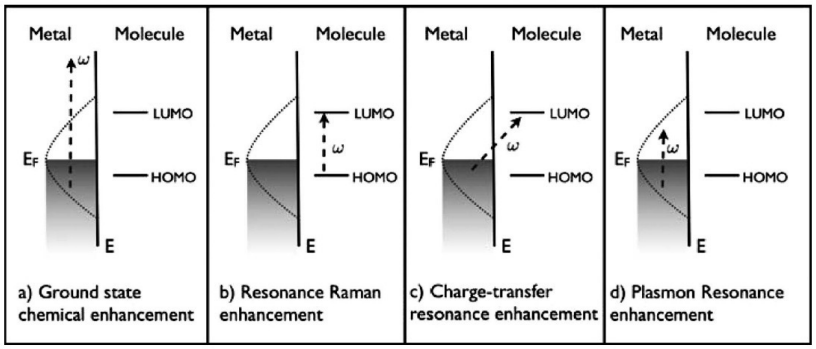

Fig. 6.13: Four different categorizers of the origin of chemical enhancement. [122] Figure reprinted with permission from Royal Society of Chemistry.

As a short summary, 1. a chemical enhancement leads to different intensity ratios of Raman modes compared to the pure spectra; 2. in order to experimentally analyze the involved chemical mechanisms, intensity ratios should be quantified; 3. the intensity ratios will be further shifted by the surface plasmon. Therefore, quantifying the surface plasmon's contribution to the ratio deviation is a key aspect for a better experimental understanding of the CMs.

In an On-chip SERS experiment, the samples to be measured usually consist of three components: target organic molecules, environment(surface of solid substrate) and metallic nanostructure. A laser excitation in Raman measurement could lead to photo-induced physical or chemical processes over time, for instance a photo bleaching. Such spontaneous "dynamic" phenomena would influences the Raman intensity, therefore they should also be considered. As shown in Fig. 6.5, during the whole measurement process, there is no drastic spectral change or the emergence of additional Raman modes, which means no considerable chemical reaction took place. However, the overall intensity decreases as a function of exposure time. Four significant Raman modes (around 1368, 1400, 1592 and 1620 cm^{-1}) are selected and fitted with Lorentz line-shapes. The intensity results are presented in Table 6.3. The intensities of each mode over time are plotted in Fig. 6.14. All the modes have a decreasing tendency with a characteristic time scale of 100 s, which

suggests that a photo-induced degradation happens rather than other fast chemical reactions. Moreover, the normalized intensities (divided by intensity of mode at 1620 cm^{-1}) are also calculated and shown in Fig. 6.15. It can be seen that the normalized intensity of the mode at 1368 cm^{-1} decreases, while the modes at 1400 and 1592 cm^{-1} increase in intensity. Therefore, the conventional CMs analysis method must be corrected by a "dynamic" contribution. A novel method for estimating CMs contribution to each Raman mode in such cases will be proposed as follows.

Mode / Measure	1368 cm^{-1}	1400 cm^{-1}	1592 cm^{-1}	1620 cm^{-1}
1st	224.5	240.6	226	543.7
2nd	114.1	139.5	144.8	295.9
3rd	83.1	105.7	112.4	222.1
4th	69.7	91.6	100.7	187.7
5th	58	78.4	87.4	158.6
6th	51.6	71.4	78.4	140.9
7th	45.4	64.9	72.5	124.1

Tab. 6.3: Mode intensities fitted from Malachite Green spectra in Fig. 6.5.

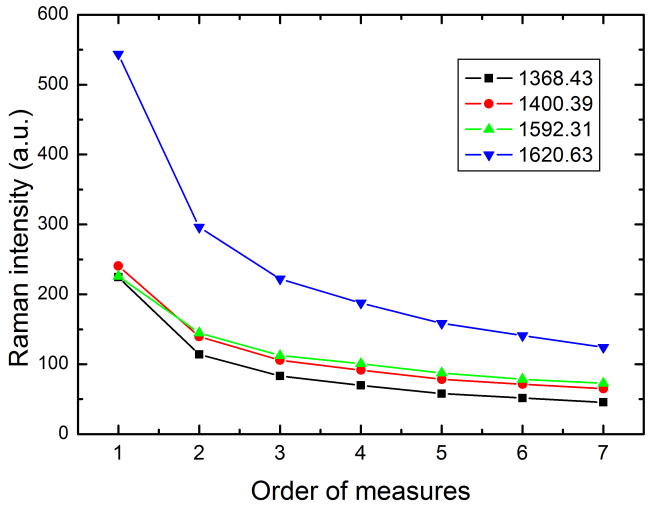

Fig. 6.14: As measured SERS mode intensity decay. Such decay is related to the light-induced degradation of malachite green.

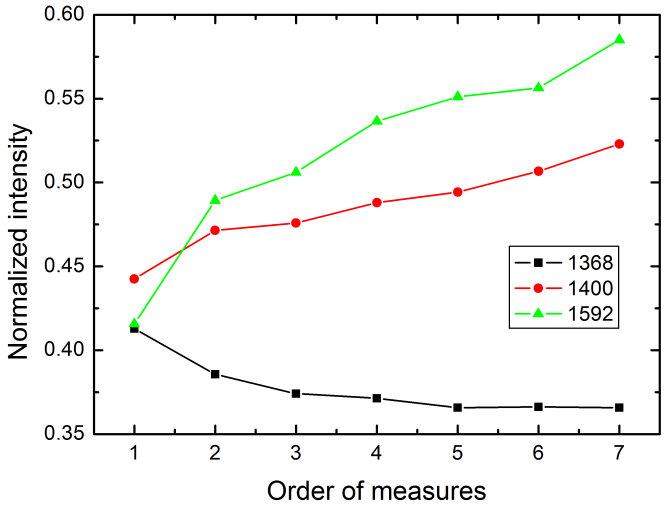

Fig. 6.15: Each SERS mode of Malachite Green has its own intensity decay tendency. Such figure, which contains mode selective behaviour, could be considered as a proof of the existence of CM by using a dynamic approach.

All decay curves shown in Fig. 6.14 are fitted to an exponential decrease, based on the mathematical discussion Eq. (6.3) and Eq. (6.4). It is found that Eq. (6.4), i.e., a second order exponential decay function I(n)=$A*exp(-B*n)+C*exp(-D*n)$ works much better than a first order exponential fitting curve. The order of the decay function should relate to the number of different degradation routes. The reason, why it can be well-fitted with a second order exponential decay function, could attribute to the facts that 1. malachite green has monomer and dimer (or aggregate) structures, therefore it could show different photo-induced degradation processes; 2. the intensity of the excitation light in the focal spot could be roughly separated into a weak and a strong section, and non-linear degradation involved; 3. the surface of Au/AAO contains phase-separated regions of pure Au and pure AAO, where an adsorption on Au or on AAO surfaces could lead to different life times. Regarding the first scenario, due to the genotoxic and carcinogenic properties of malachite Green and its application as a biocide in the aquaculture industry, malachite green has been extensively investigated especially with respect to its degradation. [123, 124] There are indeed several degradation routes. [125] However there is no difference between monomers and dimers (aggregate) of malachite green in those routes according to the reports, and a first order

degradation function commonly works very well. [125, 126] A deviation of the normalized mode intensities could only happen in this case. Therefore we can rule out the first scenario. The second scenario (or other purely physical mechanisms) would also be ruled out, because they are processes, which could not result in a modification of a normalized mode intensity as shown in Fig. 6.15. Finally, the third scenario is the most likely one: compared to a molecule on the AAO surface, a molecule adsorbed (or rather chemisorbed) on the Au surface could gain CMs, which changes the normalized mode intensities, and also locates it in the enhanced light field, which can reduce the lifetime.

The fitting results are shown in table 6.4. Two lifetime parameters B and D are plotted in the Fig. 6.16, to roughly estimate the possible lifetime parameters of Malachite Green in the experiment. It should be noticed that the lifetime is a property of molecules, and is related to the physical and chemical environment of the molecule. Therefore all Raman modes from the identical molecule should have the same lifetime. As shown in Fig. 6.16, the lifetime parameter B, which corresponds to the first degradation route, is of the order of 12.5 s. The parameter D, corresponding to the second route, is about 150 s and has a relative large possible distribution range, indicated by the shaded area.

Fitting	1368 cm^{-1}	1400 cm^{-1}	1592 cm^{-1}	1620 cm^{-1}
A	118±15.3	134.8±19	142.6±29	313.9±30
B	0.138±0.024	0.1058±0.0262	0.09783±0.0359	0.134±0.018
C	600.2±122	467.2±92.5	345.1±105	1295±229
D	1.596±0.274	1.365±0.293	1.272±0.479	1.571±0.239

Tab. 6.4: Fitting parameters based on the second order exponential decay function and dynamic mode intensity in Fig. 6.15.

According to Eqn. (6.1) and Eqn. (6.4), the intensity of each Raman mode as a function of n th measure is specified and rewritten as follows:

$$\begin{aligned} \iota_{mode1}(n) =& a_{mode1}e^{-Bn} + c_{mode1}e^{-Dn} \\ =& N_{[0,ce]}I_{ce}\alpha_{[mode1,ce]}e^{-Bn} + N_{[0,e]}I_e\alpha_{[mode1,e]}e^{-Dn}, \end{aligned} \tag{6.7}$$

where $N_{[0,ce]}$ and $N_{[0,e]}$ are the number of adsorbed (with CMs and EM) and non-adsorbed molecules (with only EM) at an initial time; I is the (enhanced) intensity of the excitation around the molecules. α_{mode1} corresponds to the native Raman cross-section of mode 1; B and D are lifetimes; and n is the order of measurement on sample(order of laser illumination).

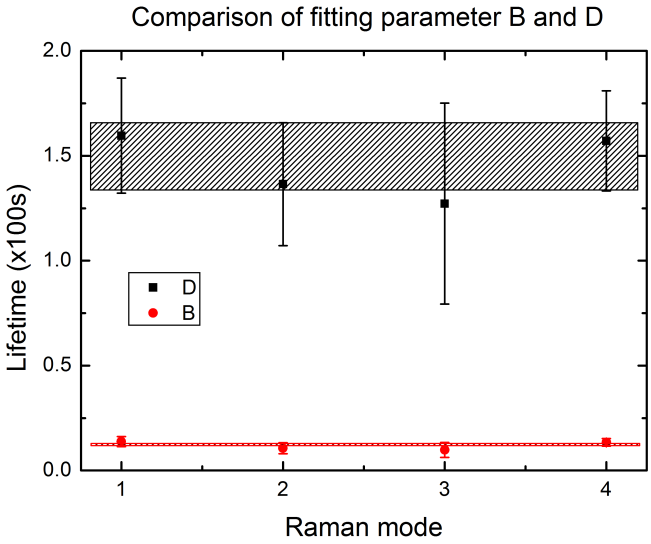

Fig. 6.16: Plotting of fitting results of parameter B and D in Tab. 6.4. Error bars indicate the 95% confidence ranges of the fitting results. Raman Modes numbered with 1, 2, 3 and 4 corresponds to the mode at 1368 cm^{-1}, 1400 cm^{-1},1592 cm^{-1} and 1620 cm^{-1},respectively.

Especially, when the first term is removed from the formula as shown in Eqn. (6.8), it corresponds to the case in which only EM contributes to an experiment.

$$\begin{aligned} \iota_{mode1}(n) =& c_{mode1}e^{-Dn} \\ =& N_{[0,e]}I_e\alpha_{[mode1,e]}e^{-Dn}, \end{aligned} \tag{6.8}$$

Please note that in this case, the intensity ratio of two modes should have the same or similar as intensity ratio as observed in common Raman spectroscopy, because both of them are equal to the ratio between native Raman cross-sections of these two modes as shown in Eqn. (6.9). This is helpful to distinguish the "CM and EM" and "only EM" terms in the expression.

$$\begin{aligned} \iota_{mode1}(n)/\iota_{mode2}(n) =& c_{mode1}e^{-Dn}/c_{mode2}e^{-Dn} \\ =& c_{mode1}/c_{mode2} \\ =& N_{[0,e]}I_e\alpha_{[mode1,e]}/N_{[0,e]}I_e\alpha_{[mode2,e]} \\ =& \alpha_{[mode1,e]}/\alpha_{[mode2,e]}, \end{aligned} \tag{6.9}$$

Since we accept the fact that parameters B and D are not mode-dependent. Therefore based on the new "most possible" shared parameters $B = 0.125$

and $D = 1.5$ (with unit: 100s) of four modes, all the four decay curves in Fig. 6.15 should follow the corrected second order exponential decay function

$$a{\cdot}e^{-0.125\cdot} + c{\cdot}e^{-1.5{\cdot}n}, \tag{6.10}$$

Therefore, all the four curves are fitted with the corrected second order exponential decay function 6.10, and the corrected fitting results are shown in Tab. 6.5.

Fitting	1368 cm^{-1}	1400 cm^{-1}	1592 cm^{-1}	1620 cm^{-1}
a	110.4±2	148.4±3.4	163.3±5.3	300.3±3.9
c	569.7±15	490.6±25.7	365.7±40	1249±29

Tab. 6.5: Fitting results of parameters a and c, if we accept $B = 0.125$ and $D = 1.5$ (100s) as the most possible estimation according to the results in Fig. 6.16.

A comparison between relative mode intensities of normalized powder, a and c related terms is shown in Fig. 6.17. All modes in one spectrum are normalized by the first mode (at 1368 cm^{-1}). According to the Fig. 6.17 we propose to use $c{\cdot}e^{-1.5{\cdot}n}$ as the "only EM" term, because from 1368 mode to 1620 mode, c' (green curve) also an up-down-down-up tendency as in the powder sample results (black curve) is observed, they are also rather close to each other. The deviation between "powder" and "c'" could be attributed to the crystalline property of "powder" malachite green.

Furthermore, the normalized intensity $a'_i = a_i/a_s$ of each mode (as shown in Fig. 6.17) could be expressed as follows:

$$\begin{aligned} a'_i =& a_{mode\ i}/a_{mode\ s} \\ =& N_{[0,ce]} I_{ce} \alpha_{[mode\ i,ce]} / N_{[0,ce]} I_{ce} \alpha_{[mode\ s,ce]} \\ =& \alpha_{[mode\ i,ce]} / \alpha_{[mode\ s,ce]} \\ & . \end{aligned} \tag{6.11}$$

Similar, the normalized $c'_i = c_i/c_s$ holds:

$$\begin{aligned} c'_i =& c_{mode\ i}/c_{mode\ s} \\ =& N_{[0,e]} I_e \alpha_{[mode\ i,e]} / N_{[0,e]} I_e \alpha_{[mode\ s,e]} \\ =& \alpha_{[mode\ i,e]} / \alpha_{[mode\ s,e]} \\ & . \end{aligned} \tag{6.12}$$

Therefore,

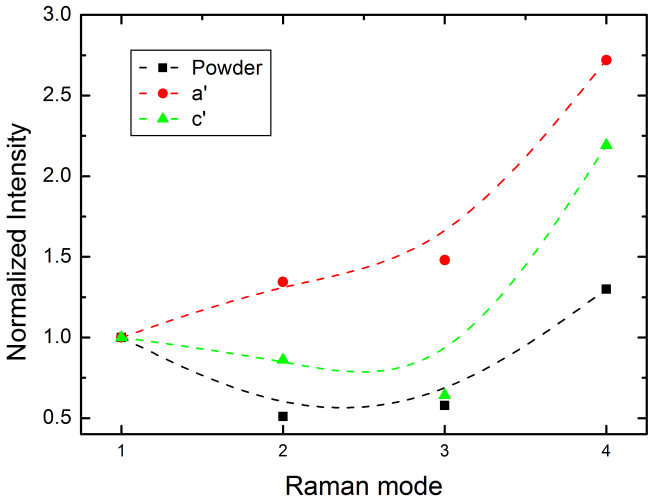

Fig. 6.17: Comparison among normalized fitting parameters a', c' and the intensity ratio from the powder sample. The similar one would be considered more likely as from contribution of "only EM" affected molecules.

$$\begin{aligned} a'_i/c'_i =& \frac{\alpha_{[mode\ i,ce]}/\alpha_{[mode\ s,ce]}}{\alpha_{[mode\ i,e]}/\alpha_{[mode\ s,e]}} \\ =& \frac{\alpha_{[mode\ i,ce]}/\alpha_{[mode\ i,e]}}{\alpha_{[mode\ s,ce]}/\alpha_{[mode\ s,e]}} \\ =& \frac{CEF_{mode\ i}}{CEF_{mode\ s}} \\ =& CEF'_{mode\ i}. \end{aligned} \tag{6.13}$$

where $CEF_{mode\ i} = \alpha_{[mode\ i,ce]}/\alpha_{[mode\ i,e]}$ indicates the CMs related additional enhancement factor for mode i, and $CEF'_{mode\ i}$ is the normalized enhancement factor by mode s.

Therefore, although the measured intensity ratios of the malachite green keep changing during the SERS measurement (as shown in Fig. 6.15), the native chemical enhancement contribution can still be estimated. As a result, the normalized chemical enhancement factors on the Au/AAO substrate by mode 1620 cm^{-1} are shown in table 6.6.

For comparison, the chemical enhancement factors for Malachite Green are calculated based on the static measurement results in Table 6.2, and the

	1368 cm^{-1}	1400 cm^{-1}	1592 cm^{-1}	1620 cm^{-1}
CEF'	0.81	1.26	1.86	1

Tab. 6.6: Normalized chemical enhancement factor of each selected mode according to this dynamic treatment.

corresponding normalized chemical enhancement factors and the correction-percentage hold:

	1368 cm^{-1}	1400 cm^{-1}	1592 cm^{-1}	1620 cm^{-1}
CEF'_{static}	0.51	1.26	1.24	1
Δ/CEF'_{static}	59%	0	50%	–

Tab. 6.7: Normalized chemical enhancement factor for Malachite Green based on a common static treatment and a comparison between results from the new dynamic treatment and common static treatment.

In summary, comparing to the conventional static SERS enhancement factor analysis, the results from dynamic approach here can describe the enhancement factor more precisely. This approach quantitatively model the SERS process, and is a potential fundamental tool for quantitative SERS application.

6.2 IDSERS

The intensity ratio among SERS modes is not only of fundamental interest for a further understanding of CMs of SERS as we discussed, but also for applications. As previously discussed, Raman spectroscopy is based on inelastic scattering processes of monochromatic light. The Raman shift is commonly used to identify materials via the molecular vibrations ("fingerprint" of a sample). Moreover, as a fast and non-destructive testing technique, Raman spectroscopy is cost-efficient and has been broadly applied as a qualitative chemical detecting or sensing tool in chemical, biological, pharmacy and clinical applications. [127, 128, 129] However there are also limits in quantitative detecting applications due to the variability of absolute SERS intensity, especially in a motionless SERS system: The absolute SERS intensity depends strongly on the nanomorphology of the system such as size and the shape of the nanostructures on the SERS substrate. Tiny variations of parameters of one single nano unit in principle will non-linearly fluctuate the plasmonic property and finally change the SERS intensity – for instance via the second enhancement (Fig. 6.18)[114] or the *plasmonic spectral shaping effect* (PSSE)

(Fig. 6.19)[115], which were discussed in the previous section. Those effects lead to the observation that each plasmonic antenna has its own specific optical response function, and the amplification in a SERS spectrum is not constant at each wave-length, but rather a non-linear function of wave-length. The exact contribution from such effects to the absolute Raman intensity at each wavelength is commonly unknown, unless each plasmonic nano unit will be characterized at each wavelength before starting Raman measurement.

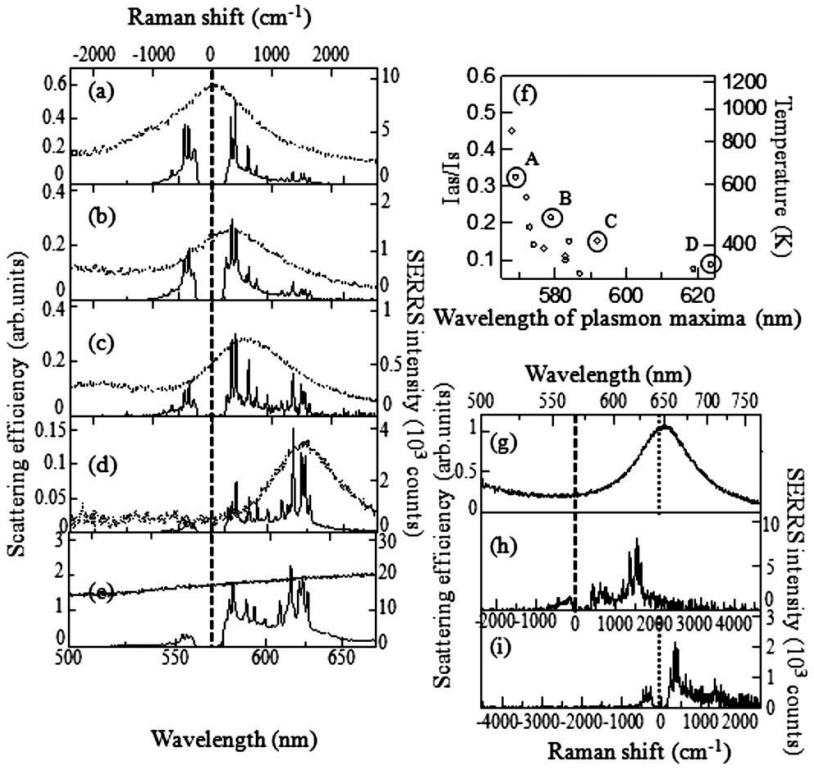

Fig. 6.18: Second enhancement attributes to the plasmon resonance Rayleigh scattering. [114] Figure reprinted with permission of American Physical Society.

The incident laser frequency should also be considered as an origin of variability of the absolute intensity. This is related to the resonance Raman effect: When the photo energy of the Raman excitation is comparable to the energy gap between HOMO and LUMO of the target molecule, an additional Raman signal amplification is usually gained due to a change in the electron population. Considering a relative complex electronic band structure, an exact quantification of such a Raman signal amplification is rather involved. In addition, the microscopic location of a target molecule within the aggre-

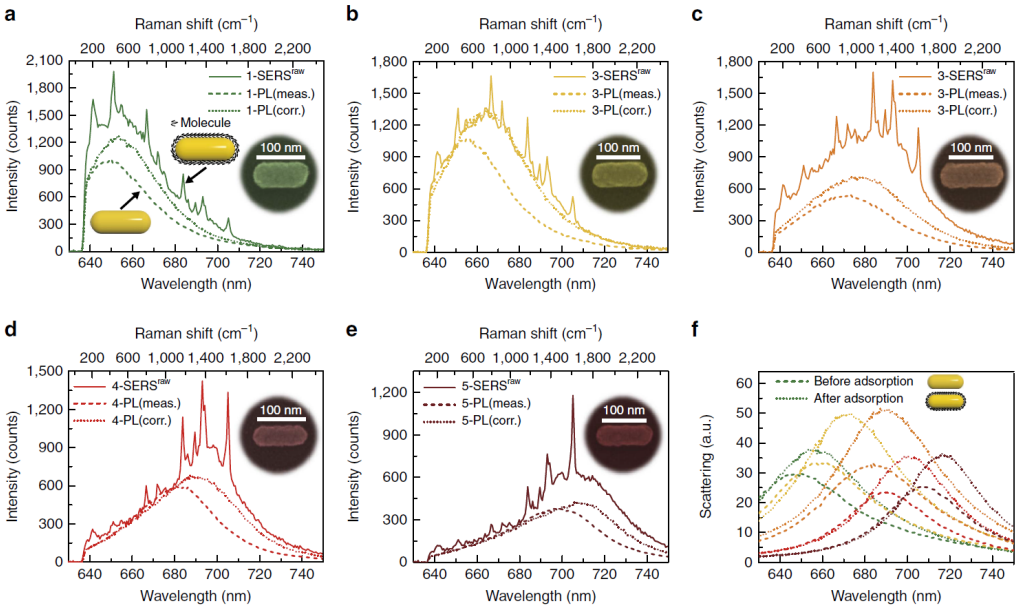

Fig. 6.19: Plasmonic spectra shaping effect(PSSE). [115] Figure reprinted with Creative Commons Licence.

gation of nano plasmonic units will also influence the absolute intensity of the SERS signal: When a molecule is located in the hot-spot between two plasmonic units, the enhancement of the signal would be extremely large. In contrast, when it is positioned away from the hot-spot, the enhancement factor is rather small. On the other hand, spatial distances between nano plasmonic units in a real SERS substrate are also fluctuating, while such distances dramatically affect the near-field properties of hot-spots. Therefore, a huge variability of the enhancement factor within a substrate will be observed in practice. [130] This leads to the difficulty of quantifying the absolute SERS intensity. Moreover, comparing the solid- to the liquid-based SERS detection, where Brownian motion is small/absent, the electromagnetic coupling between metallic nanounits in a motionless SERS system leads to a larger variation of the detected Raman signal. Finally, the calibration of a spectrometer which influences the collection efficiency, as well as other effects, such as the metal-molecule interaction, would also lead to great variations in the absolute intensity.

Therefore, it is a huge challenge nowadays to quantify molecules via absolute intensity measurements of Raman modes in SERS. Fig.6.20 shows a sketch of those effects, which vary the absolute intensity of a Raman mode in SERS.

In order to overcome the principle difficulties described above in the quan-

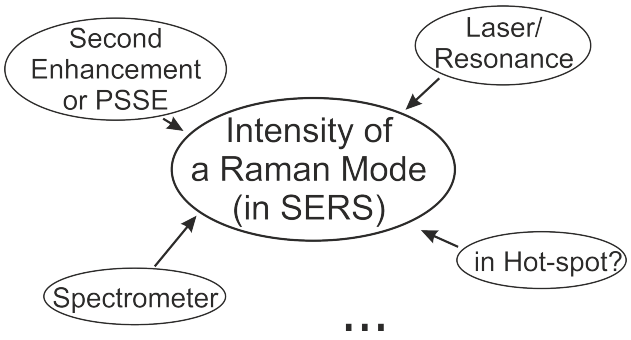

Fig. 6.20: Different factors contribute to the intensity of a Raman mode.

titative detection via absolute intensities, relative intensities of Raman signals are considered as an alternative. For instance, Raman signals from a solvent, from label molecules with known concentration, or from designed SERS substrates could be used as a reference of relative intensities for quantification of target molecules. A lot of studies were conducted throughout the last decades, that can be categorized into internal and external standardization. [131, 132, 133]

An internal standard in analytic chemistry refers to a chemical substance which is added to a sample during chemical analysis to correct any analyte loss during sample preparation. This internal standard is usually a compound that is very similar but not identical to the analyte in the sample, since the effect of the sample preparation for the internal standard signal should be equal in the case of an ideal species of interest relative to the amount of each substance. On the other hand this could also be used to determine the concentration of analyte by calculating the response factor. The internal standard methods are broadly applied in chromatography, mass spectrometry, NMR spectroscopy, etc.

Isotope edited internal standard (IEIS) is one of the most powerful internal standardization methods, because of the almost identical chemical properties and only slight molar mass differences between the target and its isotopologue. It is easy to correct any target loss during the sample preparation. This leads to a tremendous advance in clinical or environmental applications.

Two approaches, IEIS and SERS, can be combined for improving the accuracy of quantitative concentration measurements, only if:

- the analyte and its isotopologue can be distinguished from each other via SERS spectra.
- the necessary of understanding of absolute SERS intensity can be ignored within IEIS.

Refer to the first point, the slight molar mass difference between the analyte and its isotopologue in IEIS leads to an energy difference of the vibrational modes of a molecule, which is manifested by a change in the Raman shift in SERS spectra. Therewith, the analyte and its isotopologue can be distinguished from each other via spectra.

Refer to the second point, all the effects from setup such as from laser or spectrometer, which complicate the understanding of absolute SERS intensity (seen in Fig. 6.20), almost identically affect analyte and its isotopologue. They can be expressed as a coefficient in both absolute SERS intensities of analyte and its isotopologue. By measuring an intensity ratio between analyte and its isotopologue, this additional coefficient in the absolute intensities can be eliminated.

Such a technique is called *Isotope Dilution SERS* (IDSERS) or *Isotope Labeled SERS*. Generally speaking, in this technique an intensity ratio of Raman peaks between a target analyte and its isotopologue (as an internal standard) is determined first. Then the unknown concentration of the analyte can be determined from the intensity ratio and the known concentration of the reference isotopologue. This allows a sensitive, traceable and accurate concentration measurement that could compete with the more expensive isotope dilution mass spectrometry (ID-MS) [134, 135].

In the next section, *Isotope Dilution Surface Enhanced Raman Spectroscopy*(IDSERS), especially *On-chip Isotope Dilution Surface Enhanced Raman Spectroscopy* (On-chip IDSERS) will be discussed.

6.2.1 Introduction

In the case of IDSERS, a target species is mixed with its isotopologue. Due to the isotopic enrichment a slight change in molar mass of the spike molecule leads to a spectral shift of vibrational modes towards usually lower wavenumbers (for an increase in molar mass). Therefore, both target species and internal standard (isotopologue) are nearly equally affected by the complex contributions to the measurement uncertainty, so that these contributions can be nearly eliminated in this technique. A sketch of the general IDSERS process is illustrated in Fig. 6.21. There are two common approaches of IDSERS: single and double IDSERS. Both approaches start by measuring a set of reference mixtures, followed by generating and validating a PLS regression model from the resulting SERS spectra. In a single IDSERS measurement the spiked sample is measured. The SERS spectrum is used for predicting the amount of substance fraction of the analyte in the spiked sample. In a double IDSERS experiment the spiked sample is measured together with a reference sample simultaneously. Both SERS spectra are used to deter-

mine the amount of substance fraction of the analyte in the spiked sample, and then convert it to the analyte concentration together with its associated uncertainty.

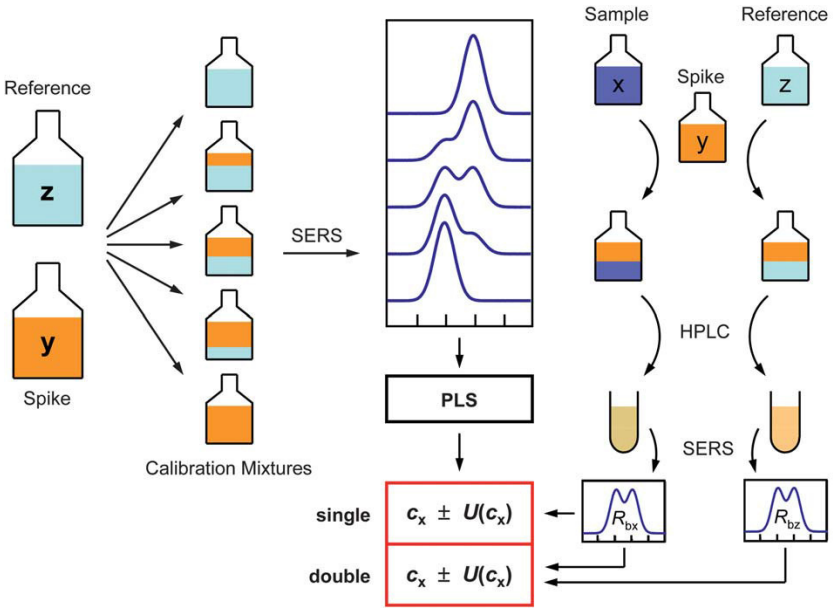

Fig. 6.21: A scheme of ID-SERS method. [134] In this work, a set of calibration mixtures from natural (reference, z) and isotopically labeled analytes (spike, y) is prepared and measured. Therewith a PLS calibration is performed. Sample (blood serum, x) and reference are spiked and further purified for SERS measurement. The isotopologue abundance ratios are predicted from the spectra and then converted into the analyte concentration c_x and the associated expanded uncertainty $U(c_x)$. Figure reprinted with permission from Royal Society of Chemistry.

Indeed, the uncertainty of ID-SERS experiments has been discussed from a practical point of view in literature. Frequently the chemical purity and isotopic enrichment of the isotopically labelled spike material are ambiguous, and therefore a main contribution to the overall uncertainty, based on the experience in reference procedures of ID-MS. [134, 135]. In this thesis the complexity from the IDSERS process itself will be focused. The theoretical limit of uncertainty analysis will be discussed as follows based on the principle of IDSERS. This will be helpful to improve the understanding of uncertainty contribution in IDSERS.

In an ID method, the isotope abundance ratio of references $r = C_1/C_2$ is

given by

$$r = \frac{I(n_1)}{I(n_2)} \tag{6.14}$$

where $I(n_1)$ and $I(n_2)$ denote intensity of the peaks in a spectrum accumulated from n_1 isotope spikes and n_2 target molecules in a measurement, respectively. In principle, the main difference between IDSERS and ID-MS experiments is the characteristics of the response functions $I(n)$. In ID-MS the number of molecules of analyte and its isotopologue can be directly counted, while on a SERS substrate, each isotope spike or analyte molecule will gain an individuate enhancement factor k. We can assume that the contribution from each molecule to the overall intensity would be $k\Omega$, where Ω is the Raman cross section of one molecule. Therefore, from a microscopic point of view, r holds

$$r = \frac{\sum_{i=1}^{n_1} k_i\Omega}{\sum_{j=1}^{n_2} k_j\Omega} = \frac{\sum_{i=1}^{n_1} k_i}{\sum_{j=1}^{n_2} k_j}, \tag{6.15}$$

where k_i and k_j abide by a distribution, which is based on the interaction between molecules and SERS substrate. Their sum $\sum_{i=1}^{n_1} k_i$ and $\sum_{j=1}^{n_2} k_j$ is defined as K_1 and K_2, respectively. The isotope ratio r can be expressed as $r = K_1/K_2$.

In theory, according to the central limit theorem, K_1 and K_2 tend towards a normal distribution, respectively, when there is a large number of probed molecules. And this should be independent from the distribution of the initial variables k_1 and k_2. If the probability density function of K_1 and K_2 is assumed as $K_1 \sim (\mu_1, \sigma_1^2)$ and $K_2 \sim (\mu_2, \sigma_2^2)$, respectively, the ratio r will be expressed as quotient of two normal random variables.

The problem of determining the ratio of two correlated normal random variables has been mathematically discussed by E. C. Fieller in 1932 and 1954, D.V. Hinkley in 1969 (a correction in 1970), and G. Marsaglia in 1965, 2004. r could be expressed as a complex integral. [136] If K_1 and K_2 are independent and have a Gaussian distribution with a mean value of zero, the form of their ratio distribution should be fairly simple, and can be described by a Cauchy distribution. There would be no definition of mean or variance in such Cauchy distribution case. In a more common case, the two distributions have non-zero mean values, and the correlation coefficient between variables K_1 and K_2 has to be taken into account. Thus, the form for the distribution of the ratio is more complicated:

1) if we assume the absence of correlation between K_1 and K_2, the prob-

ability density function of ratio r would be:

$$p(r) = \frac{b(r)\cdot d(r)}{\sqrt{2\pi}\sigma_1\sigma_2 a^3(r)}\left[\Phi\left(\frac{b(r)}{a(r)}\right) - \Phi\left(-\frac{b(r)}{a(r)}\right)\right] + \frac{1}{a^2(r)\cdot\pi\sigma_1\sigma_2}e^{-\frac{c}{2}}, \tag{6.16}$$

where, $a(r) = \sqrt{\frac{1}{\sigma_1^2}r^2 + \frac{1}{\sigma_2^2}}$, $b(r) = \frac{\mu_1}{\sigma_1^2}r + \frac{\mu_2}{\sigma_2^2}$,
$c = \frac{\mu_1^2}{\sigma_1^2} + \frac{\mu_2^2}{\sigma_2^2}$, $d(r) = e^{\frac{b^2(r)-ca^2(r)}{2a^2(r)}}$,
and Φ is the cumulative distribution function of the Normal distribution

$$\Phi(t) = \int_{-\infty}^{t}\frac{1}{\sqrt{2\pi}}e^{-\frac{1}{2}u^2}\mathrm{d}u.$$

2) if we assume that there is a correlation between K_1 and K_2 and the correlation coefficient is ρ, then the probability density function of ratio r would be modified as:

$$p(r) = \frac{b(r)\cdot d(r)}{\sqrt{2\pi}\sigma_1\sigma_2 a^3(r)}\left[\Phi\left(\frac{b(r)}{\sqrt{(1-\rho^2)}a(r)}\right) - \Phi\left(-\frac{b(r)}{\sqrt{(1-\rho^2)}a(r)}\right)\right] + \frac{\sqrt{(1-\rho^2)}}{a^2(r)\cdot\pi\sigma_1\sigma_2}e^{-\frac{c}{2(1-\rho^2)}}, \tag{6.17}$$

where, $a(r) = \sqrt{\frac{1}{\sigma_1^2}r^2 - \frac{2\rho r}{\sigma_1\sigma_2} + \frac{1}{\sigma_2^2}}$, $b(r) = \frac{\mu_1}{\sigma_1^2}r - \frac{\rho(\mu_1+\mu_2 r)}{\sigma_1\sigma_2} + \frac{\mu_2}{\sigma_2^2}$,
$c = \frac{\mu_1^2}{\sigma_1^2} - \frac{2\rho\mu_1\mu_2}{\sigma_1\sigma_2} + \frac{\mu_2^2}{\sigma_2^2}$, $d(r) = e^{\frac{b^2(r)-ca^2(r)}{2(1-\rho^2)a^2(r)}}$,
However, three challenges increase the complexity of such a ratio distribution in a real on-chip IDSERS measurement:

- *the exact mathematical treatment of the ratio of two normal random variables is nowadays still under discussion.* Practical rules are developed only for specific analytical approximations, or by numerical studies depending on specific prerequisites. [137, 138] For instance, Marsaglia showed that a ratio of correlated normal random variables $W = X_1/X_2$ could be translated into a $Z = \frac{a+Y_1}{b+Y_2}$ form, where Y_1 and Y_2 are independent $N(0,1)$ variables. With the prerequisite $a < 2.256$ and $b > 4$, the ratio Z is itself approximately normally distributed with a mean value $\mu = a/(1.01b - 0.2713)$ and a variance $\sigma^2 = (a^2+1)/(b^2 + 0.108b - 3.795) - \mu^2$.

- *K_1 and K_2 are extracted from an unknown distribution of k, which is substrate-dependent in on-chip IDSERS, and each substrate is unique and usually disposable.* A variation of parameters of substrates will drastically alter the plasmonic property-related K of the whole system. It is neither easy to exactly model such a many-body system, nor to manufacture such metallic structures at a sub-nanoscale in a well-controlled way. Therefore, it is not easy to predict the mean value μ and the variance σ^2 of K_1 or K_2 on each individual SERS substrate.

- *the contribution from the analyte itself will influence the statistics.* If the concentration is so low that the sample size in the microscope field of view is small enough, it would be possible that t-distributes will replace the normal distribution in the ratio formula.

Moreover, it will be more challenging to determine the statistics of an on-chip IDSERS measurement, when light-induced degradation of isotope spikes and target molecules occurs. It leads to a decreasing n, and consequently K_1 and K_2 are dynamic within one acquisition period of a spectrum.

6.2.1.1 Subsystem

Ishikawa diagrams have been first developed in 1968 by Kaoru Ishikawa, a japanese organizational theorist, as cause-and-effect diagrams. Ishikawa diagrams describe the causes of a specific event and are commonly applied in product design and quality defect prevention to identify potential factors causing an overall effect.

The standard *ISO 9004-4* gives the following description "A cause-and-effect diagram is used to analyze cause-and-effect relationships; to communicate cause-and-effect relationships; and to facilitate problem solving from symptom to cause to solution". [139] Such cause-and-effect diagrams start with a horizontal arrow, the main bone. Major categories of causes are represented as new arrows pointing to the main bone, to identify the effects of the causes on the event. Factors to be considered are commonly categorized as data and information systems, environment, equipment, materials, measurements, methods, and observer. [139]

From a metrology point of view, Ishikawa diagrams are a compact way to identify, illustrate and structure the effects of input quantities on an output quantity, which usually is the measurand of interest, and then facilitate the creation of the uncertainty budget for the measurement result. Also the expression of system equations in mathematical form is facilitated.

However, in a nano complex system such as IDSERS, it would be challenging to accurately determine influences (for instance, the absolute en-

hancement factor k) from a large number of causes, which are involved in the measurement. In addition, these causes could also influence each other. Therefore, the the uncertainty propagation is typically very complicated.

Since the most of the "unknown" causes-effects in IDSERS are related to the substrate, a "breakdown" of the system would be a starting approach to determine on-chip IDSERS measurement uncertainty as suggested in author's previous work. [140] With that we would have a possibility to combine the most complex uncertainties into the "SERS substrate" subsystem and analyze them for instance via the Monte Carlo method, and then carry out the uncertainty analysis within rest subsystems.

As shown in Fig. 6.22, an Ishikawa diagram is developed for On-chip IDSERS by following the "subsystem" idea. In this study the uncertainty associated with the enhancement factor K (the "SERS substrate" branch) is mainly focused, so a rather simplified Ishikawa diagram will be sufficient here.

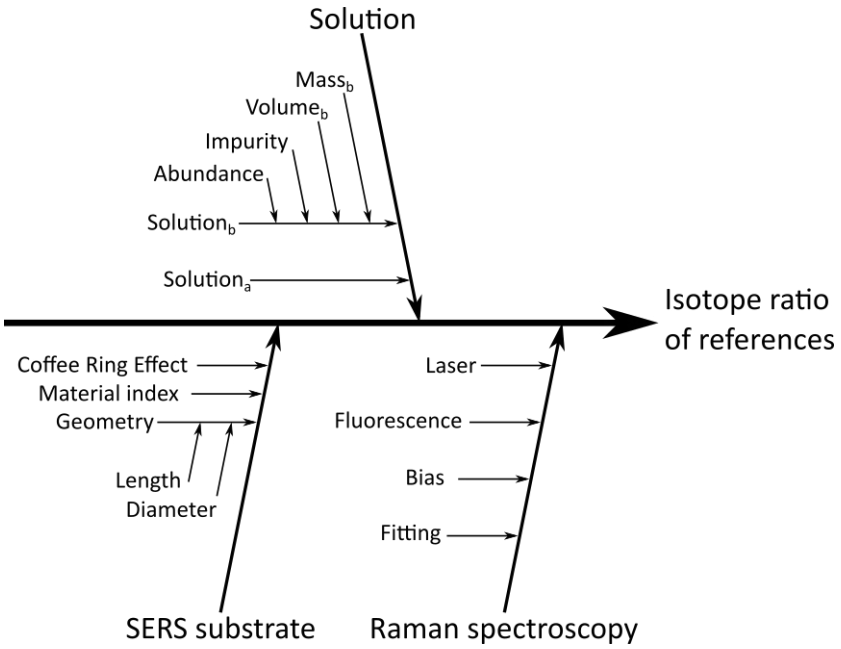

Fig. 6.22: An Ishikawa diagram for On-chip IDSERS.

For the sub-branch"SERS substrate" in Fig. 6.22, the so-called "Coffee Ring Effect" influences the choice of proper statistics. This effect describes a circular pattern of concentration distributions left by a drop of solution after it evaporates. The phenomenon is named after the characteristic ring-like deposit along the perimeter of a spill of coffee. The mechanism behind this effect is related to differential evaporation rates across the drop: liquid

evaporating from the edge is replenished by liquid from the center, and the resulting edgeward flow can carry nearly all the dispersed material to the edge. As discussed in the last section, when the field of view of a microscope is focused in the center of such a "coffee ring", the concentration of the dispersed analyte in the field of view could be low enough, to achieve a quasi-single molecule level. In this case the t-distribution would be applied.

The "material index" responds to fluctuations of the optical path length between neighbors in arrays. It includes both fluctuations of refractive indices of the matrix material and a position dependence of metallic nano particles from their sites in an ideal super-lattice. This affects mainly nano-arrays or aggregations, which offer hot-spots.

The "geometry" responds to a deviation of parameters within individual nano particles. For instance, in the case of AAO/Au nanorod substrates, the length and diameter of the rods should be considered, especially when the IDSERS utilizes the longitudinal mode of the surface plasmon.

6.2.2 Modelling, Monte Carlo Simulation and Analytical Understanding

6.2.2.1 Modelling the Intensity of Raman Signal

Numerical studies are carried out and discussed in this part for a better understanding of uncertainty in IDSERS. For this purpose, the Raman intensity should be modelled firstly as a function of parameters.

We can assume that the whole process can be divided in two steps:

- the incident laser light is scattered (amplified) by the surface plasmon, which then excites the target molecules. A Raman signal is generated.
- The Raman signal is scattered (amplified) by the surface plasmon, and detected by a spectrometer.

Therefore, it is suggested to model the intensity problem as shown in Fig. 6.23, and to simplify the amplification with a factor q. The factor q relates to not only the surface plasmon's properties but also is site-dependent. It would be reasonable to assume that for each single site near to surface plasmon, intensity of incoming light can be amplified by a corresponding factor q, no matter this input is laser or Raman emission from analyte.

There are several models to describe the amplification related to the surface plasmon in sub-wavelength metal particles: *Quasi-Static approximation* and *Mie Theory* as described in section 2.2. In a quasi-static approximation, the scattering cross-section is expressed by Eq. 2.9, and the amplification is given by $C_{scat} \propto a^6$, where a is the radius of the metallic nano particle. In Mie theory the relation between C_{scat} and a is more complicated, but it can

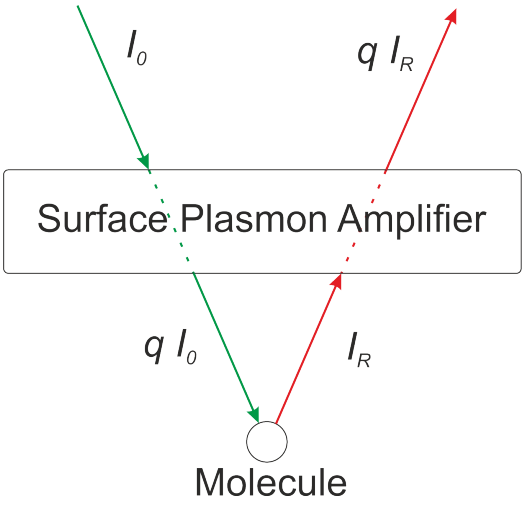

Fig. 6.23: AAO/Au transmission under different angles of incident light. I_0 corresponds to light field intensity of incident laser and I_R is the intensity of the Raman emission. It would be reasonable to assume that for each location around surface plasmon, where a molecule sited, intensity of incoming light can be amplified by a factor q no matter this input is laser or Raman emission from analyte.

be expressed as a Taylor series expansion and thus be approximated. For the Au/AAO substrates discussed in this thesis, the radius of the Au nanorod is around 16 nm and small enough. It is reasonable to assume a proportionality relation between C_{scat} and a^n. Accordingly, if we take for instance $n = 6$, we find that $k_i = q_i^2 \propto a_i^{12}$.

As discussed hereinabove, a (small) fluctuation of the nanorod diameter as well as the gap between neighboring rods can not be avoided during the fabrication of a SERS substrate. Fabrication resulting a size fluctuation (standard deviation) below $5\% \sim 10\%$ is typically considered as well-controlled. Here, a normal distribution is suggested to be used to describe such fluctuations. As shown in Fig. 6.24, for simplification, the mean value of the normalized radius is set as 1, and the theoretical distributions with different standard deviations (parameter sigma) range from 0.01 to 0.1 ($a \sim N(1, \sigma^2)$) are plotted. In contrast, in Fig. 6.25, 100000 random numbers are generated to numerically simulate the distribution of radius. It is clear that, the Monte-Carlo simulation represents the theoretical distributions well, it will be applied in the all numerical experiments as follows.

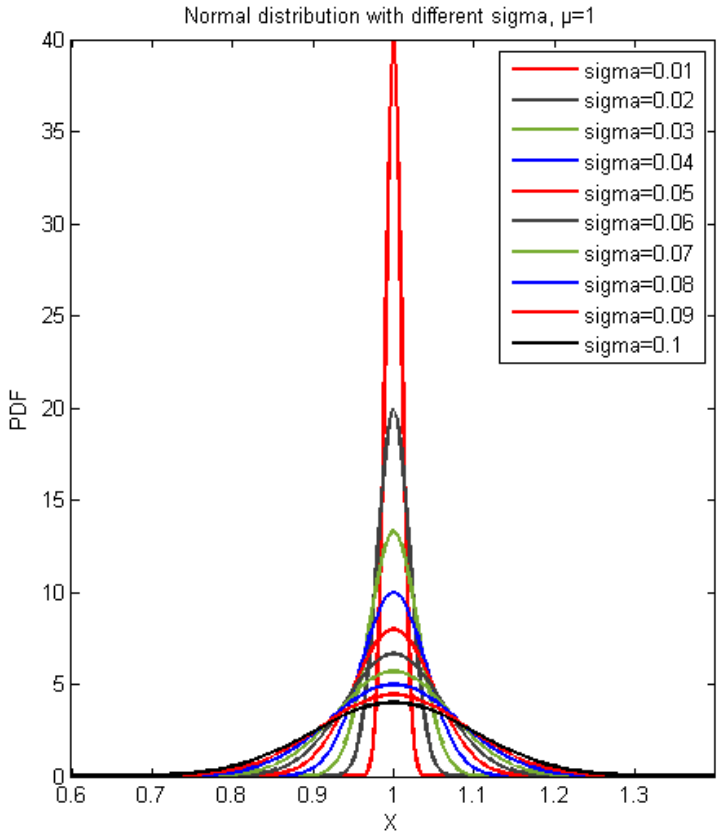

Fig. 6.24: A set of normal distribution curves with different standard deviations. In practice, fabrication of plasmonic nanostructures around dozens of nanometer with a 10% size fluctuation is nowadays still challenging.

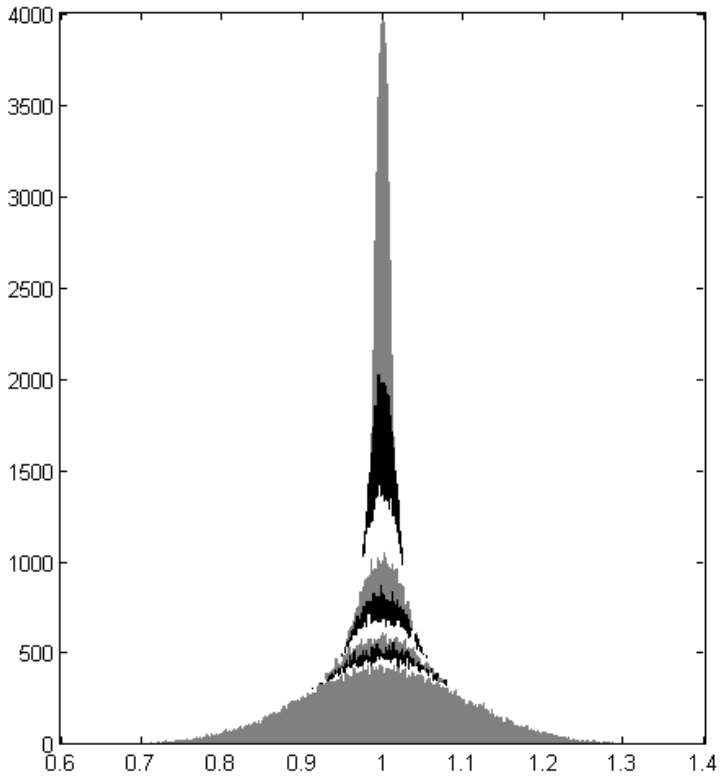

Fig. 6.25: A set of simulated radius distributions with different standard deviations. 100000 pseudo-random numbers are generated for each sigma. It is clear that, a simple Monte-Carlo simulation can represent the theoretical distributions well.

For simulations of the intensity (enhancement factor) of the detected Raman signal from the i-th molecules:

$$k_i \sim a_i^m \tag{6.18}$$

$$a_i \sim N(1, \sigma^2), \tag{6.19}$$

It is clear that the parameters σ and m will influence the distribution of the enhancement factor. Therefore, a set of numerical calculation are shown in the following, in order to clarify the tendency of the enhancement factor k as a function of the power m and the standard deviation σ.

As seen from the histogram in Fig. 6.26, a cross section $C_{abs} \propto a^3$ (absorption cross section) and a cross section $C_{sca} \propto a^6$ (scattering cross section) are simulated, while the radius of the nanorod follows a normal distribution in Eqn. 6.19 with $\sigma = 0.1$. The first consequence here is clear that increases of the power m lead to increases of asymmetry of the cross section distribution, when the standard deviation σ is fixed.

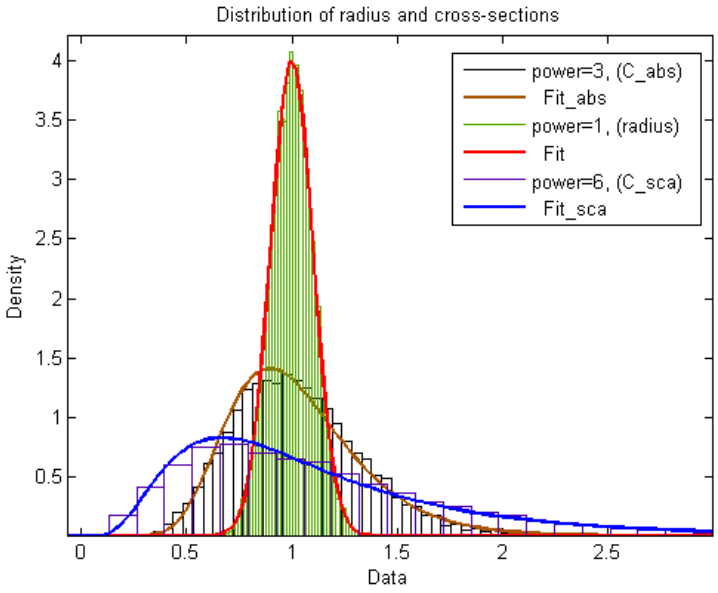

Fig. 6.26: Distribution of cross-sections with different power numbers. The green, brown and purple histogram refers to numerical simulation with power=1, 3 and 6, respectively. Increasing the power m can lead to an increasing asymmetry of the cross section distribution.

At the same time, the standard deviation σ also influences the asymmetry of the distribution. As shown in the histogram in Fig. 6.27, when the power

m is fixed as 6 for example, a larger standard deviation leads to more reinforced asymmetry. The second consequence holds: increases of the standard deviation σ lead to increases of asymmetry, when power m is fixed.

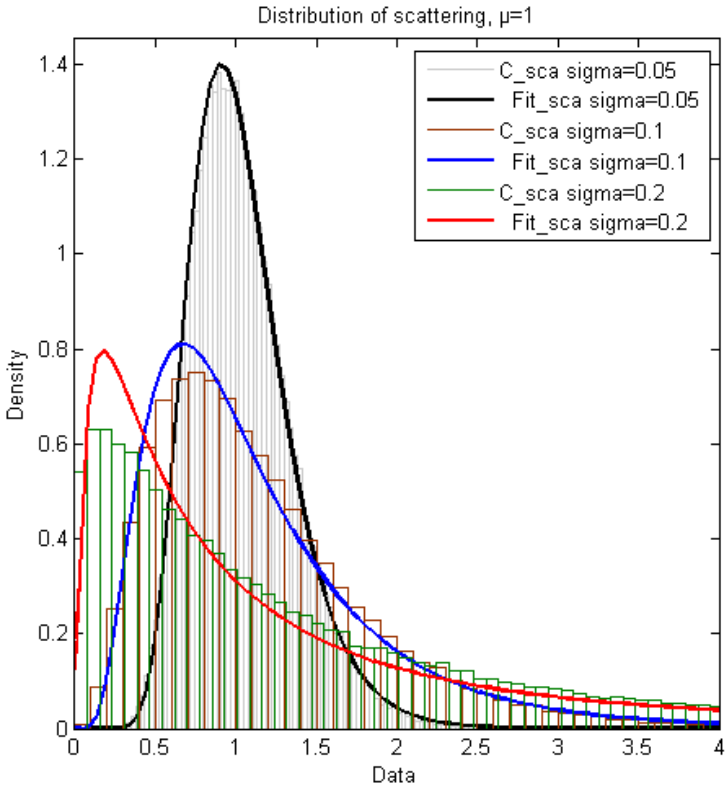

Fig. 6.27: Distribution of scattering cross section with different standard deviations. The power m is fixed as 6. It is clear that increasing the standard deviation σ lead to an increasing asymmetry of the distribution.

Please note that all histograms in both Fig. 6.26 and 6.27 are fitted by a *log-normal distribution*. A log-normal (or lognormal) distribution is a continuous probability distribution of a random variable whose logarithm is normally distributed. Mathematically, if the random variable X is log-normally distributed, then $Y = ln(X)$ has a normal distribution. In other words, if Y has a normal distribution, then the exponential function $X = exp(Y)$, has a log-normal distribution.

The *PDF* of a log-normal distribution holds:

$$f(x) = \frac{1}{x\sigma\sqrt{2\pi}} e^{-\frac{(lnx-\mu)^2}{2\sigma^2}}. \tag{6.20}$$

and

$$\begin{aligned} mean: \ E[X] &= e^{\mu+\frac{\sigma^2}{2}}, \\ variance: \ V &= (e^{\sigma^2}-1)e^{2\mu+\sigma^2}. \end{aligned} \tag{6.21}$$

In principle, for a power of a normal distributed random variable, $Y = Z^m, Z \sim N(\mu, \sigma^2)$, the PDF of Y can be mathematically described as follows:

$$\begin{aligned} F_Y(y) &= P(Y \le y) \\ &= P(Z^m \le y) = P(Z \le y^{\frac{1}{m}}) \\ &= \int_{-\infty}^{y^{\frac{1}{m}}} \frac{1}{\sigma\sqrt{2\pi}} e^{-\frac{(x-\mu)^2}{2\sigma^2}} dx \end{aligned} \tag{6.22}$$

$$\begin{aligned} f_Y(y) &= \frac{dF_Y(y)}{dy} \\ &= \frac{1}{\sigma\sqrt{2\pi}} e^{-\frac{(y^{\frac{1}{m}}-\mu)^2}{2\sigma^2}} \cdot \frac{1}{m} y^{\frac{1}{m}-1} \end{aligned} \tag{6.23}$$

However, a log-normal distribution is still suggested to be used in fitting instead of Eqn. 6.22 in on-chip IDSERS issues for the following reasons: 1. In probability theory, a log-normal process is the statistical realization of the multiplicative product of many independent random variables, each of which is positive. In the realistic physical process of plasmonic enhancement, there is not only the variation of the radius of particles, but also a variation of the gap between particles, a variation of the refractive index of the surrounding materials or other factors influencing the overall process; 2. The line-shape of the two distributions are quite similar, especially when the variation is much smaller than the dimension. This tendency can be easily found in Fig. 6.27: the smaller the standard deviation, the better similarity between the two distributions is achieved. Furthermore, the second reason can be roughly explained by a Taylor series expansion.

$$f(x) = f(a) + \frac{f'(a)}{1!}(x-a) + \frac{f^{(2)}(a)}{2!}(x-a)^2 + \ldots + \frac{f^{(n)}(a)}{n!}(x-a)^n + R_n(x), \tag{6.24}$$

When $f(x) = e^x$, $a = 1$ and $|x-a| \ll 1$,

$$\begin{aligned} e^x &= e + \frac{e}{1!}(x-1) + \frac{e}{2!}(x-1)^2 + \ldots + \frac{e}{n!}(x-1)^n + R_n(x), \\ &= e\left[1 + \frac{(x-1)}{1!} + \frac{(x-1)^2}{2!} + \ldots + R_n(x)\right] \\ &\approx ex \end{aligned} \tag{6.25}$$

and similarly,

$$e^{mx} = (e^x)^m \approx (ex)^m = e^m x^m \tag{6.26}$$

where, when x follows a normal distribution (mx has a normal distribution form), e^{mx}, which approximates to $e^m x^m$, obeys log-normal distribution.

Such a log-normal distribution approximation is suitable for experimental results. [130] The experimental measurement of the distribution of site enhancements are shown in Table 6.8, and plotted as symbols in Fig. 6.28. This result is fitted by a log-normal distribution shown as the red curve.

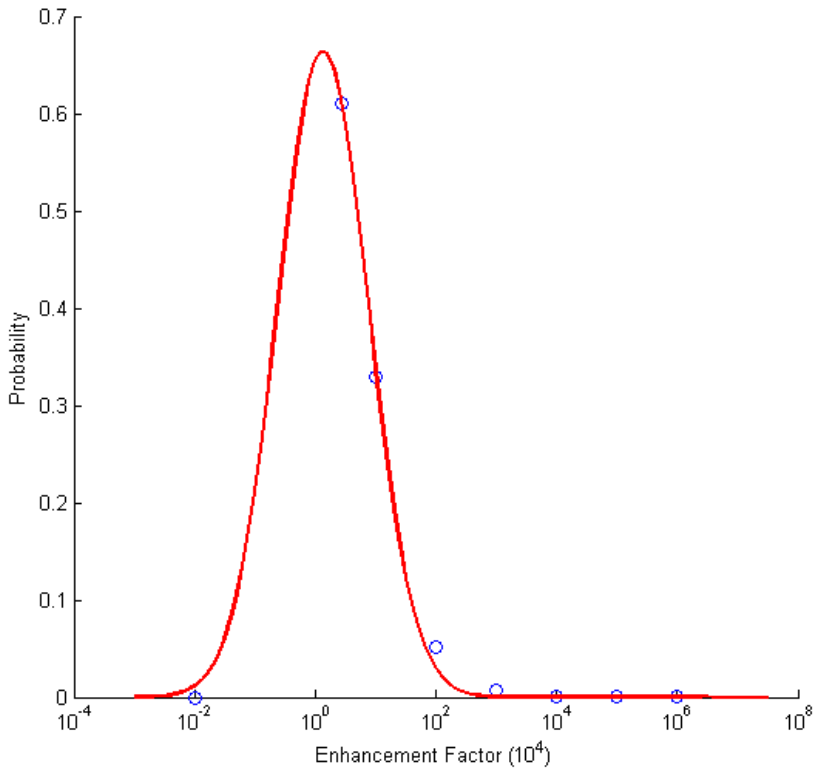

Fig. 6.28: Fitting the experiment results from Fang et al. [130] by a log-normal distribution. Blue symbols are response to the results in the reference, while the red curve is a log-normal fit.

As shown in the Fig. 6.28, the measurement results can be well fitted by a log-normal distribution *PDF* Eq. 6.20 with the following parameters (within a 95% confidence bounds): $\mu = 3.26(2.63, 3.891)$ and $\sigma^2 = 2.961(1.888, 4.034)$ (unit 10^4 and 10^8, respectively). For a random X, which follows such a distribution, the mean value is 115.07 (10^4) and the standard deviation is

Raman enhancement factors	percentage of molecules
$\leq 2.8 \times 10^4$	0
2.8×10^4 to 1×10^5	61%
10^5 to 10^6	33%
10^6 to 10^7	5.1%
10^7 to 10^8	0.7%
10^8 to 10^9	0.08%
10^9 to 10^{10}	0.006%
$\geq 10^{10}$	0.0003%

Tab. 6.8: Experimental results from Fang et al. [130] In a SERS measurement, molecules gain enhancement factor with a huge difference. The minority of the molecules contribute to the majority of the Raman signal.

495.89 (10^4) due to the intensive asymmetry. This influences the rate of convergence.

Therefore, based on Eq. (6.18), we extract the power $m = 24$, which corresponds to both dimension and site fluctuation of nanoparticles. Distributions with varying particle size standard deviations ($\sigma = 0.01, 0.03, 0.05$ and 0.10) are numerically calculated and shown in Fig. 6.29 and 6.30. It is clear that a larger particle size standard deviation σ leads to a larger skewness; and when $\sigma = 0.1$, the line-shape of the distribution curve is similar to the experimentally measured *Enhancement Factor* (EF) distribution in reference [130]. Each curve here is fitted and represented as a log-normal expression, which will be used as a Random number generator later in the following section.

Additionally, please note as shown in Fig. 6.30, that for $\sigma = 0.10$ most molecules gain such a low enhancement factor, that they don't contribute considerably to the collected Raman signal I. while minor molecules which gain relative huge enhancement factors make the main contribution to I.

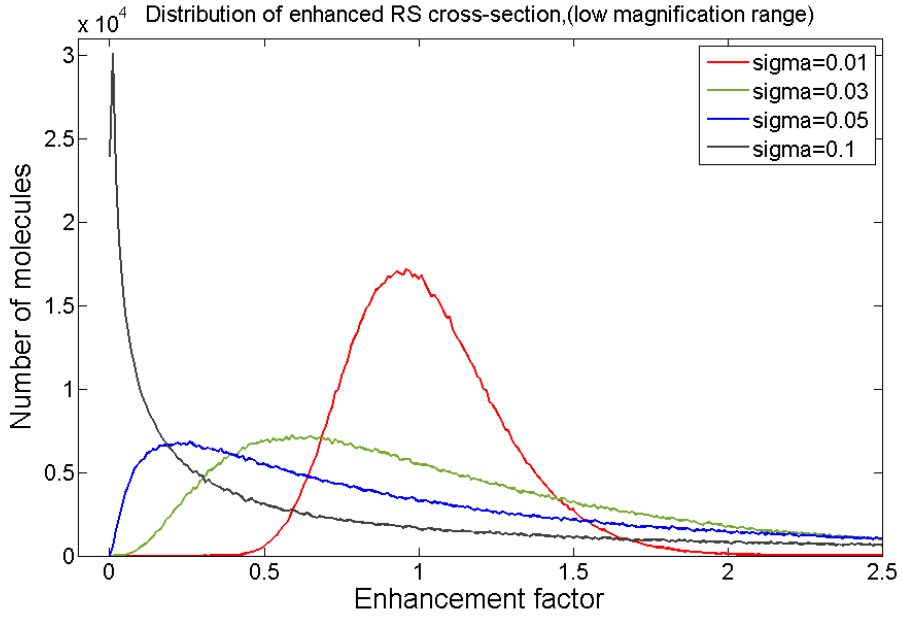

Fig. 6.29: Distribution of enhanced RS cross-section (low magnification range). Size distribution influences the skewness of PDF of SERS signal intensity. The $\sigma = 0.10$ curve has a similar line-shape to the experimentally measured *EF* distribution in literature [130].

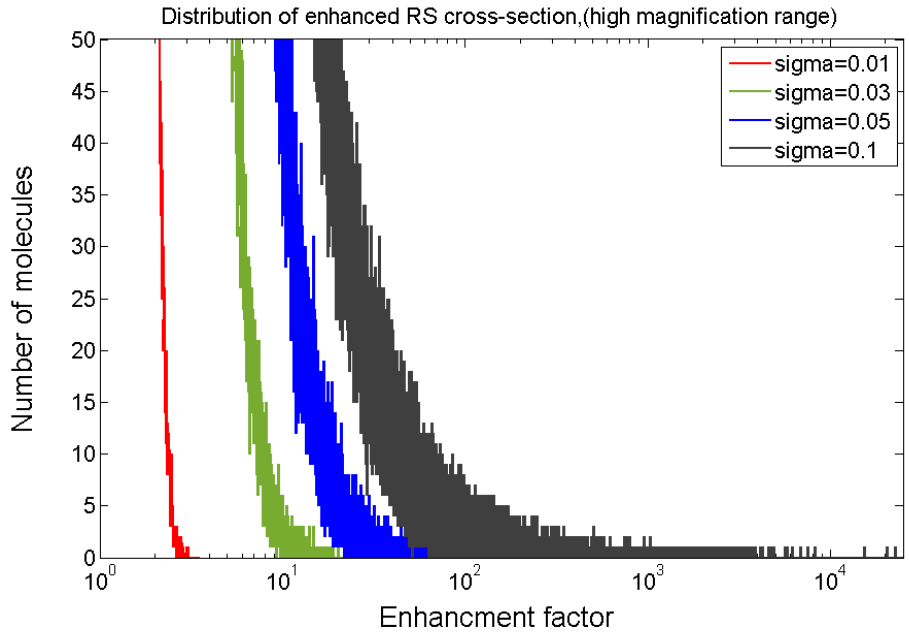

Fig. 6.30: Distribution of enhanced RS cross-section (high magnification range). Minor molecules which gain huge enhancement factors make the main contribution to Raman signal I.

Beside distribution of enhancement factor k of a single molecule, the sample size(how many analyte molecules involved in measurement) should also be considered in IDSERS issues. According to the classical CLT (*central limit theorem*), ***for a large enough n***, the distribution of the sample average $S_n := \frac{X_1+\cdots+X_n}{n}$ is close to the normal distribution with a mean value μ and a variance $\frac{\sigma^2}{n}$. Therefore,

$$I = \sum_i^n X_i = n \cdot S_n \sim N(n\mu, (\sqrt{n}\sigma)^2). \tag{6.27}$$

It is clear that the sample size n influences the *coefficient of variance*, and $\frac{\sigma}{\sqrt{n}\mu} = 4.31/\sqrt{n} \times 100\%$, according to the fitting of our experimental results. Therefore, for an intensity SERS measurement, it is here suggested that the Raman signal from at least $10,000$ molecules should be collected in the measurements. However, ***if n is too small***, i.e., it approaches the quasi single-molecule level, the intensity based molecular concentration evaluation would become complected. A small n would influence the skewness of the probability distribution, and it could be that the collected signal I (the sum of all Raman signal from all target molecules in the view of field, $I = \sum_i^n X_i$)

in repeating measurements doesn't follow a normal distribution at all. Therefore, the intensity ratio problem in an IDSERS is more complicated in such a case.

6.2.2.2 Monte Carlo Simulation and Analytical Understanding

Through simulation, we will seek for a tendency from the parameters, which mainly influence the IDSERS uncertainty, based on the master equation 6.28.

$$R = \frac{I_1}{I_2} = \frac{\sum_i^{n_1} X_i}{\sum_j^{n_2} X_j} = \frac{\sum_i^{r \cdot N} X_i}{\sum_j^{N} X_j}, \tag{6.28}$$

where X_i and X_j obey log-normal distribution. n_1 and n_2 are the number of analyte molecules and its isotopologue, and $n_1 = r \cdot n_2 = r \cdot N$, where r is the actual ratio.

Therefore, first of all in the simulation, the SERS signal intensity of individual molecule X_i generated as particle size distribution corresponding log-normal distributed Random numbers as clarified in the previous section. Secondly, the influence of different number n of the molecules on the SERS intensity ratio $I(n_1)/I(n_2)$ in a single spectra-shot is involved, and the intensity ratio between analyte and its isotopologue can be then simulated. In detail, the Monte Carlo simulations in this section are carried out with varying standard deviation of particle size σ = 0.01, 0.03, 0.05 and 0.10, different target molecule number N = 10000, 1000 and 100 also different true values of molecular number ratio r = 1, 2, 3, 4 and 5. To balance the computational resource cost and accuracy of simulation results, a numerical simulation for each parameters combination has 10000 iterations. More details of the simulations can be seen in the source code in Appendix A.

Simulated cross-validation of concentration ratio based on each single spectrum obtained from 10000, 1000, and 100 molecules, respectively, are shown in Fig. 6.31, 6.32 and 6.33. A larger particle size variation (resulting in a larger skewness) leads to a larger standard deviation in all the three groups. As discussed, the *EF* distribution with sigma= 0.1 is comparable to the realistic on-site enhancement. Focusing on sigma= 0.1 simulations, with a detection of 10000 molecules, the standard deviation is acceptable. With the detection of 1000 molecules, the standard deviation is appreciable. In contrast, as shown in Fig. 6.33, with 100 molecules per spectrum, the accuracy of the ratio evaluation from a single measurement is rather limited. For that, a comparison is shown in Fig.6.34.

Simulated ratio cross-validation can be analyzed by calculating the mean value and variance, which are given in Tab. 6.9.

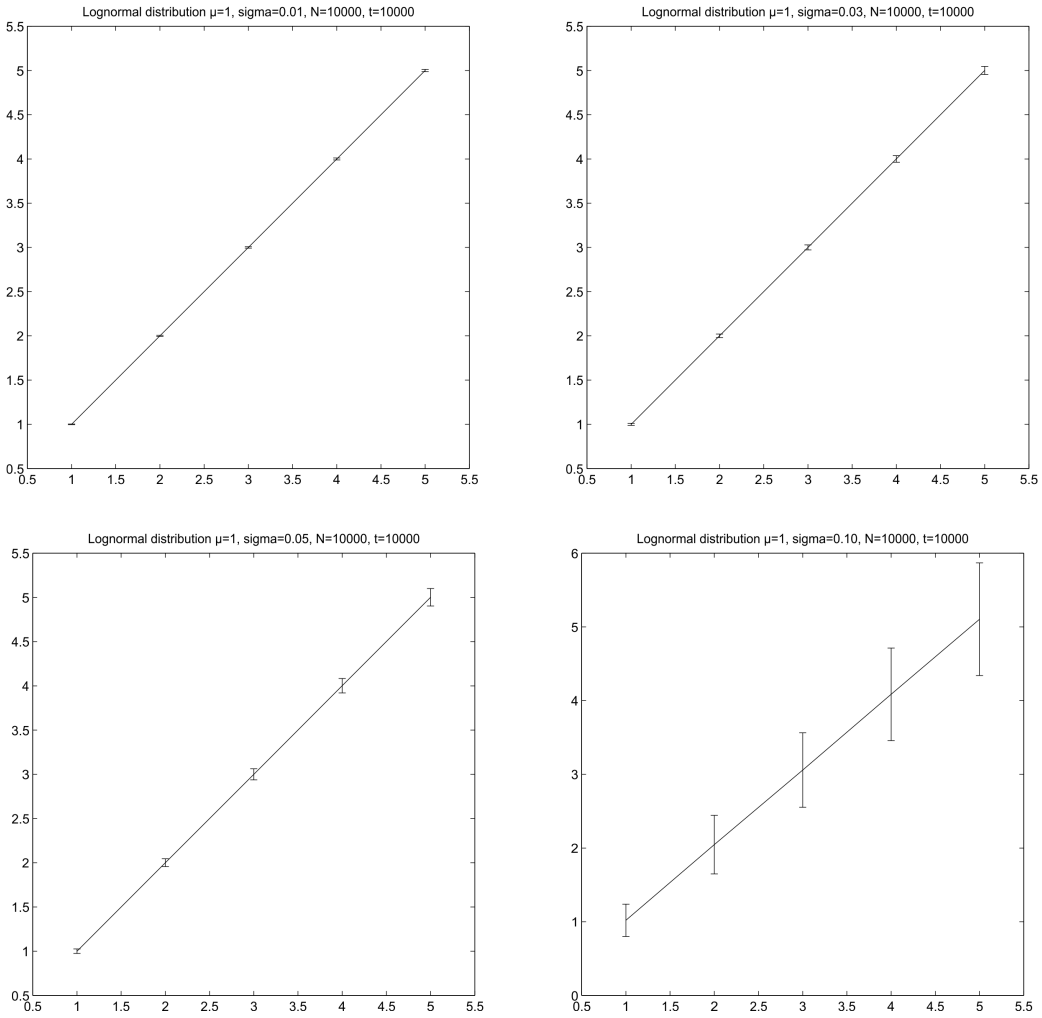

Fig. 6.31: Simulated cross-validation of concentration ratio from spectra with $N = 10000$ molecules. Each of the four figures(up-left, upper-right, lower-left and lower-right) refers to the case with standard deviation of particle size $\sigma = 0.01$, 0.03, 0.05 and 0.10, respectively.

	r=1		r=5	
Molecule number	mean	variance	mean	variance
$N = 10000$	1.0192	0.0479	5.1043	0.5835
$N = 1000$	1.1088	0.3872	5.6035	5.8102
$N = 100$	1.5644	6.7422	7.8419	55.8120

Tab. 6.9: Mean value and variance of selected simulated ratios in the sigma=0.1 case.

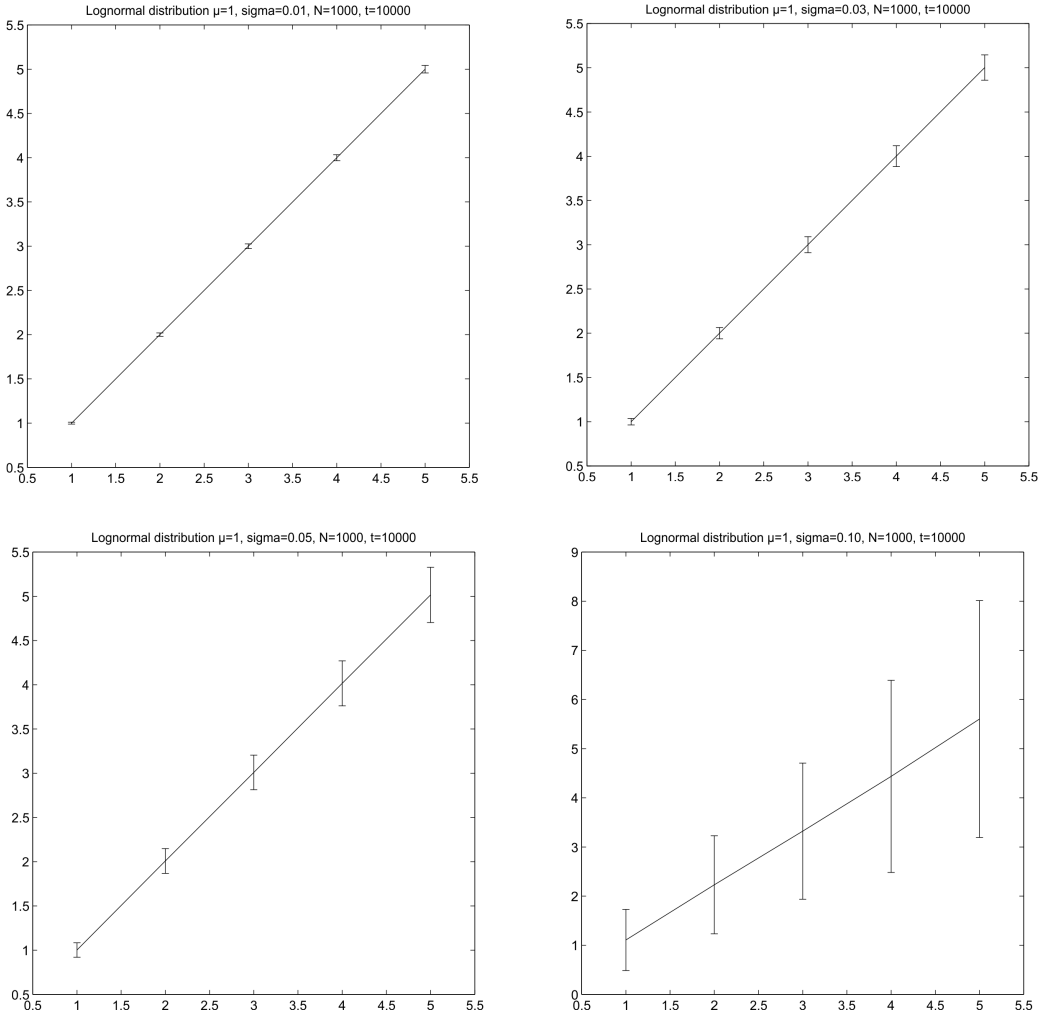

Fig. 6.32: Simulated cross-validation of concentration ratio from spectra with $N = 1000$ molecules. Each of the four figures(up-left, upper-right, lower-left and lower-right) refers to the case with standard deviation of particle size $\sigma = 0.01$, 0.03, 0.05 and 0.10, respectively.

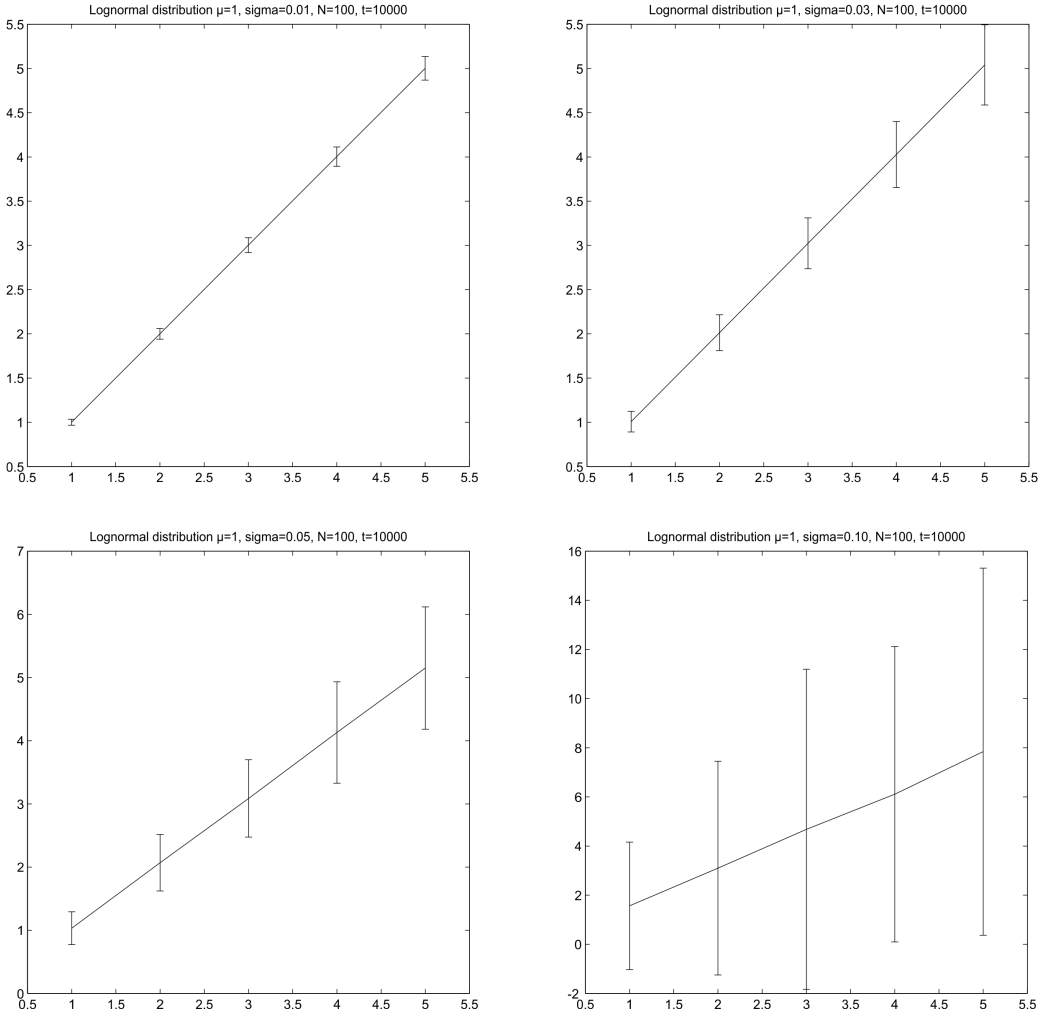

Fig. 6.33: Simulated cross-validation of concentration ratio from spectra with $N = 100$ molecules. Each of the four figures(up-left, upper-right, lower-left and lower-right) refers to the case with standard deviation of particle size $\sigma = 0.01$, 0.03, 0.05 and 0.10, respectively.

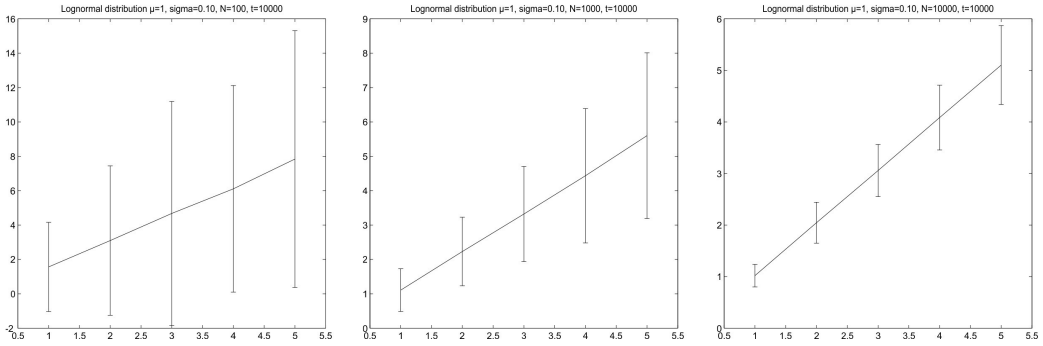

Fig. 6.34: Ratio evaluations with varying number of molecules $N = 100$, 1000 and 10000, respectively. The standard deviation of particle size distribution is sigma=0.1.

The simulated ratio results can also be analyzed roughly but more visibly by a fitting with a Gauss distribution. Their fitting curves and results are shown in Fig.6.35. The upper left, upper right, lower left and lower right figures responses the case with ($N = 100$, $r = 1$), ($N = 10000$, $r = 1$), ($N = 100, r = 5$) and ($N = 10000, r = 5$), respectively. Comparing the symbols to the fitting curves, it is clear that 1. a large number N leads to an increased symmetry of the distribution. 2. a larger ratio leads to a better symmetry of the distribution.

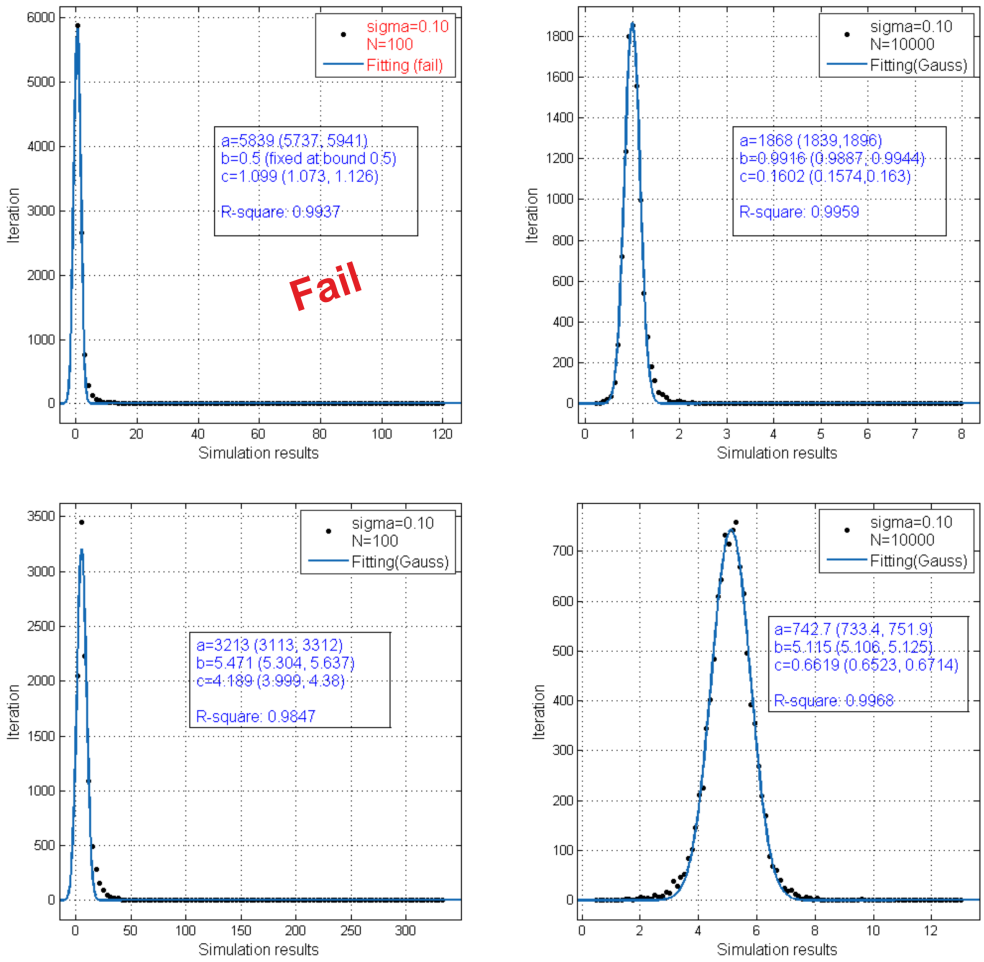

Fig. 6.35: A comparison amount simulation results. The upper left, upper right, lower left and lower right figures responses the case with ($N = 100$, $r = 1$), ($N = 10000$, $r = 1$), ($N = 100, r = 5$) and ($N = 10000, r = 5$), respectively. parameter a ist the un-normalized hight, b is the mean of Gaussian distribution, and c is the standard deviation of the Gaussian distribution. It is obvious that 1. larger number N leads to better symmetry of the distribution, 2. larger ratio leads to better symmetry of the distribution.(The upper left data with $N = 100$ is failed to be fitted as a gaussian distribution, unless b is forced to be constant.)

In fact, for such asymmetric ratio distribution A/B as discussed previously, what we really desire is the *median* of the ratio distribution instead of its *mean*. (For more mathematical details about the median of a distribution we refer to the work of Laplace and R. Fisher. [141]) In short, also a large enough m (with m being the number of spectra on each SERS substrate) is needed, to estimate the median precisely: as sample size increases without bound, the deviation of sample medians goes infinitely to zero. However, recording a huge number of spectra for each substrate is not practically orientated.

Regarding a large enough number N, the distribution of measured ratios will increase in symmetry, and the mean approaches the median. Therefore, the mean of intensity ratio (in a *sample* with *sample size*=m) can be also used to describe the median. In contrast, when N is not large enough, for instance $N < 10000$, there would be a considerable difference between median and mean, and the author suggests here to calculate the median (in a sample with sample size=m) instead of the mean to estimate the ratio. More discussion on the approaches for the estimation of a median can be found in statistics literature, and will not be discussed in detail in this thesis.

In on-chip IDSERS, a large enough number N means that the concentration of the analyte has to be high enough. The author suggests a concentration of at least 10^{-7} mol/L, assuming that in on-chip IDSERS a 10 μL droplet of solution spreads on a SERS substrate across a 1 cm^2 area; the excitation laser is focused onto the center of the drop, and the diameter of the laser spot is 10 μm; in this scenario the coffee ring effect will decrease the amount of molecules in the center of the drop by one or two orders of magnitude.

For single molecule level SERS ($< 10^{-11}$ mol/L), by using a digital protocol technique the limitation could be overcome. [142] Details will not be discussed in this thesis.

As a short summary for the simulation study, the author predicts that for an analyte with a concentration between 10^{-11} and 10^{-7} mol/L, it would be challenging to estimate the ratio of the analyte and its isotopologue (or other internal standards) precisely by using IDSERS, unless a huge number of spectra are collected and median is calculated instead of mean.

6.2.3 Measurement in Practice: An Extreme Example

Except for the fundamental "challenging concentration range", other practical issues would also impact the IDSERS-based ratio estimation process. Here a series of spectra from Rhodamine B and D4-Rhodamine B from double-blind IDSERS measurements would be taken as an extreme example.

In this experiment, a student assistant was asked to prepare five different mixtures of D4-Rhodamine B and Rhodamine B solution (around 10^{-4} M level) using the following ratios 1 : 1, 2 : 1, 3 : 1, 4 : 1, 5 : 1, respectively, and to measure their SERS spectra. The original spectra are shown in Fig. 6.36.

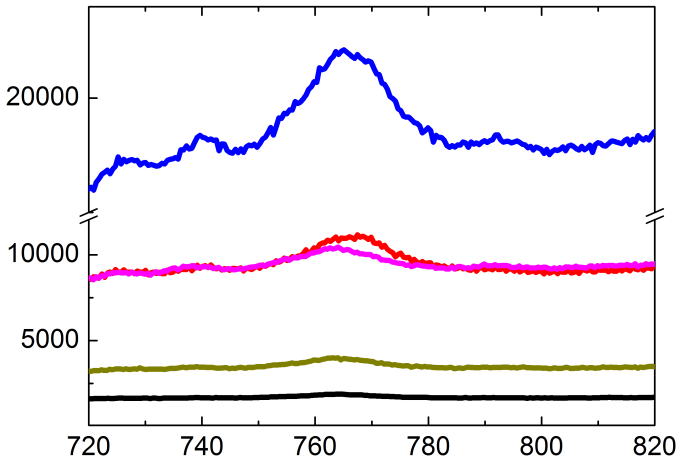

Fig. 6.36: Original IDSERS spectra from the 5 mixtures of D4-Rhodamine B and Rhodamine B solution are measured. Concentration ratio will be then estimated by the data analyzer based on these 5 non-labeled spectra curves.

Then all the five non-labeled spectra are normalized by another person, and redrawn as shown as in Fig. 6.37. Three aspects of the difficulties during the normalization have to be highlighted here: First, an IDSERS spectrum can contain an unexpectedly complex background, which would strongly influence the estimation of the absolutely intensity of each characteristic Raman peak (for this we could consider the *PSSE* discussed in the previous section); Moreover, the spectra plotted in Fig. 6.36 evidence a broadening of the characteristic Raman peaks and a small wavenumber gap between the two peaks hinders an accurate estimation of the peak intensities. Finally, relative noisy spectra also make the estimation rather difficult.

Based on the identical spectrum, choosing background counts slightly different could lead to different reading-out of peak intensity. This is particularly efficient in cases with a large ratio, as shown in Fig. 6.38. On the other hand, when the ratio is close to 1 : 1, fluctuations of the estimation are

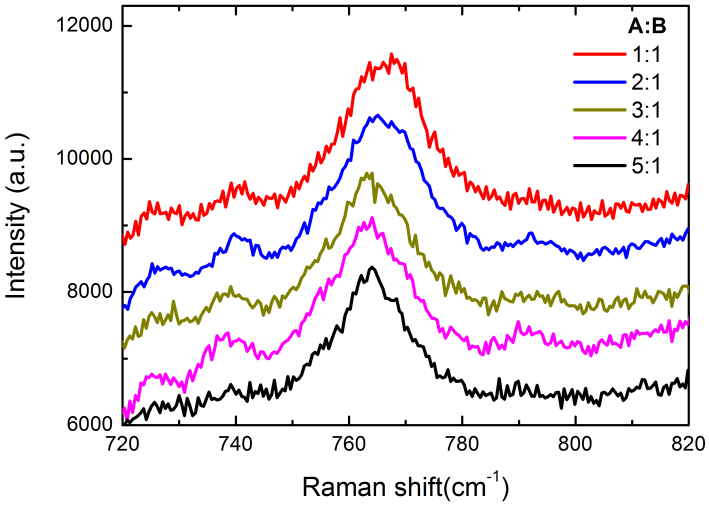

Fig. 6.37: Shifted and normalized IDSERS spectra from the samples.

rather small. Nevertheless, the main point here is that even in such extreme IDSERS experiments as shown in Fig. 6.36, the concentration estimation based on IDSERS spectra is still possible.

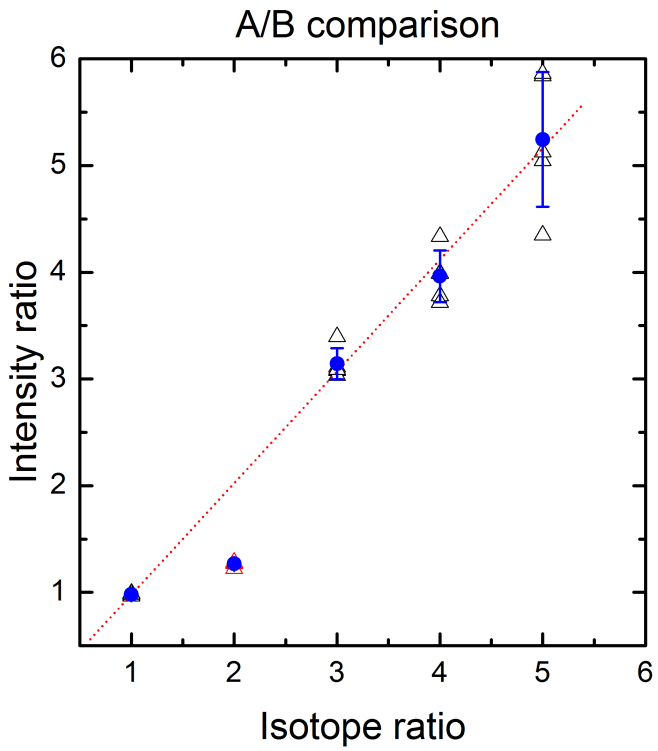

Fig. 6.38: Each mode in a spectrum has been fitted 5 times, and all fitting results are plotted as black triangles. Mean and standard deviation of each group of data are plotted as blue scatters and error bars, respectively. The only mismatch at ratio 2 : 1 should relate to the human error during the mixture preparation.

6.2.4 Conclusion

In this section, an IDSERS technique and the "sub-system" concept for quantifying the IDSERS uncertainty is introduced. According to such a sub-system concept, the IDSERS measurements are modelled and numerically simulated. The relation between intensity ratio of characteristic peaks, which is measured in IDSERS, and the concentration ratio of the analyte to its isotopologue, which is actually the demanded quantity in IDSERS is demonstrated. Moreover, based on the plasmonic properties of SERS substrates, a "challenging concentration range" for IDSERS ($10^{-11} \sim 10^{-7}$mol/L) is predicted by the simulation. In order to overcome this concentration range, it is suggested to collected more spectra and estimate the concentration ratio per median of Raman intensity ratio instead of mean in this range. In the last part the validity of IDSERS is shown by considering an extreme example.

7. SUMMARY

This work aims at the understanding of several charming nano-photonic phenomena related to surface plasmon-molecule interactions.

The first one is strong coupling between surface plasmons and molecular excitons in a periodic nano system. Such strong coupling has been experimentally achieved at room temperature based on Au/AAO nanorod array and Aza-BODIPY system, and theoretically described as a quantum model by quantizing the collective plasmonic behavior in the array. In the future such an intriguing room temperature quantum effect could be of interest in sensors, devices and other techniques.

The second group of questions this thesis answered, is related to quantitative surface enhanced Raman scattering. An approach based on light induced molecular degradations has been demonstrated experimentally and theoretically to quantify the enhancement contribution from chemical mechanisms in SERS. Further questions around IDSERS measurement uncertainty have been discussed for the application purpose, intensity ratio of characteristic peaks, which is to measure in IDSERS, has been modelled as a function of the concentration ratio of the analyte to its isotopologue, which is actually wondered in IDSERS, is demonstrated and numerically studied. A possible challenging measurement range in IDSERS is predicted together with a solution to overcome this challenge.

BIBLIOGRAPHY

[1] Hubert Rauscher, Gert Roebben, Valeria Amenta, Ana Boix Sanfeliu, Luigi Calzolai, Hendrik Emons, Claire Gaillard, Neil Gibson, Thomas Linsinger, Agnieszka Mech, Laia Quiros Pesudo, Kirsten Rasmussen, Juan Riego Sintes, Birgit Sokull-Klüttgen, and Hermann Stamm. Towards a review of the ec recommendation for a definition of the term nanomaterial: Part 1: Compilation of information concerning the experience with the definition. Technical report, Joint Research Centre of the European Commission, Publications Office of the European Union.

[2] Fashui Hong, Juan Zhou, Chao Liu, Fan Yang, Cheng Wu, Lei Zheng, and Ping Yang. Effect of nano-TiO_2 on photochemical reaction of chloroplasts of spinach. *Biological Trace Element Research*, 105(1-3):269–280, 2005.

[3] Chang Hyo Lee, Seung Woo Rhee, and Hyung Wook Choi. Preparation of TiO_2 nanotube/nanoparticle composite particles and their applications in dye-sensitized solar cells. *Nanoscale Research Letters*, 7(1):48, 2012.

[4] Emil Roduner. Size matters: Why nanomaterials are different. *Chemical Society Reviews*, 35(7):583–592, 2006.

[5] A.Boudghene Stambouli and E. Traversa. Solid oxide fuel cells (SOFCs): A review of an environmentally clean and efficient source of energy. *Renewable and Sustainable Energy Reviews*, 6(5):433–455, 2002.

[6] Ming Jiang, Nelson O. Wood, and R. Komanduri. On chemo-mechanical polishing (CMP) of silicon nitride (Si_3N_4) workmaterial with various abrasives. *Wear*, 220(1):59–71, 1998.

[7] E. Yablonovitch. Inhibited spontaneous emission in solid-state physics and electronics. *Physical Review Letters*, 58(20):2059–2062, 1987.

[8] S. John. Strong localization of photons in certain disordered dielectric superlattices. *Physical Review Letters*, 58(23):2486–2489, 1987.

[9] Dennis W. Prather. *Photonic crystals: Theory, applications, and fabrication*. Wiley series in pure and applied optics. Wiley, Hoboken, N.J., 2009.

[10] Nathan G. Greeneltch, Martin G. Blaber, Anne-Isabelle Henry, George C. Schatz, and Van Duyne, Richard. P. Immobilized nanorod assemblies: Fabrication and understanding of large area surface-enhanced Raman spectroscopy substrates. *Analytical Chemistry*, 85(4):2297–2303, 2013.

[11] Shikuan Yang, Xianming Dai, Birgitt Boschitsch Stogin, and Tak-Sing Wong. Ultrasensitive surface-enhanced Raman scattering detection in common fluids. *Proceedings of the National Academy of Sciences*, 113(2):268–273, 2016.

[12] Joel Yuen-Zhou, Semion K. Saikin, Tony Zhu, Mehmet C. Onbasli, Caroline A. Ross, Vladimir Bulovic, and Marc A. Baldo. Plexciton dirac points and topological modes. *Nature Communications*, 7:11783, 2016.

[13] Lamy de la Chapelle, Marc, Nicolas Guillot, Benoît Frémaux, Hong Shen, and Timothée Toury. Novel apolar plasmonic nanostructures with extended optical tunability for sensing applications. *Plasmonics*, 8(2):475–480, 2013.

[14] John D. Joannopoulos, Steven G. Johnson, Joshua N. Winn, and Robert D. Meade. *Photonic Crystals: Molding the Flow of Light (Second Edition)*. Princeton University Press, Princeton, 2008.

[15] Kunimasa Saitoh, Yukihiro Tsuchida, Masanori Koshiba, and Niels Asger Mortensen. Endlessly single-mode holey fibers: The influence of core design. *Optics Express*, 13(26):10833, 2005.

[16] T. A. Birks, J. C. Knight, and P. J. St. Russell. Endlessly single-mode photonic crystal fiber. *Optics Letters*, 22(13):961, 1997.

[17] Stefan Enoch and Nicolas Bonod, editors. *Plasmonics: From basics to advanced topics*, volume v.167 of *Springer Series in Optical Sciences*. Springer, Berlin and New York, 2012.

[18] R. H. Ritchie. Plasma losses by fast electrons in thin films. *Physical Review*, 106(5):874–881, 1957.

[19] Y. J. Huang, W. T. Lu, and S. Sridhar. Nanowire waveguide made from extremely anisotropic metamaterials. *Physical Review A*, 77(6), 2008.

[20] Xinmei Kang, Ximing Guo, Weiwei An, Xingjian Niu, Suhan Li, Zhaoliang Liu, Yue Yang, Na Wang, Qicheng Jiang, Caichuan Yan, Hui Wang, and Qingyuan Zhang. Photothermal therapeutic application of gold nanorods-porphyrin-trastuzumab complexes in HER2-positive breast cancer. *Scientific Reports*, 7:42069, 2017.

[21] Jaeyun Kim, Sungjin Park, Ji Eun Lee, Seung Min Jin, Jung Hee Lee, In Su Lee, Ilseung Yang, Jun-Sung Kim, Seong Keun Kim, Myung-Haing Cho, and Taeghwan Hyeon. Designed fabrication of multifunctional magnetic gold nanoshells and their application to magnetic resonance imaging and photothermal therapy. *Angewandte Chemie*, 118(46):7918–7922, 2006.

[22] Kerry J. Lee, Lauren M. Browning, Prakash D. Nallathamby, and Xiao-Hong Nancy Xu. Study of charge-dependent transport and toxicity of peptide-functionalized silver nanoparticles using zebrafish embryos and single nanoparticle plasmonic spectroscopy. *Chemical Research in Toxicology*, 26(6):904–917, 2013.

[23] Joel Henzie, Min Hyung Lee, and Teri W. Odom. Multiscale patterning of plasmonic metamaterials. *Nature Nanotechnology*, 2(9):549–554, 2007.

[24] F. J. Garcia-Vidal, L. Martín-Moreno, and J. B. Pendry. Surfaces with holes in them: New plasmonic metamaterials. *Journal of Optics A: Pure and Applied Optics*, 7(2):S97–S101, 2005.

[25] Andrea Alù and Nader Engheta. Plasmonic and metamaterial cloaking: Physical mechanisms and potentials. *Journal of Optics A: Pure and Applied Optics*, 10(9):093002, 2008.

[26] Wenshan Cai, Uday K. Chettiar, Alexander V. Kildishev, and Vladimir M. Shalaev. Optical cloaking with metamaterials. *Nature Photonics*, 1(4):224–227, 2007.

[27] I. Bergmair, B. Dastmalchi, M. Bergmair, A. Saeed, W. Hilber, G. Hesser, C. Helgert, E. Pshenay-Severin, T. Pertsch, E. B. Kley, U. Hübner, N. H. Shen, R. Penciu, M. Kafesaki, C. M. Soukoulis, K. Hingerl, M. Muehlberger, and R. Schoeftner. Single and multilayer

metamaterials fabricated by nanoimprint lithography. *Nanotechnology*, 22(32):325301, 2011.

[28] Wei Wu, Zhaoning Yu, Shih-Yuan Wang, R. Stanley Williams, Yongmin Liu, Cheng Sun, Xiang Zhang, Evgenia Kim, Y. Ron Shen, and Nicholas X. Fang. Midinfrared metamaterials fabricated by nanoimprint lithography. *Applied Physics Letters*, 90(6):063107, 2007.

[29] Junhong Zhao, Jian Lin, Xiuhua Li, Guannan Zhao, and Wenjun Zhang. Silver nanoparticles deposited inverse opal film as a highly active and uniform sers substrate. *Applied Surface Science*, 347:514–519, 2015.

[30] B. Hatton, L. Mishchenko, S. Davis, K. H. Sandhage, and J. Aizenberg. Assembly of large-area, highly ordered, crack-free inverse opal films. *Proceedings of the National Academy of Sciences*, 107(23):10354–10359, 2010.

[31] J. Y. Cheng, C. A. Ross, E. L. Thomas, Henry I. Smith, and G. J. Vancso. Fabrication of nanostructures with long-range order using block copolymer lithography. *Applied Physics Letters*, 81(19):3657–3659, 2002.

[32] Chengdu Liang, Kunlun Hong, Georges A. Guiochon, Jimmy W. Mays, and Sheng Dai. Synthesis of a large-scale highly ordered porous carbon film by self-assembly of block copolymers. *Angewandte Chemie (International ed. in English)*, 43(43):5785–5789, 2004.

[33] John C. Hulteen, David A. Treichel, Matthew T. Smith, Michelle L. Duval, Traci R. Jensen, and Van Duyne, Richard P. Nanosphere lithography: Size-tunable silver nanoparticle and surface cluster arrays. *The Journal of Physical Chemistry B*, 103(19):3854–3863, 1999.

[34] Amanda J. Haes, Christy L. Haynes, and Van Duyne, Richard P. Nanosphere lithography: Self-assembled photonic and magnetic materials. *MRS Proceedings*, 636, 2000.

[35] Jong G. Ok, Hong Seok Youn, Moon Kyu Kwak, Kyu-Tae Lee, Young Jae Shin, L. Jay Guo, Anton Greenwald, and Yisi Liu. Continuous and scalable fabrication of flexible metamaterial films via roll-to-roll nanoimprint process for broadband plasmonic infrared filters. *Applied Physics Letters*, 101(22):223102, 2012.

[36] B. Liu, H. Yan, R. Stosch, B. Wolfram, M. Broring, A. Bakin, M. Schilling, and P. Lemmens. Modelling plexcitons of periodic gold nanorod arrays with molecular components. *Nanotechnology*, 28(19):195201, 2017.

[37] Stefan A. Maier. *Plasmonics: Fundamentals and applications*. Springer, New York, 2007.

[38] Hideki Miyazaki and Yoichi Kurokawa. Squeezing visible light waves into a 3-nm-thick and 55-nm-long plasmon cavity. *Physical Review Letters*, 96(9), 2006.

[39] Palash Bharadwaj, Alexandre Bouhelier, and Lukas Novotny. Electrical excitation of surface plasmons. *Physical Review Letters*, 106(22), 2011.

[40] E. Hutter and J. H. Fendler. Exploitation of localized surface plasmon resonance. *Advanced Materials*, 16(19):1685–1706, 2004.

[41] John David Jackson. *Classical electrodynamics*. Wiley, New York, 3rd ed edition, 1999.

[42] Craig F. Bohren and Donald R. Huffman. *Absorption and scattering of light by small particles*. Wiley, New York, 1983.

[43] Uwe Kreibig and Michael Vollmer. *Optical properties of metal clusters*, volume 25. Springer, Berlin and New York, 1995.

[44] Jeff W. Lichtman and José-Angel Conchello. Fluorescence microscopy. *Nature Methods*, 2(12):910–919, 2005.

[45] Timothy W. Collette and Ted L. Williams. The role of raman spectroscopy in the analytical chemistry of potable water. *Journal of Environmental Monitoring*, 4(1):27–34, 2002.

[46] Katrin Kneipp, Yang Wang, Harald Kneipp, Lev T. Perelman, and Irving Itzkan. Single molecule detection using surface-enhanced Raman scattering (SERS). *Physical Review Letters*, 78(9):1667–1670, 1997.

[47] S. N. Terekhov, P. Mojzes, S. M. Kachan, N. I. Mukhurov, S. P. Zhvavyi, A. Yu. Panarin, I. A. Khodasevich, V. A. Orlovich, A. Thorel, F. Grillon, and P.-Y. Turpin. A comparative study of surface-enhanced Raman scattering from silver-coated anodic aluminum oxide and porous silicon. *Journal of Raman Spectroscopy*, 42(1):12–20, 2011.

[48] Graeme McNay, David Eustace, W. Ewen Smith, Karen Faulds, and Duncan Graham. Surface-enhanced Raman scattering (SERS) and surface-enhanced resonance Raman scattering (SERRS): A review of applications. *Applied Spectroscopy*, 65(8):825–837, 2011.

[49] D. Cunningham, R. E. Littleford, W. E. Smith, P. J. Lundahl, I. Khan, D. W. McComb, D. Graham, and N. Laforest. Practical control of SERRS enhancement. *Faraday Discussions*, 132:135, 2006.

[50] Edward D. Palik, Edward J. Prucha, and Ivan P. Kaminow, editors. *Handbook of optical constants of solids*. Academic Press, New York, 1985-98.

[51] Dirk P. Kroese, Tim Brereton, Thomas Taimre, and Zdravko I. Botev. Why the monte carlo method is so important today. *Wiley Interdisciplinary Reviews: Computational Statistics*, 6(6):386–392, 2014.

[52] J. C. Spall. Feature - estimation via markov chain monte carlo. *IEEE Control Systems Magazine*, 23(2):34–45, 2003.

[53] Oliver C. Wells. *Scanning electron microscopy*. McGraw-Hill, New York, 1974.

[54] Weili Zhou and Zhong Lin Wang. *Scanning microscopy for nanotechnology: Techniques and applications*. Springer, New York and London, 2007.

[55] Woo Lee, Ran Ji, Ulrich Gösele, and Kornelius Nielsch. Fast fabrication of long-range ordered porous alumina membranes by hard anodization. *Nature Materials*, 5(9):741–747, 2006.

[56] Junius D. Edwards and Fred Keller. Formation of anodic coatings on aluminum. *Transactions of The Electrochemical Society*, 79(1):135, 1941.

[57] F. Keller, M. S. Hunter, and D. L. Robinson. Structural features of oxide coatings on aluminum. *Journal of The Electrochemical Society*, 100(9):411, 1953.

[58] H. Masuda and K. Fukuda. Ordered metal nanohole arrays made by a two-step replication of honeycomb structures of anodic alumina. *Science*, 268(5216):1466–1468, 1995.

[59] Aijun A. Wang, Joun Lee, Gabriela Jenikova, Ashok Mulchandani, Nosang V. Myung, and Wilfred Chen. Controlled assembly of multi-segment nanowires by histidine-tagged peptides. *Nanotechnology*, 17(14):3375–3379, 2006.

[60] Li-Feng Liu, Wei-Ya Zhou, Si-Shen Xie, Ole Albrecht, and Kornelius Nielsch. Microstructure and temperature-dependent magnetic properties of Co/Pt multilayered nanowires. *Chemical Physics Letters*, 466(4-6):165–169, 2008.

[61] Zixue Su and Wuzong Zhou. Formation mechanism of porous anodic aluminium and titanium oxides. *Advanced Materials*, 20(19):3663–3667, 2008.

[62] G. E. Thompson and G. C. Wood. Porous anodic film formation on aluminium. *NATURE*, 290(5803):230–232, 1981.

[63] A. Mozalev, A. Poznyak, I. Mozaleva, and A. W. Hassel. The voltage–time behaviour for porous anodizing of aluminium in a fluoride-containing oxalic acid electrolyte. *Electrochemistry Communications*, 3(6):299–305, 2001.

[64] S. Shingubara, K. Morimoto, H. Sakaue, and T. Takahagi. Self-organization of a porous alumina nanohole array using a sulfuric/oxalic acid mixture as electrolyte. *Electrochemical and Solid-State Letters*, 7(3):E15, 2004.

[65] Yufei Jia, Haihui Zhou, Peng Luo, Shenglian Luo, Jinhua Chen, and Yafei Kuang. Preparation and characteristics of well-aligned macroporous films on aluminum by high voltage anodization in mixed acid. *Surface and Coatings Technology*, 201(3-4):513–518, 2006.

[66] Hongdan Yan. *Preparation and optical characterization of nanoporous templates as a basis for nanocontact arrays.* PhD thesis, Technische Universität Carolo-Wilhelmina zu Braunschweig, 2013.

[67] Hongdan Yan. High-density array of au nanowires coupled by plasmon modes. *Acta Phys. Sin.*, 61, 2012.

[68] Hongdan Yan. Personal communication, 2014.

[69] A. A. Mistonov, N. A. Grigoryeva, A. V. Chumakova, H. Eckerlebe, N. A. Sapoletova, K. S. Napolskii, A. A. Eliseev, D. Menzel, and S. V. Grigoriev. Three-dimensional artificial spin ice in nanostructured co on an inverse opal-like lattice. *Physical Review B*, 87(22), 2013.

[70] Yi-Jui Huang, Chun-Han Lai, Pu-Wei Wu, and Li-Yin Chen. Ni inverse opals for water electrolysis in an alkaline electrolyte. *Journal of The Electrochemical Society*, 157(3):P18, 2010.

[71] A. L. Rogach, N. A. Kotov, D. S. Koktysh, J. W. Ostrander, and G. A. Ragoisha. Electrophoretic deposition of latex-based 3D colloidal photonic crystals: A technique for rapid production of high-quality opals. *Chemistry of Materials*, 12(9):2721–2726, 2000.

[72] Zhong-Ze Gu, Akira Fujishima, and Osamu Sato. Fabrication of high-quality opal films with controllable thickness. *Chemistry of Materials*, 14(2):760–765, 2002.

[73] Orlin D. Velev and Abraham M. Lenhoff. Colloidal crystals as templates for porous materials. *Current Opinion in Colloid & Interface Science*, 5(1-2):56–63, 2000.

[74] D. J. Norris, E. G. Arlinghaus, L. Meng, R. Heiny, and L. E. Scriven. Opaline photonic crystals: How does self-assembly work? *Advanced Materials*, 16(16):1393–1399, 2004.

[75] Catherine M. Cotell. *Surface engineering*, volume / prepared under the direction of the ASM International Handbook Committee ; Vol. 5 of *ASM handbook*. ASM International, Materials Park, Ohio, [10. ed.], 4. print edition, 2007.

[76] Nche T. Fofang, Tae-Ho Park, Oara Neumann, Nikolay A. Mirin, Peter Nordlander, and Naomi J. Halas. Plexcitonic nanoparticles: Plasmon−exciton coupling in nanoshell−J-aggregate complexes. *Nano Letters*, 8(10):3481–3487, 2008.

[77] Salvatore Savasta, Rosalba Saija, Alessandro Ridolfo, Omar Di Stefano, Paolo Denti, and Ferdinando Borghese. Nanopolaritons: Vacuum rabi splitting with a single quantum dot in the center of a dimer nanoantenna. *ACS Nano*, 4(11):6369–6376, 2010.

[78] Nche T. Fofang, Nathaniel K. Grady, Zhiyuan Fan, Alexander O. Govorov, and Naomi J. Halas. Plexciton dynamics: Exciton−plasmon coupling in a J-aggregate−Au nanoshell complex provides a mechanism for nonlinearity. *Nano Letters*, 11(4):1556–1560, 2011.

[79] J. Bellessa, C. Symonds, K. Vynck, A. Lemaitre, A. Brioude, L. Beaur, J. C. Plenet, P. Viste, D. Felbacq, E. Cambril, and P. Valvin. Giant

rabi splitting between localized mixed plasmon-exciton states in a two-dimensional array of nanosize metallic disks in an organic semiconductor. *Physical Review B*, 80(3), 2009.

[80] Olalla Pérez-González, Javier Aizpurua, and Nerea Zabala. Optical transport and sensing in plexcitonic nanocavities. *Optics Express*, 21(13):15847, 2013.

[81] Xiaohua Wu, Stephen K. Gray, and Matthew Pelton. Quantum-dot-induced transparency in a nanoscale plasmonic resonator. *Optics Express*, 18(23):23633, 2010.

[82] Bob Y. Zheng, Hangqi Zhao, Alejandro Manjavacas, Michael McClain, Peter Nordlander, and Naomi J. Halas. Distinguishing between plasmon-induced and photoexcited carriers in a device geometry. *Nature Communications*, 6:7797, 2015.

[83] Andres D. Neira, Nicolas Olivier, Mazhar E. Nasir, Wayne Dickson, Gregory A. Wurtz, and Anatoly V. Zayats. Eliminating material constraints for nonlinearity with plasmonic metamaterials. *Nature Communications*, 6:7757, 2015.

[84] Jeffrey M. McMahon, Stephen K. Gray, and George C. Schatz. Optical properties of nanowire dimers with a spatially nonlocal dielectric function. *Nano Letters*, 10(9):3473–3481, 2010.

[85] Olga Spirina Jenkins and Hunt, Katharine L. C. Nonlocal dielectric functions on the nanoscale: Screened forces from unscreened potentials. *The Journal of Chemical Physics*, 119(16):8250, 2003.

[86] A. Manjavacas, Abajo, F. J. García de, and P. Nordlander. Quantum plexcitonics: Strongly interacting plasmons and excitons. *Nano Letters*, 11(6):2318–2323, 2011.

[87] M. S. Tame, K. R. McEnery, Ş. K. Özdemir, J. Lee, S. A. Maier, and M. S. Kim. Quantum plasmonics. *Nature Physics*, 9(6):329–340, 2013.

[88] A. Ridolfo, O. Di Stefano, N. Fina, R. Saija, and S. Savasta. Quantum plasmonics with quantum dot-metal nanoparticle molecules: Influence of the Fano effect on photon statistics. *Physical Review Letters*, 105(26), 2010.

[89] M. S. Tame, C. Lee, J. Lee, D. Ballester, M. Paternostro, A. V. Zayats, and M. S. Kim. Single-photon excitation of surface plasmon polaritons. *Physical Review Letters*, 101(19), 2008.

[90] D. C. Marinica, H. Lourenço-Martins, J. Aizpurua, and A. G. Borisov. Plexciton quenching by resonant electron transfer from quantum emitter to metallic nanoantenna. *Nano Letters*, 13(12):5972–5978, 2013.

[91] Ruben Esteban, Andrei G. Borisov, Peter Nordlander, and Javier Aizpurua. Bridging quantum and classical plasmonics with a quantum-corrected model. *Nature Communications*, 3:825, 2012.

[92] P. Törmä and W. L. Barnes. Strong coupling between surface plasmon polaritons and emitters: a review. *Reports on Progress in Physics*, 78(1):013901, 2015.

[93] P. R. Evans, Gregory A. Wurtz, R. Atkinson, W. Hendren, D. O'Connor, W. Dickson, R. J. Pollard, and A. V. Zayats. Plasmonic core/shell nanorod arrays: Subattoliter controlled geometry and tunable optical properties. *Journal of Physical Chemistry C*, 111(34):12522–12527, 2007.

[94] Z. Wang, Y.-K. Su, and H.-L. Li. Afm study of gold nanowire array electrodeposited within anodic aluminum oxide template. *Applied Physics A: Materials Science and Processing*, 74(4):563–565, 2002.

[95] Bin Wu, Andreas Heidelberg, and John J. Boland. Mechanical properties of ultrahigh-strength gold nanowires. *Nature Materials*, 4(7):525–529, 2005.

[96] Gregory A. Wurtz, Paul R. Evans, William Hendren, Ronald Atkinson, Wayne Dickson, Robert J. Pollard, Anatoly V. Zayats, William Harrison, and Christopher Bower. Molecular plasmonics with tunable exciton−plasmon coupling strength in J-aggregate hybridized Au nanorod assemblies. *Nano Letters*, 7(5):1297–1303, 2007.

[97] Xiaohua Huang, Ivan H. El-Sayed, Wei Qian, and Mostafa A. El-Sayed. Cancer cell imaging and photothermal therapy in the near-infrared region by using gold nanorods. *Journal of the American Chemical Society*, 128(6):2115–2120, 2006.

[98] Nikhil R. Jana, Latha Gearheart, and Catherine J. Murphy. Wet chemical synthesis of high aspect ratio cylindrical gold nanorods. *The Journal of Physical Chemistry B*, 105(19):4065–4067, 2001.

[99] Hongdan Yan, Peter Lemmens, Dirk Wulferding, Jianmin Shi, Klaus Dieter Becker, Chengtian Lin, Aidin Lak, and Meinhard Schilling. Tailoring defect structure and optical absorption of porous

anodic aluminum oxide membranes. *Materials Chemistry and Physics*, 135(1):206–211, 2012.

[100] Prashant K. Jain, Susie Eustis, and Mostafa A. El-Sayed. Plasmon coupling in nanorod assemblies: Optical absorption, discrete dipole approximation simulation, and exciton-coupling model. *The Journal of Physical Chemistry B*, 110(37):18243–18253, 2006.

[101] Gregory A. Wurtz and W. Dickson. Guided plasmonic modes in nanorod assemblies: strong electromagnetic coupling regime. *Optics Express*, 16(10):7460–7470, 2008.

[102] René Kullock, William R. Hendren, Andreas Hille, Stefan Grafström, Paul R. Evans, Robert J. Pollard, Ron Atkinson, and Lukas M. Eng. Polarization conversion through collective surface plasmons in metallic nanorod arrays. *Optics Express*, 16(26):21671, 2008.

[103] Alexander B. Nepomnyashchii, Martin Bröring, Johannes Ahrens, and Allen J. Bard. Synthesis, photophysical, electrochemical, and electrogenerated chemiluminescence studies. Multiple sequential electron transfers in bodipy monomers, dimers, trimers, and polymer. *Journal of the American Chemical Society*, 133(22):8633–8645, 2011.

[104] Tomasz J. Antosiewicz, S. Peter Apell, and Timur Shegai. Plasmon–exciton interactions in a core–shell geometry: From enhanced absorption to strong coupling. *ACS Photonics*, 1(5):454–463, 2014.

[105] J. Bellessa, C. Bonnand, J. C. Plenet, and J. Mugnier. Strong coupling between surface plasmons and excitons in an organic semiconductor. *Physical Review Letters*, 93(3), 2004.

[106] Gülis Zengin, Martin Wersäll, Sara Nilsson, Tomasz J. Antosiewicz, Mikael Käll, and Timur Shegai. Realizing strong light-matter interactions between single-nanoparticle plasmons and molecular excitons at ambient conditions. *Physical Review Letters*, 114(15), 2015.

[107] Martin Moskovits. Persistent misconceptions regarding sers. *Physical Chemistry Chemical Physics*, 15(15):5301, 2013.

[108] Andreas Otto. The 'chemical' (electronic) contribution to surface-enhanced raman scattering. *Journal of Raman Spectroscopy*, 36(6-7):497–509, 2005.

[109] J. A. Porto, L. Martín-Moreno, and F. J. García-Vidal. Optical bistability in subwavelength slit apertures containing nonlinear media. *Physical Review B*, 70(8):15, 2004.

[110] Liangbao Yang, Pan Li, Honglin Liu, Xianghu Tang, and Jinhuai Liu. A dynamic surface enhanced Raman spectroscopy method for ultrasensitive detection: From the wet state to the dry state. *Chemical Society Reviews*, 44(10):2837–2848, 2015.

[111] R. F. Kubin and A. N. Fletcher. Fluorescence quantum yields of some rhodamine dyes. *Journal of Luminescence*, 27(4):455–462, 1982.

[112] Douglas Magde, Roger Wong, and Paul G. Seybold. Fluorescence quantum yields and their relation to lifetimes of rhodamine 6G and fluorescein in nine solvents: Improved absolute standards for quantum yields. *Photochemistry and Photobiology*, 75(4):327–334, 2002.

[113] M. Fischer and J. Georges. Fluorescence quantum yield of rhodamine 6G in ethanol as a function of concentration using thermal lens spectrometry. *Chemical Physics Letters*, 260(1-2):115–118, 1996.

[114] Tamitake Itoh, Kenichi Yoshida, Vasudevanpillai Biju, Yasuo Kikkawa, Mitsuru Ishikawa, and Yukihiro Ozaki. Second enhancement in surface-enhanced resonance Raman scattering revealed by an analysis of anti-Stokes and Stokes Raman spectra. *Physical Review B*, 76(8):83, 2007.

[115] Kai-Qiang Lin, Jun Yi, Jin-Hui Zhong, Shu Hu, Bi-Ju Liu, Jun-Yang Liu, Cheng Zong, Zhi-Chao Lei, Xiang Wang, Javier Aizpurua, Rubén Esteban, and Bin Ren. Plasmonic photoluminescence for recovering native chemical information from surface-enhanced Raman scattering. *Nature Communications*, 8:14891, 2017.

[116] Chaofan Sui, Kaige Wang, Shuang Wang, Junying Ren, Xiaohong Bai, and Jintao Bai. Sers activity with tenfold detection limit optimization on a type of nanoporous AAO-based complex multilayer substrate. *Nanoscale*, 8(11):5920–5927, 2016.

[117] Jianing Chen, Thomas Mårtensson, Kimberly A. Dick, Knut Deppert, H. Q. Xu, Lars Samuelson, and Hongxing Xu. Surface-enhanced raman scattering of rhodamine 6G on nanowire arrays decorated with gold nanoparticles. *Nanotechnology*, 19(27):275712, 2008.

[118] Xiu Liang, BenLiang Liang, Zhenghui Pan, Xiufeng Lang, Yuegang Zhang, Guangsheng Wang, Penggang Yin, and Lin Guo. Tuning plasmonic and chemical enhancement for sers detection on graphene-based Au hybrids. *Nanoscale*, 7(47):20188–20196, 2015.

[119] Elizabeth Kohr, Buddini I. Karawdeniya, Jason R. Dwyer, Anju Gupta, and William B. Euler. A comparison of sers and mef of rhodamine 6g on a gold substrate. *Physical Chemistry Chemical Physics : PCCP*, 19(39):27074–27080, 2017.

[120] Alan Campion and Patanjali Kambhampati. Surface-enhanced raman scattering. *Chemical Society Reviews*, 27(4):241, 1998.

[121] A. T. Zayak, Y. S. Hu, H. Choo, J. Bokor, S. Cabrini, P. J. Schuck, and J. B. Neaton. Chemical raman enhancement of organic adsorbates on metal surfaces. *Physical Review Letters*, 106(8), 2011.

[122] Lasse Jensen, Christine M. Aikens, and George C. Schatz. Electronic structure methods for studying surface-enhanced raman scattering. *Chemical Society Reviews*, 37(5):1061–1073, 2008.

[123] Angela Punzi, Gaëlle Martin-Gassin, Jakob Grilj, and Eric Vauthey. Effect of salt on the excited-state dynamics of malachite green in bulk aqueous solutions and at air/water interfaces: A femtosecond transient absorption and surface second harmonic generation study †. *The Journal of Physical Chemistry C*, 113(27):11822–11829, 2009.

[124] S. Schneider, G. Brehm, and P. Freunscht. Comparison of surface-enhanced raman and hyper-raman spectra of the triphenylmethane dyes crystal violet and malachite green. *Physica Status Solidi (b)*, 189(1):37–42, 1995.

[125] C. Berberidou, I. Poulios, N. P. Xekoukoulotakis, and D. Mantzavinos. Sonolytic, photocatalytic and sonophotocatalytic degradation of malachite green in aqueous solutions. *Applied Catalysis B: Environmental*, 74(1-2):63–72, 2007.

[126] Yue Jin, Pinyi Ma, Fanghui Liang, Dejiang Gao, and Xinghua Wang. Determination of malachite green in environmental water using cloud point extraction coupled with surface-enhanced raman scattering. *Analytical Methods*, 5(20):5609, 2013.

[127] Musundi B. Wabuyele and Tuan Vo-Dinh. Detection of human immunodeficiency virus type 1 DNA sequence using plasmonics nanoprobes. *Analytical Chemistry*, 77(23):7810–7815, 2005.

[128] Callum J. McHugh, Ruth Keir, Duncan Graham, and W. Ewen Smith. Selective functionalisation of TNT for sensitive detection by SERRS. *Chemical Communications*, (6):580–581, 2002.

[129] Barry D. Moore, Lorna Stevenson, Alan Watt, Sabine Flitsch, Nicolas J. Turner, Chris Cassidy, and Duncan Graham. Rapid and ultrasensitive determination of enzyme activities using surface-enhanced resonance Raman scattering. *Nature Biotechnology*, 22(9):1133–1138, 2004.

[130] Ying Fang, Nak-Hyun Seong, and Dana D. Dlott. Measurement of the distribution of site enhancements in surface-enhanced Raman scattering. *Science (New York, N.Y.)*, 321(5887):388–392, 2008.

[131] Jeffrey H. Giles, Daniel A. Gilmore, and M. Bonner Denton. Quantitative analysis using Raman spectroscopy without spectral standardization. *Journal of Raman Spectroscopy*, 30(9):767–771, 1999.

[132] Weigao Xu, Xi Ling, Jiaqi Xiao, Mildred S. Dresselhaus, Jing Kong, Hongxing Xu, Zhongfan Liu, and Jin Zhang. Surface enhanced Raman spectroscopy on a flat graphene surface. *Proceedings of the National Academy of Sciences of the United States of America*, 109(24):9281–9286, 2012.

[133] Shirshendu K. Deb, Brandon Davis, Giselle M. Knudsen, Ravindra Gudihal, Dor Ben-Amotz, and V. Jo Davisson. Detection and relative quantification of proteins by surface enhanced Raman using isotopic labels. *Journal of the American Chemical Society*, 130(30):9624–9625, 2008.

[134] Sabine Zakel, Olaf Rienitz, Bernd Güttler, and Rainer Stosch. Double isotope dilution surface-enhanced Raman scattering as a reference procedure for the quantification of biomarkers in human serum. *The Analyst*, 136(19):3956, 2011.

[135] Sabine Zakel, Stefan Wundrack, Gavin O'Connor, Bernd Güttler, and Rainer Stosch. Validation of isotope dilution surface-enhanced Raman scattering (idsers) as a higher order reference method for clinical measurands employing international comparison schemes. *Journal of Raman Spectroscopy*, 44(9):1246–1252, 2013.

[136] D. V. Hinkley. On the ratio of two correlated normal random variables. *Biometrika*, 56(3):635, 1969.

[137] George Marsaglia. Ratios of normal variables. *Journal of Statistical Software*, 16(4), 2006.

[138] Ulrike von Luxburg and Volker H. Franz. A geometric approach to confidence sets for ratios: Fieller's theorem, generalizations and bootstrap. *Statistica Sinica*, 19:1095–1117, 2009.

[139] International Organization for Standardization. ISO9004-4:1993 Quality management and quality system elements - Guidelines for quality improvement, 1993.

[140] B. Hampel, B. Liu, F. Nording, J. Ostermann, P. Struszewski, J. Langfahl-Klabes, M. Bieler, H. Bosse, B. Güttler, P. Lemmens, M. Schilling, and R. Tutsch. Approach to determine measurement uncertainty in complex nanosystems with multiparametric dependencies and multivariate output quantities. *Measurement Science and Technology*, 29(3):035003, 2018.

[141] Stephen M. Stigler. Studies in the history of probability and statistics. xxxii: Laplace, Fisher and the discovery of the concept of sufficiency. *Biometrika*, 60(3):439, 1973.

[142] Carlos Diego L. de Albuquerque, Regivaldo G. Sobral-Filho, Ronei J. Poppi, and Alexandre G. Brolo. Digital protocol for chemical analysis at ultralow concentrations by surface-enhanced Raman scattering. *Analytical Chemistry*, 90(2):1248–1254, 2018.

APPENDIXES

Appendix A ..... MATLAB code of Monte Carlo Method for IDSERS

A: MATLAB code of Monte Carlo Method for IDSERS

```
function [ ] = simul( )

% parameters
%N: Number of molecules
%t: times of experiment
%%%%N*t should be smaller than 10E11, otherwise '
   out of memory'.
%d: type of distribution
    %----------------------type of distribution----------
    % parameter d
    % d=1; uniform
    % d=2; normal
    % d=3; Rayleigh(B=delta=0.25)
    % d=4; Rayleigh(B=delta=1)
    % d=5; lognormal :lognrnd(_003 =
        -0.011419782732928, sigma_003 =
        0.7205157923254 07);
    % d=6; lognormal :lognrnd(_010 =
        -0.120493034780926, sigma_010 =
        2.428459686013845);
    % d=7; lognormal :lognrnd(_005 =
        -0.029252572864584, sigma_005 =
        1.203145878901769);
    % d=8; lognormal :lognrnd(_001 =
        -9.724175829426487e-04, sigma_001 =
        0.239951931712128);
    %-------------------------------------------------------
N=10000; %Number of molecules
```

```
ra=5; %
t=10000; %times of experiment
D=8; %distribution%
% M=10^6;%EF_max
%max=2000;
%————————————————————main body————————————————————
while ra
    k=D; %distribution total number
    while k
        switch D+1-k
            case 1
                r1=rand(N.*ra,t);
                b1=sum(r1);
                r2=rand(N,t);
                b2=sum(r2);
                brad=b1./b2;
                m1=mean(brad,2);
                var1=var(brad);
                figure;[nele1,ncenter1]=hist(brad
                    ,50);
                scatter(ncenter1,nele1);
                xlim([ra.*0.85, ra.*1.15]);
            case 2
                r1=normrnd(0.5,0.3,N.*ra,t);
                b1=sum(r1);
                r2=normrnd(0.5,0.3,N,t);
                b2=sum(r2);
                bnor=b1./b2;
                m2=mean(bnor,2);
                var2=var(bnor);
                figure;[nele2,ncenter2]=hist(bnor,[
                    ra.*0.85:ra.*0.005:ra.*1.15]);
                scatter(ncenter2,nele2);
                xlim([ra.*0.85, ra.*1.15]);

            case 3
                r1=raylrnd(0.25,N.*ra,t);
                b1=sum(r1);
                r2=raylrnd(0.25,N,t);
                b2=sum(r2);
                bray=b1./b2;
```

```
        m3=mean(bray,2);
        var3=var(bray);
        figure;[nele3,ncenter3]=hist(bray,[
            ra.*0.85:ra.*0.005:ra.*1.15]);
        scatter(ncenter3,nele3);
        xlim([ra.*0.85, ra.*1.15]);
    case 4
        r1=raylrnd(1,N.*ra,t);
        b1=sum(r1);
        r2=raylrnd(1,N,t);
        b2=sum(r2);
        bray=b1./b2;
        m4=mean(bray,2);
        var4=var(bray);
        figure;[nele4,ncenter4]=hist(bray,[
            ra.*0.85:ra.*0.005:ra.*1.15]);
        scatter(ncenter4,nele4);
        xlim([ra.*0.85, ra.*1.15]);
    case 5
        r1=lognrnd
            (-0.011419782732928,0.720515792325407,
            N.*ra,t);
        b1=sum(r1);
        r2=lognrnd
            (-0.011419782732928,0.720515792325407,
            N,t);
        b2=sum(r2);
        blog=b1./b2;
        m5=mean(blog,2);
        var5=var(blog);
        figure;[nele5,ncenter5]=hist(blog
            ,100);
        scatter(ncenter5,nele5);
        %xlim([ra.*0.85, ra.*1.15]);
     case 6
        r1=lognrnd
            (-0.120493034780926,2.428459686013845,
            N.*ra,t);
        b1=sum(r1);
        r2=lognrnd
            (-0.120493034780926,2.428459686013845,
```

```
                    N,t);
                b2=sum(r2);
                blog=b1./b2;
                m6=mean(blog,2);
                var6=var(blog);
                figure;[nele6,ncenter6]=hist(blog
                    ,100);
                scatter(ncenter6,nele6);
            case 7
                r1=lognrnd
                    (-0.029252572864584,1.203145878901769,
                    N.*ra,t);
                b1=sum(r1);
                r2=lognrnd
                    (-0.029252572864584,1.203145878901769,
                    N,t);
                b2=sum(r2);
                blog=b1./b2;
                m7=mean(blog,2);
                var7=var(blog);
                figure;[nele7,ncenter7]=hist(blog
                    ,100);
                scatter(ncenter7,nele7);
            case 8
                r1=lognrnd(-9.724175829426487e
                    -04,0.239951931712128,N.*ra,t);
                b1=sum(r1);
                r2=lognrnd(-9.724175829426487e
                    -04,0.239951931712128,N,t);
                b2=sum(r2);
                blog=b1./b2;
                m8=mean(blog,2);
                var8=var(blog);
                figure;[nele8,ncenter8]=hist(blog
                    ,100);
                scatter(ncenter8,nele8);
        end
        k=k-1;
    end
    foldernm = ['molecule_' num2str(N) 'times_'
        num2str(t)];
```

```
        mkdir(foldernm);
        filenm = ['molecule_' num2str(N) 'times_'
            num2str(t) '\ratio_' num2str(ra) 'molecule_'
             num2str(N) 'times_' num2str(t) '.mat'];
        save( filenm,'m1','var1','m2','var2','m3','var3
            ','m4','var4','m5','var5','m6','var6','m7','
            var7','m8','var8','nele1','ncenter1','nele2'
            ,'ncenter2','nele3','ncenter3','nele4','
            ncenter4','nele5','ncenter5','nele6','
            ncenter6','nele7','ncenter7','nele8','
            ncenter8');
        ra=ra-1;
    end
    end
```

ACKNOWLEDGEMENTS

My work at the Institute for Condensed Matter Physics (Institut für Physik der Kondensierten Materie, IPKM), TU Braunschweig has benefitted from many collaborations, important discussions and a friendly environment.

Firstly, I would like to express my sincere gratitude to my first advisor Prof. Peter Lemmens for the continuous support of my research and related projects. He was always open to new scientific ideas and supported my trial-and-error both experimentally and theoretically. His guidance helped me in all the time of research and writing of this thesis.

My sincere thanks also goes to Dr. Rainer Stosch, my second advisor in Braunschweig International Graduate School of Metrology for all his kind discussion, insightful advice and support in writing and experiments.

Besides my advisors, I would like to thank the rest of my thesis committee: Prof. Patrik Recher, Prof. Meinhard Schilling for their constructive comments and encouragement, but also for the challenging questions which helped me to widen my research from various perspectives.

In addition, I would like to thank Prof. Samir Pal, S. N. Bose National Centre for Basic Sciences for our comprehensive discussions for in the years, and to thank Prof. Bernd Güttler for his help and support.

I thank my current and past fellows: Dr. Hongdan Yan, Dr. Azat Sharafeev, Savutjan Sidik, Silvia Müllner, and Dr. Dirk Wulferding for accommodating me and creating an excellent atmosphere for research and learning.

Valuable advice in my research and study I have had many helpful discussions with our guests Dr. Vladimir Gnezdilov, Prof. Yurii Pashkevich, and Prof. Kwang-Yong Choi. I have also benefited from Dr. Dirk Menzel, Prof. Fred Jochen Litterst, Prof. Stefan Süllow, Axel Paschke for the last four years. I am also grateful to the help from our workshop and technical colleagues, Thilo Lampe, Lutz Nagatz, Arno Ellermann, and Gudrun Zeising.

My work was supported by the DFG 1952/1(NanoMet) and the International Graduate School of Metrology (IGSM). Last but not the least, I would appreciate my parents and my friends for their continuous support.